

p-ISSN 1811-1165
e-ISSN 2413-2179

VOLUME 18, No. 1(35), 2021

EURASIAN
PHYSICAL
TECHNICAL

JOURNAL

E.A. BUKETOV KARAGANDA UNIVERSITY

KARAGANDA, THE REPUBLIC OF KAZAKHSTAN

EURASIAN PHYSICAL TECHNICAL JOURNAL

p - ISSN 1811-1165
e - ISSN 2413-2179

Volume 18, No. 1(35), 2021

1st issue – March, 2004

Journal Founder:

**E.A. BUKETOV KARAGANDA
UNIVERSITY**

**Е.А.БӨКЕТОВ АТЫНДАҒЫ
ҚАРАҒАНДЫ УНИВЕРСИТЕТІ**

**КАРАГАНДИНСКИЙ УНИВЕРСИТЕТ
ИМ. Е.А.БУКЕТОВА**

Contact information:

Editorial board of EPhTJ (Build. 2, room 216)
E.A. Buketov Karaganda University
Universitetskaya Str.28, Karaganda,
Kazakhstan, 100028
Subscription index: 75240

Tel: +7(7212)77-04-03
Fax: +7(7212)77-03-84
E-mail: ephjt@mail.ru

Signed to print on **30.03.2021**.
Format 60x84 1/8. Offset paper.
Volume **11.12 p.sh.** Circulation 300 copies.
Agreed price. Order No. 30.

Басуға **30.03.2021**ж. қол қойылды.
Пішімі 60×84 1/8. Офсеттік қағазы.
Көлемі **11.12** ес.-б.т. Таралымы 300 дана.
Бағасы келісім бойынша. Тапсырыс № 30.

Подписано к печати **30.03.2021**.
Формат 60 × 84 1/8. Офсетная бумага.
Объем **11.12** печ.л. Тираж 300 экз.
Цена договорная. Заказ № 30.

Printed in the Publishing House
of the E.A. Buketov KarU

Е.А. Бөкетов атындағы ҚарУ баспасының
баспаханасында басылып шықты

Отпечатано в Издательстве
КарУ имени Е.А. Букетова

Chief EDITOR

Sakipova S.E., E.A. Buketov Karaganda University,
Karaganda, Kazakhstan

EDITORIAL BOARD

Aringazin A.K., L.N. Gumilyov Eurasian National University,
Nur-Sultan, Kazakhstan

Dueck J., Erlangen-Nuernberg University, Erlangen, Germany

Dzhumanov S., Institute of Nuclear Physics, Uzbekistan
Academy of Sciences, Tashkent, Uzbekistan

Ibrayev N.Kh., Institute of Molecular Nanophotonics,
E.A.Buketov Karaganda University, Kazakhstan

Jakovics A., Institute of Numerical Modelling, University of
Latvia, Riga, Latvia

Kadyrzhanov K.K., L.N. Gumilyov Eurasian National
University, Nur-Sultan, Kazakhstan

Kucherenko M.G., Director of the Laser and Information
Biophysics Centre, Orenburg State University, Orenburg,
Russia

Kumekov S.E., K. Satbaev Kazakh State National Technical
University, Almaty, Kazakhstan

Kuritnyk I.P., Department of Electronics and Automation, High
school in Oswiecim, Poland

Miau J.J., Department of Aeronautics and Astronautics,
National Cheng Kung University, Tainan, Taiwan

Narimanova G.N., Tomsk State University of Control Systems
and Radioelectronics, Tomsk, Russia

Potapov A.A., V.A. Kotelnikov Institute of Radio Engineering
and Electronics of RAS, Moscow, Russia

Pribaturin N.A., Institute of Thermal Physics, SB RAS,
Novosibirsk, Russia

Saulebekov A.O. Kazakhstan Branch of Lomonosov Moscow
State University, Nur-Sultan, Kazakhstan

Senyut V.T., Joint Institute of Mechanical Engineering of
National Academy of Sciences of Belarus, Minsk, Belarus

Shrager E.R., National Research Tomsk State University,
Tomsk, Russia

Stoev M., South-West University «Neofit Rilski», Blagoevgrad,
Bulgaria

Trubitsyn A.A., Ryazan State Radio Engineering University,
Ryazan, Russia

Zhanabaev Z.Zh., Al-Farabi Kazakh National State University,
Almaty, Kazakhstan

TECHNICAL EDITORS

Kambarova Zh.T., **Akhmerova K.E.**, E.A. Buketov Karaganda
University, Karaganda, Kazakhstan

CONTENTS

MATERIALS SCIENCE

1. *Malyshev A.V., Lysenko E.N., Sheveleva E.A., Surzhikova O.A., Aringazin A.K.*
Relationship between magnetic properties and microstructure of ferrites during sintering in radiation and radiation-thermal conditions..... 3
2. *Yurov V.M., Goncharenko V.I., Oleshko V.S.*
Anisotropy of the surface of cubic body-centered crystal lattices..... 9
3. *Kruchinin N.Yu., Kucherenko M.G.*
Rearrangement of the conformational structure of polyampholytes on the surface of a metal nanowire in a transverse microwave electric field..... 16
4. *Kasenov B.K., Kasenova Sh.B., Sagintaeva Zh.I., Nukhuly A., Turtubaeva M.O., Bekturganov Zh.S., Zeynidenov A.K., Kuanyshbekov E.E., Issabaeva M.A.*
Synthesis and X-ray investigation of novel nanostructured copper-zinc manganites of lanthanum and alkali metals..... 29

ENGINEERING

5. *Leonov A., Usacheva T., Lyapunov D., Voronina N., Galtseva O., Rogachev A.*
Improving the heat resistance of polymer electrical insulation systems for the modernization of induction motors..... 34
6. *Trubitsyn A.A., Grachev E.Yu., Kozlov E.A., Shugayeva T.Zh.*
Development of High Power Microfocus X-ray Tube..... 43

ENERGY. THERMOPHYSICS. HYDRODYNAMICS

7. *Tanasheva N.K., Bakhtybekova A.R., Sakipova S.E., Minkov L.L. Shuiushbaeva N.N., Kasimov A.R.*
Numerical simulation of the flow around a wind wheel with rotating cylindrical blades... 51
8. *Bezrodny M.K., Oslovskiy S.A.*
Efficiency analysis of using a combination of air and ground heat pumps for heating and ventilation..... 57
9. *Dyussenov K. M., Sakipov K.E., Shayakhetova R.T., Nedugov I.A., Aitmagambetova M. B., Yessimseit A.K.*
Influence of the impact of acoustic cavitation on the physical and chemical properties of water..... 65
10. *Shaimerdenova K.M., Stoev M., Sekerbayeva G.K., Bulkairova G.A., Ospanova D.A., Tussybayeva A.S., Rakhmankyzy A.*
Investigation of the thermophysical characteristics of minerals at various heating parameters..... 70

PHYSICS AND ASTRONOMY

11. *Turdybekov K. M., Turdybekov M.K.*
The study of curves of the transient current in polytetrafluoroethylene by means Fourier analysis..... 75

SUMMARIES..... 80

INFORMATION ABOUT AUTHORS..... 85

GUIDELINES FOR AUTHORS..... 87

DOI 10.31489/2021No1/3-8

UDC 616.874

RELATIONSHIP BETWEEN MAGNETIC PROPERTIES AND MICROSTRUCTURE OF FERRITES DURING SINTERING IN RADIATION AND RADIATION-THERMAL CONDITIONS

Malyshev A.V.¹, Lysenko E.N.¹, Sheveleva E.A.¹, Surzhikova O.A.², Aringazin A.K.³

¹Tomsk Polytechnic University, Tomsk, Russia, malyshev@tpu.ru

²Ceské vysoké učené technické v Prague, Prague, Czech Republic

³L.N. Gumilev Eurasian National University, Nur-Sultan, Kazakhstan

The studies of correlation between magnetic properties and microstructure were conducted on samples of lithium-substituted ferrite, sintered in radiation and radiation-thermal conditions. Radiation-thermal sintering was performed for compacts irradiated with a pulsed electron beam with energy of (1.5–2.0) MeV, beam current per pulse of (0.5–0.9) A, irradiation pulse duration of 500 μs, pulse repetition rate of (5–50) Hz, and compact heating rate of 1000 °C/min. Sintering in thermal furnaces (T-sintering) was carried out in a preheated chamber electric furnace. The paper shows that magnetic induction does not depend on the ferrite grain size. In this case, the coercive force is inversely proportional to the grain size and depends on the intragranular porosity of ferrite samples. In contrast to thermal sintering, radiation-thermal sintering does not cause capturing of intergranular voids by growing grains and enhances coagulation of intragranular pores.

Keywords: ferrites, sintering, magnetic properties, microstructure, intense electron beams, high temperatures.

Introduction

The use of the effect of ionizing radiation fluxes in production and modification of materials has been observed to grow in recent years [1–5]. Particularly interesting and fundamentally new findings were obtained for a combined effect of powerful radiation fluxes and high temperatures (the so-called radiation-thermal effects). The most striking of these findings is the effect of multiple acceleration of synthesis [6–11] and sintering [12–22] of inorganic powder materials. The processes of ferrite material sintering under radiation-thermal effect have been most fully studied for lithium-titanium ferrites and similar structures [23–29]. It is obvious that the main functional characteristics of ferrimagnets are their magnetic properties. Attaining a given level of performance properties of ferrites is the ultimate goal of any production technology. Therefore, controlled formation of the main electromagnetic parameters is of high relevance.

However, the processes of magnetization reversal in ferrites are closely related to the features of their microstructure. Therefore, data on the relationship between electromagnetic characteristics and microstructure of ferrites at the stage of their sintering are of interest. This paper presents the results of the study of the kinetic patterns for formation of the hysteresis loop parameters, and patterns of changes in the microstructure of ferrites sintered under thermal and radiation-thermal effects.

1. Experimental part

The study uses powders of lithium-titanium ferrite synthesized from a mechanical mixture of oxides and carbonates containing (wt, %): Li₂CO₃ – 11.2; TiO₂ – 18.65; ZnO 7.6; MnCO₃ 2.74; others are Fe₂O₃. To prepare the compact, 10% solution of polyvinyl alcohol is added to the synthesized mixture in an amount of 12 wt.% charge. Compacts in the form of pellets and annular cores with a thickness of 2 mm are made by cold single-action pressing. Optimum compacting pressure is selected experimentally. It was found that at compacting pressures below 40 MPa, press samples exhibit low density, and at compacting pressures of more than 250 MPa, samples show cracks and delamination (repressing process).

Thus, the most optimal compacting pressure is in the range of (110–200) MPa. This compacting pressure provides an acceptable density for both green and sintered samples. In the study, the pressing mode used was as follows: P = 130 MPa, 1 min dwelling time; and radiation-thermal (RT) and thermal (T) modes of sintering compacts. In RT-sintering, compacts were exposed to pulsed electron beam with energy of (1.5–2.0) MeV using an ILU-6 accelerator. The pulsed beam current was (0.5–0.9) A, the irradiation pulse

duration was 500 μs , the pulse repetition rate was (5–50) Hz, and the compact heating rate was 1000 $^{\circ}\text{C}/\text{min}$. The samples were irradiated in lightweight chamotte box with a wall bottom thickness of 15 mm. The exposed side of the box was covered with a radiation-transparent protector with a mass thickness of 0.1 $\text{g}\cdot\text{cm}^{-1}$. The temperature was measured using a control sample placed in close proximity to the sintered compacts.

T-sintering was performed in a preheated chamber electric furnace, which provided a heating rate comparable to that of radiation heating. The cell design and temperature control technique were similar to those used for RT-sintering. Both sintering modes were performed in air. The magnetic characteristics of the ferrites were measured using the standard technique with an F 5063 ferrometer. The magnetic field was 5 Oe at a frequency of 50 Hz. The degree of porosity and grain sizes were investigated using ground, polished, and etched sections of the sintered samples with an MBI-15U optical microscope. The kinetic dependences of the hysteresis loop parameters B_m , B_r/B_m , and H_c of ferrite samples were studied after annealing in the temperature range of (1173–1373) K [30].

2. Results and discussion

Figure 1 shows the dependences of the average grain size d , B_m and H_c on the relative linear shrinkage $\Delta L/L$ on sintering time, since only this mode (in contrast to fast RT-compaction) provides detailed dynamics of the formation of these parameters.

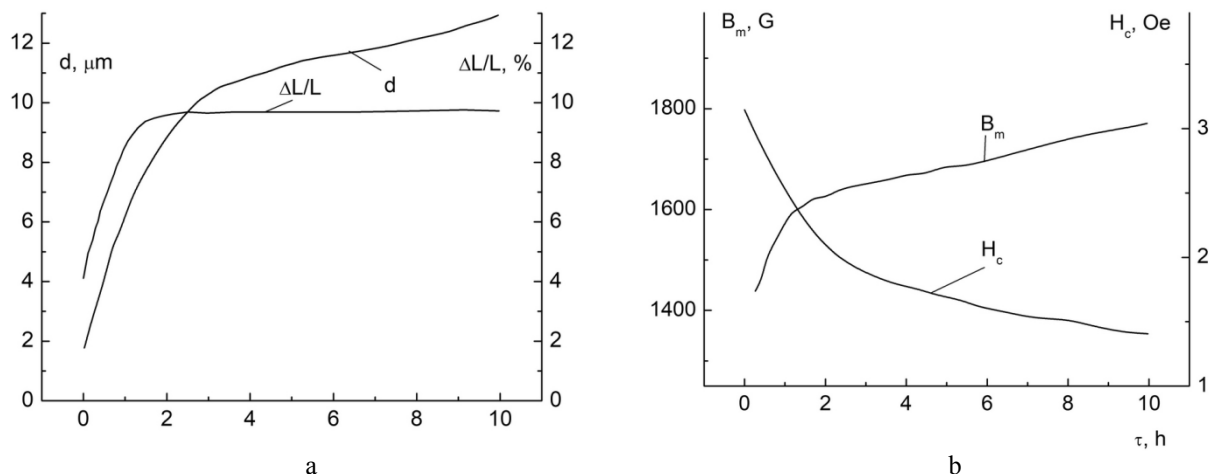


Fig.1. Dependencies of average grain size d and $\Delta L/L$ (a), B_m and H_c (b) of ferrites on time during thermal sintering ($T_{\text{sint}} = 1273$ K).

This figure shows three stages of sintering. *Stage 1* (up to 60 min) is accompanied by intense shrinkage of the sample, relatively slow growth of grains, increase in B_m and decrease in H_c . At this stage, interparticle sliding followed by a sharp decrease in intergranular voids (shrinkage), increased concentration of the magnetic phase, and reduced demagnetization effect of the void (increased B_m). *Stage 2* (up to 120 min) shows few intergranular voids, shrinkage slows down, B_m reaches saturation, and grains continue growing due to formation of numerous grain boundaries. At *stage 3* (>120 min), shrinkage is completed, B_m is almost constant, grains continue growing (due to collective recrystallization), and H_c continues to decrease. This behavior is characteristic of RT-sintering of ferrite compacts. However, the first two phases occur during compact heating and only the last phase can be observed in the isothermal regime.

Thus, the data presented on Figure 1 show the correlation of H_c with ferrite porosity and the grain size. No correlation was found between magnetic induction and the grain size. It was previously found that the dependence of B_m and B_r/B_m on porosity is ‘apparent’, since the maximum induction but not saturation induction was measured at magnetizing field of 5 Oe. The true saturation induction mainly depends on the phase composition and the depth of phase transformations, but it is not related to porosity. Therefore, the microstructure features enable forecasting H_c and, conversely, the value of H_c indicates the grain size and porosity of the samples. To quantitatively assess this correlation, use the Globus theory [28–30] to calculate the relationship between H_c and grain size and compare it with experimental results.

According to the model proposed by Globus, a ferrite grain contains one boundary. In fields less than H_c , the edges of the domain boundary remain fixed along the circumference at the grain boundary, and it is observed to bend. The external magnetic field required for irreversible displacement of the 180-degree domain wall is expressed by [31]:

$$H_c = \frac{4f}{J_s \cdot d}, \quad (1)$$

where f is the force per unit area exerted on the domain interface; d is grain size; J_s is saturation magnetization. It is experimentally shown that for various ferrites:

$$f = 0.15 \cdot \sigma_w, \quad (2)$$

where σ_w is the energy of the domain wall per unit area.

The energy of 180-degree domain wall can be expressed by [31]:

$$\sigma_w = \sqrt{\frac{2A}{K}}, \quad (3)$$

where A is the effective constant of exchange interaction; K is the crystal anisotropy constant.

The value of the Curie temperature indicates the value of exchange interactions [32]:

$$A = \frac{k\Theta}{a}, \quad (4)$$

where k is the Boltzmann constant; a is ferrite lattice parameter; Θ is Curie temperature.

The values of the saturation magnetization and Curie temperature for investigated Li-Ti ferrite are as follows: $J_s = 142$ G; $\Theta = 260$ °C. Lattice parameter $a = 8.36$ Å. The value of the anisotropy constant can be taken $K = -5 \cdot 10^4$ erg/cm³.

Appropriate substitutions into equations (1)–(4) yield the theoretical dependence of the H_c value on the grain size:

$$H_c = \frac{15.2}{d}, \quad (5)$$

where H_c is the coercive force; d is grain size.

It should be emphasized that when inclusions (impurity phases, pores, etc.) occur in the ferrite grain the domain wall in the equilibrium position intersects a certain number of inclusions, since its area and, hence, its energy reduce. In this case, additional energy is spent on magnetization reversal, and H_c is expected to increase. This process will involve the inclusions with the size equal to or exceeding the thickness of the domain wall h [31–32]:

$$h = 87a \sqrt{\frac{\Theta J_s}{|K|}}, \quad (6)$$

where h is the domain wall thickness.

Substituting the corresponding data into (5), we obtain $h \approx 1$ μm. Consequently, all inclusions of the size of $r \approx 0.1$ μm will affect the value of H_c .

If H_c is limited by inclusions in the grain material, the value of H_c will be expressed by:

$$H_c = \frac{3\pi^{1/3}\sigma_w}{4J_s r} (6V)^{3/2}, \quad (7)$$

where $V = \frac{3\pi r^3}{4d_v^3}$ is the volume fraction of inclusions; r is radius of inclusions; d_v is distance between inclusions.

Substituting the corresponding values of σ_w and J_s into (7), we obtain:

$$H_c = \frac{27.8}{r} (6V)^{3/2}, \quad (8)$$

The theoretical dependence of H_c on the size of inclusions for their various volume fractions is shown in Figure 2. Figure 3 presents the dependencies of H_c on the relative volume of inclusions with their sizes being constant.

Figures 2 and 3 show that at high recrystallization rate the capture of intergranular voids into the grain volume increases H_c . The smaller the radius of these voids, the higher the H_c value. The dissociation of captured voids (pores) into smaller ones causes similar effect.

Figure 4 shows the experimental (symbols) and theoretical (solid lines) dependencies of H_c on the average ferrite grain size. The experimental and theoretical dependencies for RT-sintering are seen to be in good agreement. This indicates that intergranular voids are not captured into growing grains or that these voids enter the grains in the form of large formations.

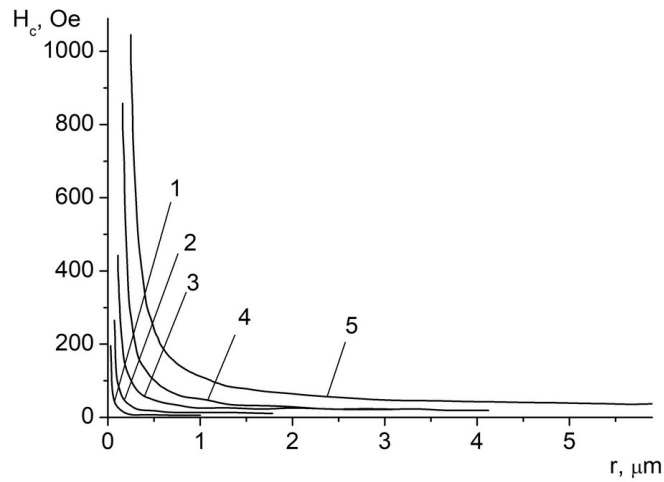


Fig.2. Calculated dependences of H_c on the radius of inclusions r at their relative volume n :
 1 – $n = 0.05$; 2 – $n = 0.1$; 3 – $n = 0.2$; 4 – $n = 0.3$; 5 – $n = 0.5$

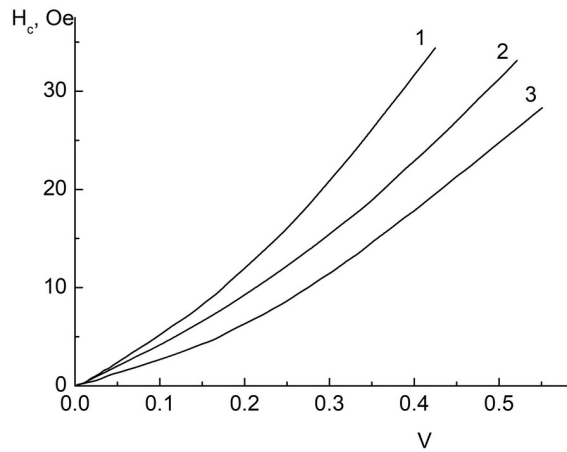


Fig.3. Calculated dependences of H_c on the relative volume of inclusions.
 The radius of inclusions r is $3 \mu\text{m}$ (1); $4 \mu\text{m}$ (2); $5 \mu\text{m}$ (3).

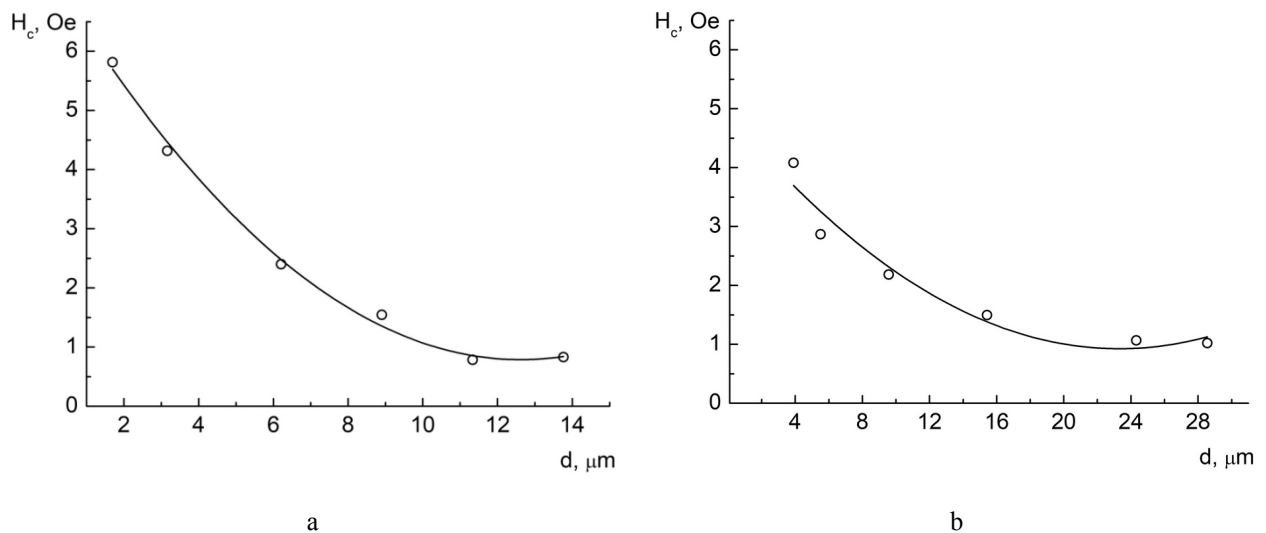


Fig.4. Dependence of H_c on the average ferrite grain size d . Sintering of ferrite samples at 1373 K in RT mode (a); T-mode (b). Symbols are experimental data; solid lines are calculated dependencies.

During T-sintering, a coincidence of the calculated and experimental data can be observed only at early sintering stages. As grains grow larger, this coincidence is violated due to intense capturing of small inclusions into the grain volume. The analysis of micrographs of thin sections of ferrite ceramics shows that the capture of intergranular pores during T-sintering is due to growing grains.

Conclusion

At short sintering time, the grains are predominantly small with a small number of inclusions. The voids are concentrated mainly in the intergranular space. Only individual recrystallized grains contain pores in their volume. Increased sintering time enlarges grains and reduces the volume of intergranular pores. The grains are enriched with inclusions and exhibit insignificant number of pores at the grain boundary. These effects are much weaker in ferrites produced by RT-sintering.

Thus, the data obtained indicate that magnetic induction does not depend on the ferrite grain size. Coercive force is inversely proportional to the grain size and is determined by intragranular porosity. In contrast to T sintering, RT-sintering does not cause capturing of intergranular voids by growing grains and promotes coagulation of intragranular pores.

It is shown for the first time that using of radiation-thermal sintering in practice makes it possible to obtain lithium-substituted ferrites with a more perfect crystal structure, including without intragranular pores and without entrapment of intergranular voids by growing grains.

Acknowledgments

The research is funded by the Ministry of Education and Science of the Russian Federation as part of the “Science” Program (project No. FSWW-2020-0014).

REFERENCES

- 1 Groom D.E., Klein S.R. Review of Particle Physics. *European Physical Journal C*. 1998, Vol.3, pp. 144 – 151.
- 2 Sagynganova I.K., Markin V.B. The organizations of the tasks implementation in the distributed automatic control systems of heat supply stations. *News of the National Academy of Sciences of the Republic of Kazakhstan*. 2019, Vol. 1, No. 433, pp. 63 – 67.
- 3 Ershov B.G. Radiation technologies: their possibilities, state, and prospects of application. *Herald of the Russian Academy of Sciences*. 2013, Vol. 83, No. 5, pp. 437 – 447.
- 4 Obodovskiy I. Radiation: fundamentals, applications, risks, and safety. Elsevier Inc. 2019, 694 p.
- 5 Yurov V.M., Baltabekov A.S., Laurinas V.C., Guchenko S.A. Dimensional effects and surface energy of ferroelectric crystals. *Eurasian Physical Technical Journal*. 2019, Vol. 16, No. 1(31), pp. 18 – 23.
- 6 Sharma P. Uniyal, Investigating thermal and kinetic parameters of lithium titanate formation by solid-state method, *J. Therm. Anal. Calorim.* 2017, Vol. 128, pp. 875 – 882.
- 7 Rakshit S.K., Parida S.C., Naik Y.P., Venugopal V. Thermodynamic studies on lithium ferrites, *J. Solid State Chem.* 2011, Vol. 184, pp. 1186 – 1194.
- 8 Lysenko E.N., Surzhikov A.P., Vlasov V.A., et al. Synthesis of substituted lithium ferrites under the pulsed and continuous electron beam heating. *Nuclear Instruments and Methods in Physics Research, Section B: Beam Interactions with Materials and Atoms*. 2017, Vol. 392, pp. 1 – 7.
- 9 Surzhikov A.P., Lysenko E.N., Malyshev A.V., et al. Influence of mechanical activation of initial reagents on synthesis of lithium ferrite. *Russian Physics Journal*. 2012, Vol. 55, No. 6, pp. 672 – 677.
- 10 Surzhikov A.P., Pritulov A.M., Lysenko E.N., Sokolovskii A.N., Vlasov V.A., Vasendina E.A. Dependence of lithium-zinc ferrosin phase composition on the duration of synthesis in an accelerated electron beam. *Journal of Thermal Analysis and Calorimetry*. 2012, Vol. 110, No. 2, pp. 733-738.
- 11 Boldyrev V.V., Voronin A.P., Gribkov O.S., Tkachenko E.V., Karagedov G.R., Yakobson B.I., Auslender V.L. Radiation-thermal synthesis. Current achievement and outlook, *J. Solid State Ion*. 1989, Vol. 36, pp. 1 – 6.
- 12 Lyakhov N.Z., Boldyrev V.V., Voronin A.P., et al. Electron beam stimulated chemical reaction in solids. *Journal of Thermal Analysis*. 1995, Vol. 43, pp. 21 – 31. <https://doi.org/10.1007/BF02635965>.
- 13 Kostishin V.G., Andreev V.G., Korovushkin V.V., et al. Preparation of 2000NN ferrite ceramics by a complete and a short radiation-enhanced thermal sintering process. *Inorganic Materials*. 2014, Vol. 50, pp. 317 – 323.
- 14 Kostishyn V.G., Komlev A.S., Korobeynikov M.V., et al. Effect of a temperature mode of radiation-thermal sintering the structure and magnetic properties of Mn-Zn-ferrites. *Journal of Nano-and Electronic Physics*. 2015, Vol.7, pp. 04044.
- 15 Lisitsyn V., Lisitsyna L., Dauletbekova A., et al. Luminescence of the tungsten-activated MgF₂ ceramics synthesized under the electron beam. *Nuclear Instruments and Methods in Physics Research Section B: Beam Interactions with Materials and Atoms*. 2018, Vol. 435, pp. 263 – 267. <https://doi.org/10.1016/j.nimb.2017.11.012>

- 16 Cleland M.R., Parks L.A. Medium and high-energy electron beam radiation processing equipment for commercial applications. *Nuclear Instruments and Methods in Physics Research Section B: Beam Interactions with Materials and Atoms*. 2003, Vol. 208, pp. 74 – 89. [https://doi.org/10.1016/S0168-583X\(03\)00672-4](https://doi.org/10.1016/S0168-583X(03)00672-4).
- 17 Mehnert R. Review of industrial applications of electron accelerators. *Nuclear Instruments and Methods in Physics Research Section B: Beam Interactions with Materials and Atoms*. 1996, Vol. 113, pp. 81 – 87.
- 18 Martins M.N., Silva T.F. Electron accelerators: History, applications, and perspectives. *Radiation Physics and Chemistry*. 2014, Vol. 95, pp. 78 – 85. <https://doi.org/10.1016/j.radphyschem.2012.12.008>.
- 19 El-Shobaky G.A., Ibrahim A.A. Solid-solid interactions between ferric oxide and lithium carbonate and the thermal stability of the lithium ferrites produced. *Thermochim. Acta*. 1987, Vol. 118, pp. 151–158.
- 20 Salimov R.A., Cherepkov V.G., Golubenko J.I., et al. D.C. high power electron accelerators of ELV-series: status, development, applications. *J. Radiation Phys. Chem*. 2000, Vol. 57, pp. 661 – 665.
- 21 Cleland M.R., Parks L.A. Medium and high-energy electron beam radiation processing equipment for commercial applications, *Nucl. Instr. Meth. B*. 2003, Vol. 208, pp. 74 – 89.
- 22 Mehnert R. Review of industrial applications of electron accelerators, *Nucl. Instr. Meth. B*. 1996, Vol. 113, pp. 81 – 87.
- 23 Neronov V.A., Voronin A.P., Tatarintseva M.I., Melekhova T.E., Auslender V.L. Sintering under a high-power electron beam, *J. Less-Common Metals*. 1986, Vol. 117, pp. 391 – 394.
- 24 Surzhikov A.P., Frangulyan T.S., Ghyngazov S.A. A thermoanalysis of phase transformations and linear shrinkage kinetics of ceramics made from ultrafine plasmochemical $ZrO_2(Y)-Al_2O_3$ powders. *Journal of Thermal Analysis and Calorimetry*. 2014, Vol. 115, No. 2, pp. 1439 – 1445.
- 25 Surzhikov A.P., Frangulyan T.S., Ghyngazov S.A., et al. Physics of magnetic phenomena: Investigation of electroconductivity of lithium pentaferriite. *Rus. Phys. J.* 2006, Vol. 49, No. 5, pp. 506 – 510.
- 26 Surzhikov A.P., Lysenko E.N., Malyshev A.V., et al. Study of the radio-wave absorbing properties of a lithium-zinc ferrite based composite. *Rus. Phys. J.* 2014, Vol. 57, No. 5, pp. 621 – 626.
- 27 Surzhikov A.P., Peshev V.V., Pritulov A.M., Gyngazov S.A. Grain-boundary diffusion of oxygen in polycrystalline ferrites. *Rus. Phys. J.* 1999, Vol. 42, No. 5, pp. 490 – 495.
- 28 Globus A. Some physical consideration about the domain wall size. Theory of magnetization mechanisms. *J. Phys. (France)*. 1977, Vol. 38, No. 4. pp. 1 – 15.
- 29 Globus A. Influence des dimensions des parois la permeability. *C. R. Acad. Sci.* 1962, Vol. 255, pp. 1709 – 1711.
- 30 Globus A., Guyot M. Wall displacement and bulging in magnetization mechanisms of the hysteresis loop. *Phys. Status Solidi B*. 1972, Vol. 52, pp. 427 – 431.
- 31 Rankis G., Yurshevich V., Jankovskis J. Modified model of initial magnetic permeability of polycrystalline ferrites. *Journal De Physique. IV: JP*. 1997, Vol. 7, No. 1, pp. 207 – 208.
- 32 Saulebekov A.O., Venos D., Kambarova Zh.T., et al. Development of energy analyzer of charged particles based on the basis non-uniform electrostatic field. *Eurasian Physical Technical Journal*. 2019, Vol.16, No.1(31) pp. 24 – 29.

ANISOTROPY OF THE SURFACE OF CUBIC BODY-CENTERED CRYSTAL LATTICES

Yurov V.M.¹, Goncharenko V.I.², Oleshko V.S.²

¹E.A. Buketov Karaganda University, Karaganda, Kazakhstan, exciton@list.ru

²Moscow Aviation Institute (National Research University), Moscow, Russia, ovs_mai@mail.ru

In the work of Shebzukhova and Arefieva, by the method of electronic-statistical calculation of the anisotropy of the surface energy of metals, a method for estimating the work function of electrons from a metal was determined. The surface energy and electron work function of four main faces of cadmium and zinc crystals and five faces of mercury are estimated. In the work of Bokarev, the anisotropy of the surface energy of single crystals was calculated from the model of coordination melting of crystals. Based on experimental studies and theoretical calculations, it is shown that the model of coordination melting of crystals unambiguously links the physicochemical properties of the surface of single crystals with their crystal structure. In our proposed empirical model, not only the anisotropy is calculated, but also the thickness of the surface layer of the metal. It is shown that the thickness of the surface layer is determined by one fundamental parameter - the molar (atomic) volume, which periodically changes in accordance with the table of D.I. Mendeleev. It is shown in the work that the work function of electrons changes proportionally with a change in the surface energy of the metal. This means that the device we have developed can be used to measure the state of the metal surface and its anisotropy.

Keywords: anisotropy, metal, surface energy, crystal, nanostructure.

Introduction

This work is a continuation of works [1, 2], where it is shown that for the operational measurement of the energy state of the metal surface, it is necessary to use non-destructive testing methods. The method of measuring the contact potential difference (or the work function of an electron from the surface) was chosen as such a control. Here the measuring electrode of the device, at which the contact potential difference and the investigated metal surface are measured, form a kind of capacitor, between which this contact potential difference is formed. The positive aspect of the capacitor method for measuring the contact potential difference is:

- high precision in capacitor manufacturing;
- the capacitor in its normal state has low heat losses and a high efficiency;
- electrical fields have little effect on the mechanical parts of the capacitor;
- the sensor of the device can be made by giving it the shape of the investigated surface.

The portable complex for measuring the work function of electrons developed by the authors on the basis of a portable digital oscilloscope makes it possible to perform non-destructive testing of the surface of metal parts in a continuous mode during their production, operation or repair.

We used this complex to determine the surface energy of the surface of pure metals and alloys that are used in aviation. This work is of a theoretical nature and is devoted to the surface of body-centered cubic crystal lattices.

1. Analysis of publications

First of all, we will note only those publications that concern the anisotropy of the metal surface, to which we will devote our presentation. A significant number of works have been devoted to the anisotropy of surface energy and the work function of electrons from metals, since it must be taken into account in solving practical problems faced by both technicians and technologists.

For example, in the microelectronic industry materials with design standards of 16-14 nm are already being used, and technologies with design standards at the level of 10^{-7} nm are being mastered. However, such a transition to the nanoscale requires a transition to work with new materials. In this case, the quantities of

the above-mentioned regions determine their size dependence and the surface energy of the crystal and its anisotropy have a significant dependence on the properties of materials.

In works [3, 4], by the method of electron-statistical calculation of the surface energy of metals, a method was determined for the work function of electrons from a metal with structures having hexagonal and rhombic syngony. The relationship between the surface energy and the work function of the electron is obtained. These calculations were performed for crystals of zinc, cadmium, and mercury. The formula for the work function of an electron $\varphi(\text{hkl})$ and surface energy $f_{\omega}(\text{hkl})$ of close-packed faces of metallic macrocrystals with noncubic structures is as follows [3]:

$$\varphi(\text{hkl}) = -\left(\frac{\partial E_0}{\partial z}\right)_{\bar{R}} - \frac{1}{n_v \tau} \left(\frac{\partial f_{\omega}(\text{hkl})}{\partial z}\right)_{\bar{R}}. \quad (1)$$

Here, the first term is a certain constant, independent of the indices of the crystallographic faces, the second determines the orientational dependence of the work function of electrons, which can be determined using Thomas – Fermi expressions for the variation of the electron density at the metal – vacuum interface with corrections [4]:

$$f_{\omega}(\text{hkl}) \cong \frac{1}{5} n(\text{hkl}) |W(r_0)| Q. \quad (2)$$

In formulas (1) and (2), a is the crystal lattice parameter, z is the number of free electrons per atom, Q is a function that weakly depends on z , $|W(r_0)|$ is the bond energy of the crystal lattice, $n(\text{hkl})$ is the concentration of particles on the face. The summation in (2) for each face was carried out up to the j -th plane, at which the contribution to the surface energy was $\leq 0.1 \text{ mJ/m}^2$.

With the effective thickness of the monatomic surface layer $\tau = R$ (where R is the radius of the s -sphere) and bearing in mind (2), we obtain [3, 4]:

$$\varphi(\text{hkl}) + \frac{B}{z} a^2 \cdot f_{\omega}(\text{hkl}) = \text{const}. \quad (3)$$

The constant B depends on the type of lattice structure of the metal and in the first approximation for hcp crystals is 3.51, and for crystalline mercury with a rhombohedral lattice 5.846. Expression (3) conveys well the anisotropy $\varphi(\text{hkl})$ of metals. To estimate the anisotropy of the work function of electrons, formula (3) is reduced to the form [3, 4]:

$$\varphi(\text{hkl}) = \varphi_0 \left(1 - \frac{f_{\omega}^{\circ}(\text{hkl})}{f_0}\right). \quad (4)$$

Here $\varphi_0 = \text{const} = \varphi + B/z a^2 f_{\omega}$, $f_0 = \varphi_0 z / B a^2$, φ is the Richardson work function of electrons from the polycrystalline sample, f_{ω} is the surface tension of the liquid metal at the melting temperature T_m , $f_{\omega}^{\circ}(\text{hkl})$ is the surface energy of the faces at a given temperature. Using expressions (2) and (4), the surface energy and work function of electronically four main faces of cadmium and zinc crystals and five faces of mercury were estimated. Thus, for zinc, the deviation of the calculated value of $\varphi(0001)$ at 293 K from $\varphi_{\text{exp}}(0001)$ and from the value for a polycrystal is 7.94 and 7.59 %, respectively. And for cadmium, the calculation error in comparison with the work function of electrons of the polycrystal is only 5.3%. In view of the absence in most cases and the ambiguity of the available experimental data on the surface energies of the faces of single crystals with noncubic structures, thin films and nanoparticles of the considered metals, expressions (3) and (4) can be used to estimate the surface energies of metal surfaces at the interface with vacuum from the work function data electrons of these surfaces.

In [5, 6], the relationship between the anisotropy of the surface energy of single crystals and the crystal structure is considered. Based on experimental studies and theoretical calculations, it is shown that the model of coordination melting of crystals (MCP) unambiguously links the physicochemical properties of the surface of single crystals with their crystal structure. The calculations of the surface energy will be carried out according to the formula derived under the assumption that there are no first-order phase transitions in these substances up to their melting point [5, 6]:

$$\sigma_{\text{hkl}} = \left(\frac{\rho l_{\text{hkl}}}{M}\right) \int_0^{T_m} c_p dT. \quad (5)$$

where ρ is the density of the crystalline substance, and M is its molecular weight, T_m is the melting point, c_p is the molar heat capacity, $[hkl]$ is the thickness of the first coordination sphere in the $[hkl]$ direction, which for crystals with body-centered (bcc) and face-centered (fcc) cubic structure is given by the relations [6]:

$$\begin{aligned} \text{Im}3m, Z = 2; l_{100} = a; l_{110} = a\sqrt{2}; l_{111} = a/\sqrt{3}, \\ \text{Fm}3m, Z = 4; l_{100} = a; l_{110} = a/\sqrt{2}; l_{111} = 2a/\sqrt{3}. \end{aligned} \quad (6)$$

We take the values of ρ , M , T_m and c_p for metals from the reference book [7]. Table 1 shows the calculations of the surface energy anisotropy by the MCP in comparison with the calculations of the surface energy anisotropy and the electron work function by several theoretical models [2–4].

Table 1. Anisotropy of the surface energy of metals, calculated from the MCP in comparison with the anisotropy of the surface energy and the work function of the electron, known from the literature

Me	(hkl)	Structure	σ_{hkl} by MCP, mJ/m ² [6]	σ_{hkl} [10], mJ/m ²	σ_{hkl} [8], mJ/m ²	F_{hkl} , eV [10]	F_{hkl} , eV [8]	F_{hkl} , eV [9]
Li	100	Im3m	304	436	541	3.15	2.968	2.28
	110		430	458	585	3.33	3.221	2.82
	111		180	-	601	-	2.746	2.11
Na	100	Im3m	189	236	258	2.76	2.638	2.28
	110		267	307	247	2.94	2.839	2.82
	111		109	-	302	-	2.585	2.11
K	100	Im3m	124	129	148	2.34	2.224	2.25
	110		175.3	116	137	2.38	2.372	2.79
	111		71.6	112	165	2.41	2.18	2.08
Rb	100	Im3m	101	107	126	2.22	2.116	2.16
	110		143	92	110	2.32	2.243	2.68
	111		58.4	89	135	2.29	2.096	2.00
Cs	100	Im3m	85	92	114	2.03	1.974	1.87
	110		120	72	97	2.09	2.073	2.34
	111		49	70	119	2.10	1.971	1.72

As can be seen from Table 2, the calculated values of the work function of different crystal faces are proportional to the surface energies of these faces, calculated using the model of coordination crystal melting. The main goal of this work is to build a model of the surface layer of perfect single crystals and to clarify the role of surface energy in physical processes occurring in the nanoscale range.

Table 2. Anisotropy of the surface energy of metals calculated by (13) in comparison with the anisotropy of the surface energy and the work function of the electron

Me	(hkl)	Structure	T_m , K	$R(I)$, nm	σ_{hkl} by (13), mJ/m ²	σ_{hkl} by MCP, mJ/m ² [6]	σ_{hkl} [10], mJ/m ²	F_{hkl} , eV [8]
Li	100	Im3m	454	3.14 (9)	454 (9)	304	436	2.968
	110				636 (13)	430	458	3.221
	111				259 (5)	180	-	2.746
Na	100	Im3m	371	5.7 (13)	371 (13)	189	236	2.638
	110				519 (18)	267	307	2.839
	111				212 (7)	109	-	2.585
K	100	Im3m	337	10.9 (20)	337 (20)	124	129	2.224
	110				472 (28)	175.3	116	2.372
	111				193 (11)	71.6	112	2.18
Rb	100	Im3m	312	13.4 (24)	312 (24)	101	107	2.116
	110				437 (34)	143	92	2.243
	111				178 (14)	58.4	89	2.096
Cs	100	Im3m	302	16.8 (27)	302 (27)	85	92	1.974
	110				423 (38)	120	72	2.073
	111				173 (15)	49	70	1.971

2. Description of the empirical model

In [11], when considering the melting temperature of small particles, we obtained the equation:

$$T(r) = T_0 \left(1 - \frac{R(I)}{r} \right), \tag{7}$$

where the parameter $R(I)$ is determined by the expression:

$$R(I) = \frac{2\sigma v}{RT}, \tag{8}$$

where σ - surface tension, v - molar volume, R - universal gas constant, T - temperature.

Experimental studies carried out by us with physical objects on thin films of various nature: mechanical, optical, magnetic, as well as the results of other researchers, have shown the size dependence of all physical properties of small particles and thin films. This dependency looks like this:

$$\dot{A}(r) = \dot{A}_0 \left(1 - \frac{R(I)}{r} \right), \tag{9}$$

where $A(r)$ is a physical property (mechanical, etc.) that depends on the linear size (dimensional effect), A_0 is a physical property (volumetric) that does not depend on size.

It is clear that the surface of a solid is a nanostructure. The same is true for liquid. Equations (7), (8), and (9) have the same structure and diverge as $r \rightarrow 0$; therefore, we will redefine equation (9) and write down finally:

$$\begin{aligned} \dot{A}(r) &= \dot{A}_0 \left(1 - \frac{R(I)}{r} \right), \quad r \gg R(I), \\ A(r) &= A_0 \left(1 - \frac{R(I)}{R(I) + r} \right), \quad R_0 \leq r \leq R(I). \end{aligned} \tag{10}$$

This model is shown schematically in Figure 1. It is an ideal atomically smooth single crystal without vacancies, dislocations, and other defects.

The de Broglie layer $R_0 = \lambda_{dB} = \hbar/p$ for metals ranges from 0.01 nm to 0.1 nm. Quantum dimensional effects begin in this layer. The main quantum-dimensional structures include structures with a two-dimensional electron gas - epitaxial films, MIS structures, heterostructures, etc.; structures with one-dimensional gas - quantum threads or wires; structures with a zero-dimensional gas - quantum dots, boxes, crystallites [12].

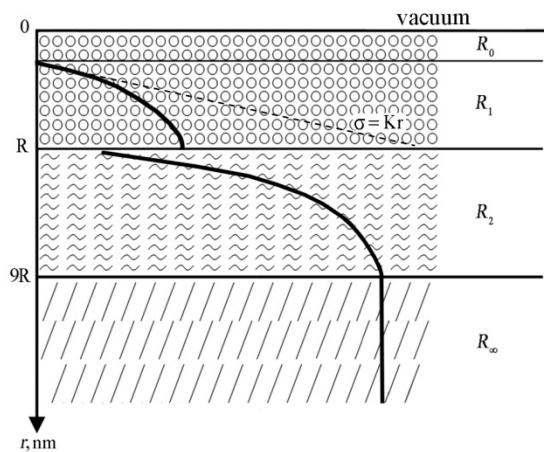


Fig.1. Schematic representation of the surface layer. Designations: R_0 - de Broglie layer; R_1 - layer $R(I)$; R_2 is the $R(II)$ layer; R_∞ - solid sample layer.

The $R(I)$ layer is described by the first dependence from equation (9) ($r \gg R(I)$). In the $R(I)$ layer with pure metal atoms, there is a reconstruction and relaxation associated with the rearrangement of the surface [13]. For gold, the lattice constant is equal to $R(I) = 0.41$ nm and the surface is rearranged at a distance

$R(I)_{Au} = 1.2/0.41 \approx 3$ of three atomic monolayers. Size effects in the R(I) layer are determined by the entire group of atoms in the system (collective processes). Such “semiclassical” size effects are observed only in nanoparticles and nanostructures [14]. Experimentally, they can be observed on very pure single crystals with grazing incidence of X-ray radiation, when the angle of incidence is equal to or less than the critical angle of total internal reflection [15]. When the angle of incidence becomes less than the critical one, the refracted wave exponentially decays in the volume at a characteristic depth of the order of several nanometers (for example, this depth is 3.2 nm for silicon, and 1.2 nm for gold). As a result, a so-called vanishing wave is formed, which propagates parallel to the surface. Therefore, the diffraction of such waves provides information on the structure of the surface layer [13].

The R(II) layer extends approximately to the size $R(II) \approx 9R = R_{\infty}$, where the bulk phase begins. Dimensional properties begin from this size. By nanomaterials it is customary to understand materials, the main structural elements of which do not exceed the nanotechnological boundary ~ 100 nm, at least in one direction [14-18]. A number of researchers are of the opinion that the upper limit (maximum size of elements) for nanostructures should be related to some critical characteristic parameter: the mean free path of carriers in transport phenomena, the size of domains/domain walls, the Frank-Read loop diameter for dislocation slip and the like. This means that the R (II) layer should contain many dimensional effects associated with optics, magnetism, and other physical properties according to Eq. (10).

The R(II) layer is described by the second dependence from equation (10) ($R_0 < r < R(I)$). The parameter R(I) is related to the surface tension σ by formula (7). In [11], it is shown that, with an accuracy of 3%, the relation:

$$\sigma = 10^{-3} \cdot T_m, \quad (11)$$

where T_m is the melting point of the solid (K). The ratio is fulfilled for all metals and for other crystalline compounds. At $T = T_m$, from equation (8) we obtain:

$$R(I)_i = 0.24 \cdot 10^{-9} \nu. \quad (12)$$

Equation (12) shows that the thickness of the surface layer R(I) is determined by one fundamental parameter - the molar (atomic) volume of the element $\nu = M/\rho$, M is the molar mass (g / mol), ρ is the density (g/cm^3), which changes periodically in accordance with the table of D.I. Mendeleev. Equation (11) can be empirically rewritten as:

$$\sigma(hkl) = 10^{-3} \cdot T_m \cdot l(hkl), \quad (13)$$

where $l(hkl)$ for crystals with body-centered (bcc) and face-centered (fcc) cubic structures is given by relations (6) at $a = 1$.

Let's make calculations according to (12) and (13), taking reference data on T_m , M , ρ .

3. Research results and discussion

Table 2 shows that our empirical model, based on the results of calculations, does not differ much from the method of electron-statistical calculation of the surface energy of metals [3, 4] and from the model of coordination melting of crystals [5, 6]. However, in contrast to these models, our model gives a numerical value for the thickness of the surface layer and, perhaps, this is the first time. The thickness of the surface layer for the $\text{Li} \rightarrow \text{Cs}$ system ranges from 3 nm to 17 nm. If we recalculate it in lattice constants a , then it turns out that the surface layer contains on average 9 monolayers (Li) to 27 monolayers (Cs). Experimentally, such surface layers can be determined by methods of scattering X-rays during their internal reflection. Using this method, the thickness of the surface layer was determined for gold single crystals ($R(I) = 1.2$ nm) and for silicon ($R(I) = 3.1$ nm) [13], that is, this R(I) layer is a nanostructure (fig. 1). Let us now consider the system of atoms $\text{Li} \rightarrow \text{Cs}$. Consider a body-centered cubic lattice (BCC) (Fig. 2).

Figure 2 shows that the shift in the crystal occurs most easily along the atomic planes with the densest packing of atoms (Fig. 2, a). Plane ABCD (Fig. 2, b), the number of atoms in the plane ABCD - 1; area ABCD = a^2 ; area per 1 atom — specific area: $S = a^2/1 = a^2$ — measure of packing density. Plane ABGH (Fig. 2, c), the number of atoms in the plane ABGH - 2; area ABGH = $a^2\sqrt{2}$; $S = a^2\sqrt{2}/2 \approx 0.7a^2 < a$.

Since the physical and chemical properties along different directions depend on the density of atoms on them, the listed properties along different directions in crystalline bodies should be unequal (Fig. 3).

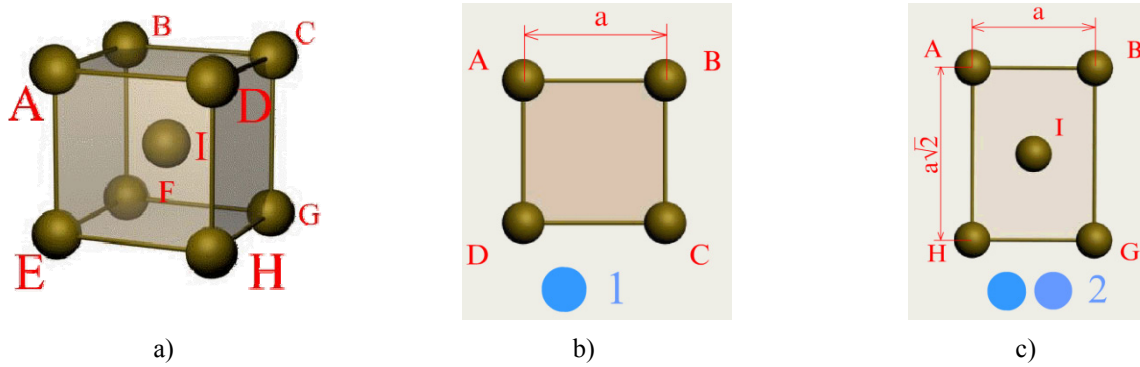


Fig.2. Volume-centric cubic lattice: a) unit cell of the bcc lattice; b) plane ABCD. The number of atoms in the plane ABCD – 1; c) plane ABGH. Number of atoms in the plane ABGH - 2

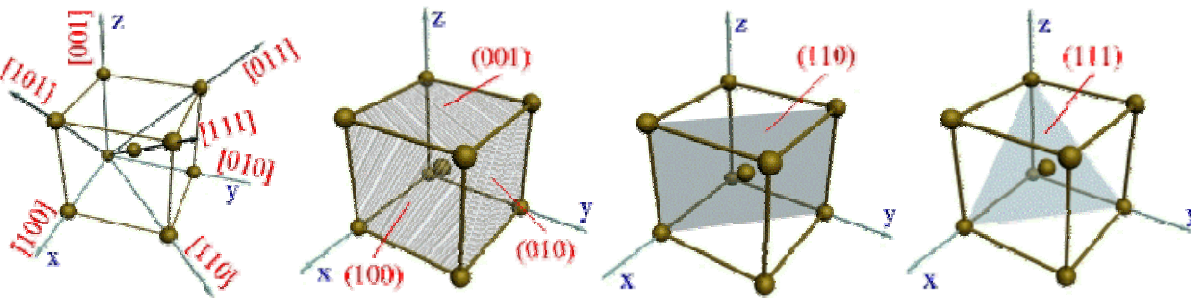


Fig.3. Crystallographic directions and planes in the crystal lattice: a) - the main directions and their designation; b), c), d) -basic planes and their designation

Table 2 shows that the body-centered cubic lattice $\text{Li} \rightarrow \text{Cs}$ in the (110) plane contains more atomic monolayers, and the (111) layer contains the smallest number of atomic monolayers. These layers are located in the R(I) layer (Fig. 1), where the relaxation or reconstruction of the single crystal surface occurs (Fig. 4) [13].

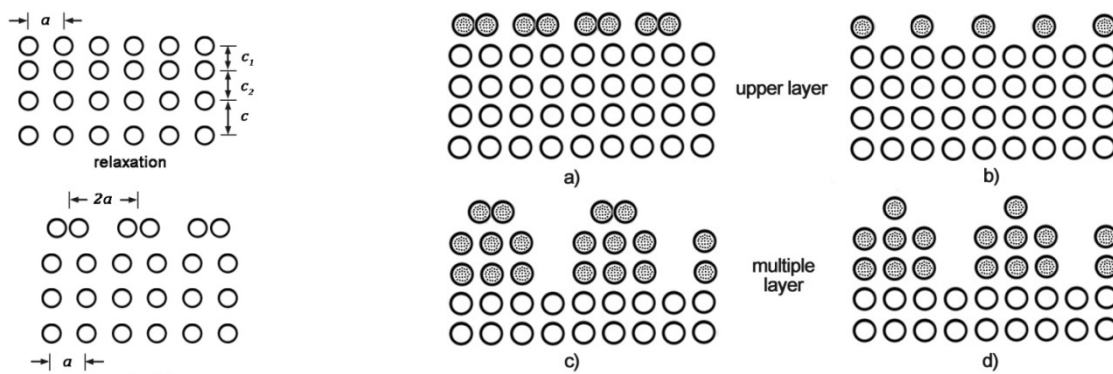


Fig.4. Transformation of the metal surface: relaxation — upper layer (a, b); reconstruction - several layers (c, d)

The relaxation of the surface is understood as the difference between the distances between the last crystallographic planes parallel to the plane of the interface with vacuum from the distances between the same planes in the volume (Fig. 4). The variety of cases when the atomic structure of the upper layer is modified is characterized by the term reconstruction (it is especially relevant for semiconductors). Relaxation is characteristic of metals. The same is expected for $\text{Li} \rightarrow \text{Cs}$ crystals, and from Table 2 it can be seen that the surface layer extends over several atomic monolayers (Fig. 4, right). On the whole, size effects are observed up to distances $R(\text{II}) \approx 9R = R_\infty$, where the bulk phase begins (Fig. 1), which, starting with potassium, exceeds the limit of 100 nm, which is characteristic of Slater nanostructures [19]. Table 2 shows

that the work function of electrons changes proportionally with a change in the surface energy of the metal. This means that the device developed by us [1, 2] can be used to measure the state of the metal surface and its anisotropy.

Conclusion

The anisotropy of the surface of its metals, even of atomically smooth surfaces, began to be developed relatively recently. First, this is due to an incomplete understanding of the role that surface energy and its anisotropy play in nanostructures. Secondly, because of the difficulty of measuring it. Our proposed model gives a numerical value for the thickness of the surface layer and allows one to evaluate the physical processes that occur in nanostructures. The de Broglie layer $R_0 = \lambda_{dB} = \hbar/p$ for metals ranges from 0.01 nm to 0.1 nm. Quantum dimensional effects begin in this layer. The main quantum-dimensional structures include structures with a two-dimensional electron gas - epitaxial films, MIS structures, heterostructures, etc.; structures with one-dimensional gas - quantum threads or wires; structures with zero-dimensional gas - quantum dots, boxes, crystallites. The R(I) layer is described by the first dependence from equation (9) ($r \gg R(I)$). In the R(I) layer with pure metal atoms, there is a reconstruction and relaxation associated with the rearrangement of the surface. The R(II) layer extends approximately to the size $R(II) \approx 9R = R_\infty$, where the bulk phase begins. Dimensional properties begin from this size. We have shown for the first time in the world that the thickness of the surface layer is determined by one fundamental parameter - the molar (atomic) volume of an element, which periodically changes in accordance with the table of D.I. Mendeleev.

Acknowledgments

The work was carried out under the program of the Ministry of Education and Science of the Republic of Kazakhstan Grant No. 0118RK000063.

REFERENCES

- 1 Yurov V.M., Oleshko V.S. The impact of the environment on the contact potential difference of metal machine parts. *Eurasian Physical Technical Journal*, 2019. Vol.16, No.1(31), pp. 99 – 108.
- 2 Yurov V.M., Makeeva O.V., Oleshko V.S., Fedorov A.V. Development of a device for determining work electron output. *Eurasian Physical Technical Journal*, 2020, Vol.17, No.1 (33), pp. 127 – 131.
- 3 Shebzukhova I. G., Arefieva L. P. Anisotropy of surface energy and the electron work function IIB of metals. *Journal of technical physics*, 2019, Vol. 89, Issue. 2, pp. 306 – 309.
- 4 Shebzukhova I. G., Arefieva L. P. Estimation of polarization and dispersion corrections to the surface energy of the faces of metal crystals. *Physicochemical aspects of studying clusters, nanostructures and nanomaterials*, 2020, Issue 12, pp. 319 – 325.
- 5 Bokarev V.P., Krasnikov G.Ya. Anisotropy of physicochemical properties of single-crystal surfaces. *Electronic technology. Series 3. Microelectronics*, 2016, No. 4(164), pp. 25 – 30.
- 6 Bochkarev V.P. *Development of physical and chemical principles for assessing the effect of surface energy on the properties of materials and processes for microelectronic technology*. Doctor Dissert. of Techn. Scinc. degree, Moscow, 2020. - 299 p.
- 7 Bernstein M.L., Rakhshadt A.G. *Element properties. Part 1. Physical properties*. Moscow, 1969, 600 p.
- 8 Jian Wang, Shao-Qing Wang. Surface energy and work function of FCC and BCC crystals: Density functional study. *Surface Science*, 2014, Vol. 630, pp. 216-224.
- 9 Vladimirov A.F. Anisotropy of the work function of the electron and reticular compaction of "loose" faces of metal crystals. *Surface, X-ray, synchrotron and neutron research*, 1999, No. 9, pp. 58 – 66.
- 10 Skriver H.L., Rosengaard N.M. Surface energy and work function of elemental metals. *Physical Review B*, 1992, Vol. 46, No. 11, pp. 7157 – 7168.
- 11 Yurov V.M., Guchenko S.A., Laurinas V.Ch. Surface layer thickness, surface energy, and atomic volume of an element. *Physicochemical aspects of studying clusters, nanostructures and nanomaterials*, 2018, Vol. 10, pp. 691-699.
- 12 Arutyunov K.Yu. Quantum size effects in metallic nanostructures. *RAS reports*. 2015. No. 3(28), pp. 7 – 16.
- 13 Oura K., Lifshits V.G., Saranin A.A., et al. Katayama M. *Introduction to surface physics*. Moscow, 2006, 490 p.
- 14 Uvarov N.F., Boldyrev V.V. Size effects in the chemistry of heterogeneous systems. *Uspekhi khimii*, 2001, Vol. 70(4), pp. 307 – 329. [in Russian]
- 15 Gusev A.I. *Nanomaterials, nanostructures, nanotechnology*. Moscow, 2005, 412 p. [in Russian]
- 16 Andrievsky R.A., Ragulya A.V. *Nanostructured materials*. Moscow, 2005, 192 p. [in Russian]
- 17 Suzdalev I.P. *Nanotechnology: physical chemistry of nanoclusters, nanostructures and nanomaterials*. Moscow, 2006, 592 p. [in Russian]
- 18 Kiselev V.F., Kozlov S.N., Zoteev A.V. *Fundamentals of Solid Surface Physics*. Moscow, 1999, 284 p.
- 19 Gleiter H. Nanostructured materials: basic concepts and microstructure. *Acta mater*. 2000, Vol. 48, pp. 1 – 29.

DOI 10.31489/2021No1/16-28

UDC 539.199, 544.723.2

REARRANGEMENT OF THE CONFORMATIONAL STRUCTURE OF POLYAMPHOLYTES ON THE SURFACE OF A METAL NANOWIRE IN A TRANSVERSE MICROWAVE ELECTRIC FIELD

Kruchinin N. Yu., Kucherenko M.G.

Center of Laser and Informational Biophysics, Orenburg State University, Orenburg, 460018 Russia,
kruchinin_56@mail.ru, clibph@yandex.ru

Molecular dynamics has been employed to study the rearrangement of the conformational structure of polyampholytes adsorbed on the surface of a gold nanowire with a periodic change in time of its polarity in the transverse direction at an ultrahigh frequency. The radial distributions of the atomic density of the polypeptide and its angular distributions on the nanowire surface have been calculated. At high temperatures, temporary fluctuations in the conformational structure of the adsorbed polyampholyte polypeptide were observed. In this case, for half the period of the nanowire polarity change, the macrochain conformation changed from dense enveloping of the nanowire to an elongated conformational structure along the dipole moment of the nanowire. At low temperature and the nanowire dipole moment, the swelling of the fringe of the adsorbed polyampholyte was observed with a displacement of most of its links to one side with respect to the plane perpendicular to the direction of the nanowire dipole moment and passing through its axis. At low temperature and high values of the nanowire dipole moment, the polyampholyte polypeptide was desorbed from the nanowire surface. An analytical model of conformational rearrangements of a polyampholyte Gaussian chain in the form of an external field perturbation theory is presented.

Keywords: polyampholytes, metal nanowire, conformational changes, molecular dynamics, microwave electric field

Introduction

Hybrid nanosystems consisting of plasmonic nanoobjects, in particular, gold nanorods and nanowires with adsorbed macromolecular chains, are widely used as elements of nanoelectronic devices, as well as in the creation of various chemical sensors [1-7]. At present, considerable efforts have been focused on increasing the sensitivity and expanding the possibilities of detecting sensors based on the effect of surface plasmon resonance and surface-enhanced Raman scattering based on such hybrid nanosystems. In this case, both photoactive molecules and plasmonic nanoparticles must be bound to the macrochain [8-13]. Of particular interest is the control of changes in the conformational structure of adsorbed polyampholytes on a conducting surface both by a static electric field and by electromagnetic radiation.

In an electric field, the conformational structure of a polyampholytic macrochain adsorbed on a solid surface will change under its influence [14-18]. When transverse electric field is imposed on a cylindrical metal nanowire, electric charges are induced on its surface, with their surface density being distributed in proportion to the cosine of the angle between the directions of the electric field vector and the normal to the nanowire surface. The arising field of the induced polarization strongly distorts the primary electric field near the nanowire. Such an uneven distribution of induced charges on the surface of a nanowire will have a significant effect on the conformational structure of polyampholyte macrochains adsorbed on its surface.

In the case of exposure to electromagnetic radiation on a nanowire, in which the electric field vector that is variable along the length remains perpendicular to its axis, the conformational structure of the polyampholyte macrochain will change in accordance with fluctuations in the density of charges induced by this field on the nanowire surface. Such a rearrangement of the conformational structure of the macromolecule near the nanowire becomes possible upon excitation of field oscillations in it in the microwave range in the direction transverse to the axis. At certain frequencies of electromagnetic radiation, a resonance of changes in the conformational structure of a polyampholyte macromolecule on the surface of a metal nanowire may appear [18].

In this work, circular-section gold nanowires are considered as metal adsorbents for polypeptides in connection with the specific properties of conducting nanocylinders as promising plasmonic nanoantennas. Similar objects with axial geometry are carbon nanotubes, the plasmon properties of which were considered by the authors in [19-20], where it was shown that such nanotubes perform the functions of a kind of electromagnetic waveguides. One-dimensional plasmon-polaritons can propagate along the surface of a conducting cylinder parallel to its axis, while only localized surface plasmons with well-studied properties can form in nanoparticles of a finite volume. Spherical metal nanoparticles with adsorbed polypeptide macrochains were considered by us earlier in [14, 16-18].

Therefore, such hybrid nanosystems, in which the conformational structure of adsorbed polyampholytes on the surface of a gold nanowire or nanorod can be rearranged under the influence of both a static electric field and a variable with an ultrahigh frequency, can find application in the creation of new and modification of existing sensors based on the effect of surface-enhanced Raman scattering or surface plasmon resonance, as well as luminescent optical units for measuring the concentration of molecular oxygen [21-22].

The goal of this work is to study the rearrangement of the conformational structure of polyampholyte polypeptides on the surface of a gold nanowire under the influence of electromagnetic radiation, in which the electric field vector is directed in the transverse direction with respect to the nanowire axis.

3. Molecular dynamic simulation

Molecular dynamics (MD) simulation of polyampholytic polypeptides on the surface of a gold nanowire was performed using the NAMD 2.14 software package [23]. The model of a gold nanowire was obtained by cutting out a cylinder with a radius of 1.5 nm and a length of 15.5 nm from a gold crystal, while the atoms of the nanowire remained fixed during the MD simulation.

Four polyampholytic polypeptides with different orders of charged amino acid residues were examined:

1) A400R100D100 polypeptide consisting of 400 Ala units (A), 100 Arg units (R, charge of $+1e$), and 100 Asp units (D, charge of $-1e$), with the two latter being uniformly distributed over the chain, with the total number of amino acid residues being equal to $600 - (ADA_2RA)_{100}$;

2) A480R60D60 polypeptide consisting of 480 Ala units, 60 Arg units, and 60 Asp units, with the two latter being uniformly distributed over the chain, with the total number of amino acid residues being equal to $600 - (A_2DA_4RA_2)_{60}$;

3) A784R98D98 polypeptide consisting of 784 Ala units, 49 pairs of Arg units, and 49 pairs of Asp units, with the two latter being uniformly distributed over the chain, with the total number of amino acid residues being equal to $980 - (A_4R_2A_8D_2A_4)_{49}$;

4) A880R54D54 polypeptide consisting of 880 Ala units, 27 pairs of Arg units, and 27 pairs of Asp units, with the two latter being uniformly distributed over the chain, with the total number of amino acid residues being equal to $988 - A_8(A_8D_2A_{16}R_2A_8)_{27}A_8$.

The CHARMM22 force field [24] was used for the polypeptides. Noncovalent interactions with the gold nanoparticle were described by the Lennard-Jones potential parameterized in [25]. The van der Waals potential was cut off at a distance of 1.2 nm using the smoothing function between 1.0 and 1.2 nm. Electrostatic interactions were calculated directly at a distance of 1.2 nm; for larger distances, the particle mesh Ewald (PME) method [26] with a mesh step of 0.11 nm was employed. The entire nanosystem was placed in a cube with edges of 24 nm, filled with TIP3P water molecules [27].

At the initial moment of time, the polypeptide macromolecule was located in the form of a nonequilibrium coil near the surface of an unpolarized cylindrical gold nanowire. Three different starting coils were considered for each polypeptide. The MD simulation has yielded three equilibrium conformational structures for each considered polypeptide. The formation of equilibrium conformations was controlled by monitoring variations in the root-mean-square distance (RMSD) between atoms of a polypeptide in different conformations. Subsequently, these structures were used as starting configurations for MD simulation on the surface of a transversely polarized nanowire.

In the case of uniform polarization of the nanowire in the transverse direction, the local electric field was set through the change in the atomic charges on the surface of the cylindrical nanowire according to the cosine law in the cross section. The following induced dipole moment of the nanowire per unit length were obtained: $p_{1\max}^{nw} = 1.5kD/nm$, $p_{2\max}^{nw} = 3.0kD/nm$ и $p_{3\max}^{nw} = 6.0kD/nm$. In this case, in the positively charged region of the polarized nanowire, the atoms acquired the maximum electric field-induced partial charges equal $+0.25e$, $+0.5e$ and, $+1.0e$, accordingly. At the first stage, MD simulation was carried

out with transverse polarization of the nanowire in a static electric field for all the considered polypeptides until an equilibrium conformational structure was obtained.

At the second stage, during the MD simulation, the densities of charges on the nanowire surface were periodically varied with time according to the sine law with oscillation period $T = 2.4$ ns (oscillation frequency of 416.7 MHz) for 3 oscillation periods. Each oscillation period was divided into 8 equal time periods of 0.3 ns, during which the field remained unchanged, and the dipole moment of the nanowire in a selected period was set by averaging it over the entire period duration. The dipole moment of the nanowire changed in the following sequence, starting from the starting conformation of the polypeptide obtained on an unpolarized nanowire: $+0.69p_{\max}^{nw}$ (average value in the oscillation region from $\pi/8$ to $3\pi/8$), $+0.97p_{\max}^{nw}$ (from $3\pi/8$ to $5\pi/8$), $+0.69p_{\max}^{nw}$ (from $5\pi/8$ to $7\pi/8$), 0 (from $7\pi/8$ to $9\pi/8$), $-0.69p_{\max}^{nw}$ (from $9\pi/8$ to $11\pi/8$), $-0.97p_{\max}^{nw}$ (from $11\pi/8$ to $13\pi/8$), $-0.69p_{\max}^{nw}$ (from $13\pi/8$ to $15\pi/8$), and 0 (from $15\pi/8$ to $17\pi/8$) [18]. The MD simulation was carried out at constant temperatures of 300 and 900 K (Berendsen thermostat) for each considered polypeptide.

Based on the obtained results of MD simulation, the radial dependences of the density of atoms of polypeptides were calculated, as well as the angular distributions of atoms of polypeptides with a step of 10 degrees over the cross section.

4. Results of the study

According to the results of MD simulation of polypeptides on the surface of an unpolarized gold nanowire, it was found that the polypeptides partially envelop the nanowire (Fig. 1a). The predominance of the location of the amino acid residues of the polypeptide on one side or the other of the nanowire depended on the starting location of the non-equilibrium macrochain coil, while the adsorption of polypeptide residues occurred regardless of their type. The radial distributions of the average density of polypeptide atoms (Fig. 2a) had a characteristic shape with a peak of the radial density distribution near the nanowire surface. The average angular distributions of polypeptide atoms over the cross section according to all the results of the MD simulation indicated a generally uniform distribution of atoms around the nanowire.

On the surface of a transversely polarized gold nanowire in a static electric field, such a rearrangement of the conformational structure of the adsorbed polyampholyte macrochain took place, in which, as the value of the induced dipole moment of the nanowire per unit of its length increased, more and more Asp amino acid residues were displaced toward the surface in the positively charged region of the nanowire (at the top in Figs. 1b and 1c), and Arg amino acid residues were displaced to the surface in the negatively charged region of the nanowire (below in Figs. 1b and 1c). In this case, the stretching of the macromolecular fringe along the dipole moment in the transverse direction to the nanowire was observed due to the repulsion of the residues of the same name with respect to the surface in the polar regions of the nanowire (Figs. 1b and 1c). This is most pronounced in polypeptides with a large distance between opposite charged amino acid residues in the macrochain.

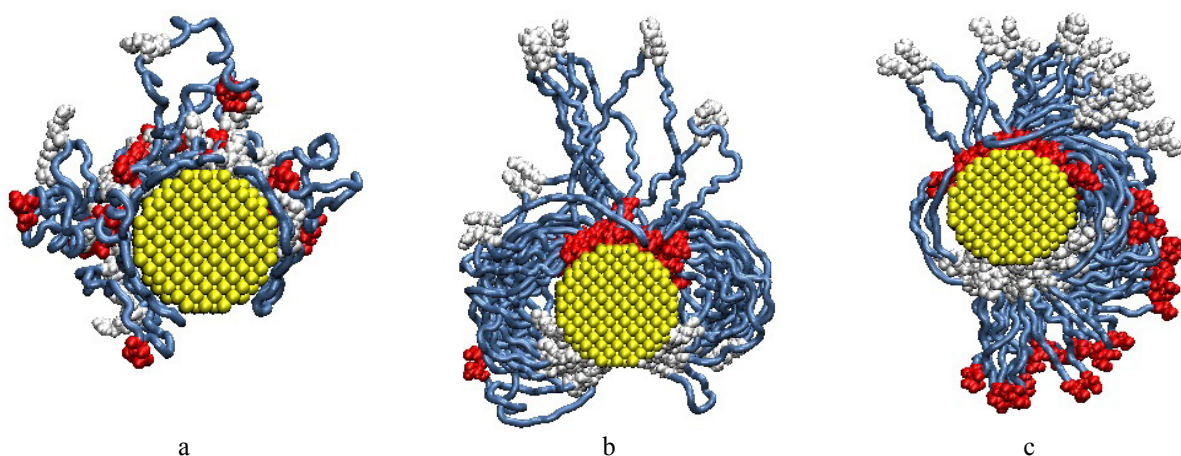


Fig.1. Polypeptide A880R54D54 on the surface of an unpolarized gold nanowire (a), polypeptides A880R54D54 (b) and A784R98D98 (c) on the surface of a polarized nanowire in a static electric field in the transverse direction (the dipole moment of the nanowire is directed upwards) after MD simulation (end view; the blue tube and white and red symbols denote Ala, Arg, and Asp residues, respectively).

The radial distributions of the average density of polypeptide atoms on the surface of a polarized nanowire also differ from the case of adsorption on an unpolarized nanowire. Figure 2b shows that the peak value of the radial distribution over all polypeptide atoms decreased by more than 5 times, and the profile of this distribution broadened significantly. This is due to the fact that the peaks of the radial distribution of the average density of the charged Arg and Asp amino acid residues of the polypeptide are located at the surface of the nanowire, and the profile of the radial distribution of the average density of Ala units is shifted from the surface. Figure 2c shows the average angular distributions of atoms of charged units of a polypeptide on the surface of a gold nanowire polarized in the transverse direction. The upper pole in Figure 1 along the cross-section of the nanowire corresponds to an angle of 0 degrees, and the lower pole corresponds to an angle of 180 degrees. It can be seen that a redistribution of Arg amino acid residues to the negatively charged region of the nanowire occurred on the polarized nanowire, and Asp units shifted to the positively charged region of the nanowire. The ratio of the thickness of the macromolecular fringe along the dipole moment of the nanowire to the thickness of the macromolecular layer in the orthogonal transverse direction was 1.4, 1.6, 1.9, and 2.2 times, respectively, for the A400R100D100, A480R60D60, A784R98D98, and A880R54D54 polypeptides. That is, the greater the distance between opposite charged links in the macrochain, the greater this ratio.

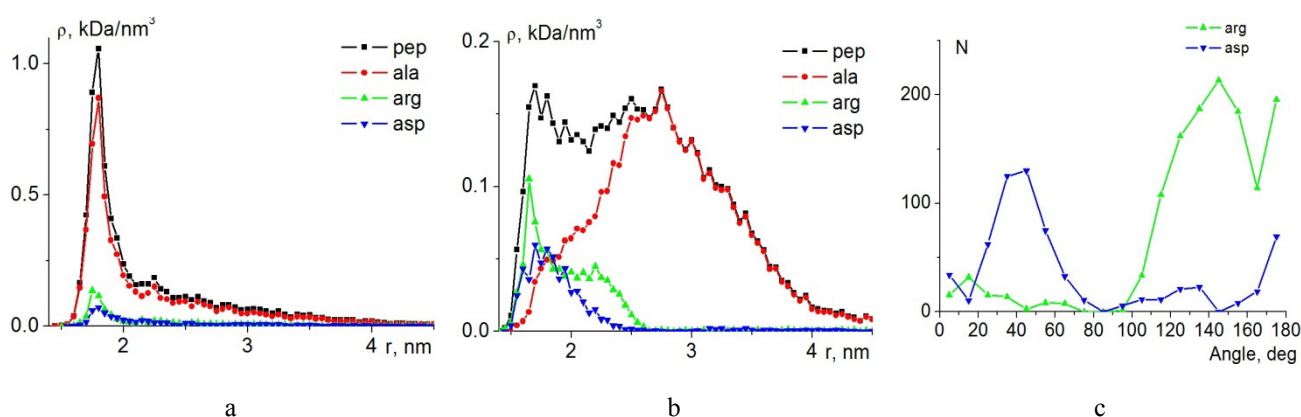


Fig.2. Radial dependences of the average atomic density for A880R54D54 polypeptide on the surfaces unpolarized (a) and polarized in a static electric field in the transverse direction (b) gold nanowires with differentiation by the types of units. Dependences of the average angular distributions of atoms of charged units of the A880R54D54 polypeptide on a polarized gold nanowire (c). In the figure: pep - dependence for all atoms of the polypeptide; ala, arg and asp - dependences by types of amino acid residues.

According to the results of MD simulation with a temperature of 900 K with periodic changes in the polarization of the nanowire in the transverse direction, oscillations of the conformational structure of polyampholyte adsorbed on the surface were observed, similar to the temporal oscillations of conformations on the surface of a metal nanoparticle [18]. Such oscillations began to be clearly observed at the peak values of the induced dipole moment of the nanowire per unit of its length $p_{2\max}^{nw}$ and higher for all the considered polypeptides, and at lower values of the dipole moment they were less pronounced. Figure 3 shows the conformational structures of the A784R98D98 polypeptide on the surface of the nanowire at different times according to the results of MD simulation with a peak dipole moment $p_{2\max}^{nw}$.

It can be seen that for different directions of the dipole moment (Figs. 3a and 3b), the conformational structure has a mirror-like appearance with respect to the horizontal plane passing through the nanowire axis. It can also be seen that these conformational structures have a similar appearance to the conformational structure obtained as a result of MD simulation in a static field (Fig. 1c) with stretching the loops along the direction of the dipole moment. Figure 3c shows the final conformational structure of the A784R98D98 polypeptide, obtained as a result of MD simulation at the last time interval, when the nanowire dipole moment was zero. In this case, the polypeptide completely envelops the gold nanowire and has a similar appearance to the starting conformations on the surface of an unpolarized nanowire (Fig. 1a).

The radial distributions of the atomic density of the A784R98D98 polypeptide with differentiation by the types of units, averaged over all time intervals in the cases when the nanowire is not polarized (Fig.4a), polarized with a dipole moment $+0.97p_{2\max}^{nw}$ (Fig.4b), and $-0.97p_{2\max}^{nw}$ (Fig.4c), also have a similar form

with radial distributions obtained on an unpolarized nanowire (Fig. 2a) and with polarization in a static electric field (Fig. 2b), respectively. In this case, the radial distributions of the average density of polypeptide atoms for opposite directions of the transverse polarization of the nanowire are similar to each other (Figs. 4b and 4c). On the curves for the radial density distributions over all atoms of the A784R98D98 polypeptide show the vertical segments of the standard deviations. It can be seen that at the same phase of the change in the dipole moment of the nanowire, the deviations from the average value of the density of polypeptide atoms are small.

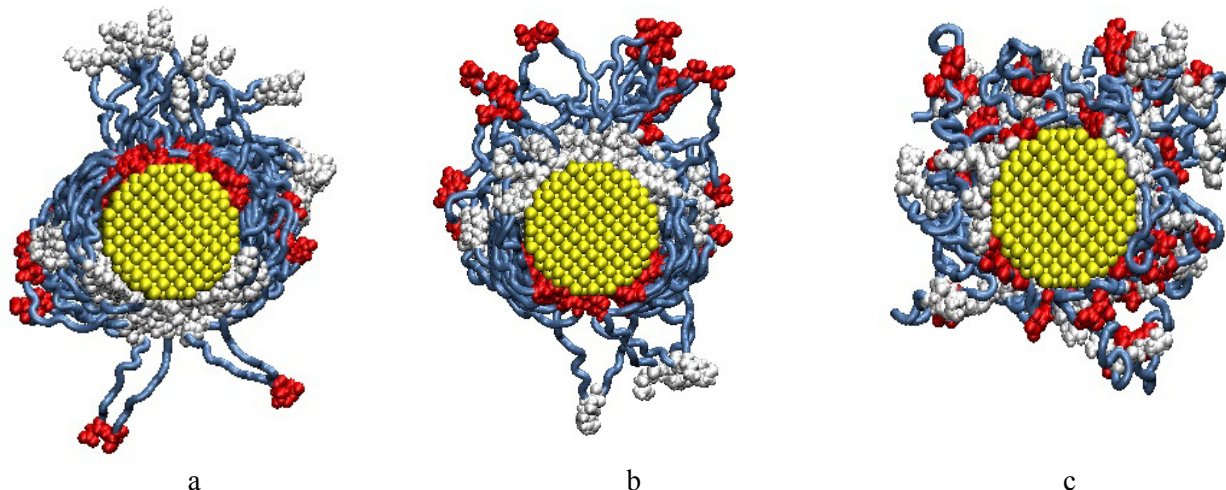


Fig.3. Conformations of the A784R98D98 polypeptide during MD simulation with a periodic change in the nanowire polarization in the transverse direction at a temperature of 900 K: a) after 5.4 ns, when the nanowire dipole moment is directed upward; b) after 6.6 ns, when the dipole moment of the nanowire is directed downward; c) after 7.2 ns, when the nanowire is not polarized.

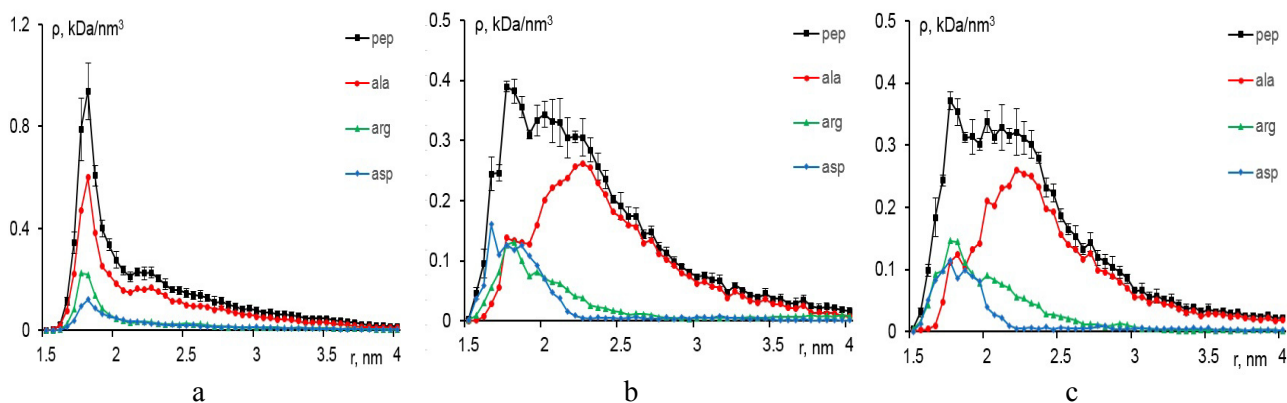


Fig.4. Radial distributions of the average density of atoms of the A784R98D98 polypeptide on the surface of a gold nanowire at the end of the MD simulation at 900 K on time intervals in cases where the nanowire is not polarized (a), is polarized in the transverse direction with a dipole moment $+0.97 p_{2\max}^{nw}$ (b) and $-0.97 p_{2\max}^{nw}$ (c). In the figure: vertical segments - an estimate of the standard deviation.

Figure 5 shows the dependences of the angular distributions of atoms of charged amino acid residues of polypeptides A784R98D98 (Fig.5a) and A880R54D54 (Fig.5b) averaged over time intervals with different values of the dipole moment of the nanowire.

It can be seen that, in the case of an unpolarized nanowire, charged amino acid residues Arg and Asp are almost uniformly distributed over the surface, and when the direction of the dipole moment of the nanowire is reversed, the peaks of the angular distributions of the charged units of the polypeptide change in a mirror image. All this means that, in MD simulations at a temperature of 900 K, with a periodic change in the polarization of the nanowire in the transverse direction, the conformational structure of the adsorbed polypeptide on the surface of the metal nanowire periodically changes from a dense enveloping of the nanowire to an elongated conformational structure in the transverse direction to the nanowire twice during one oscillation period.

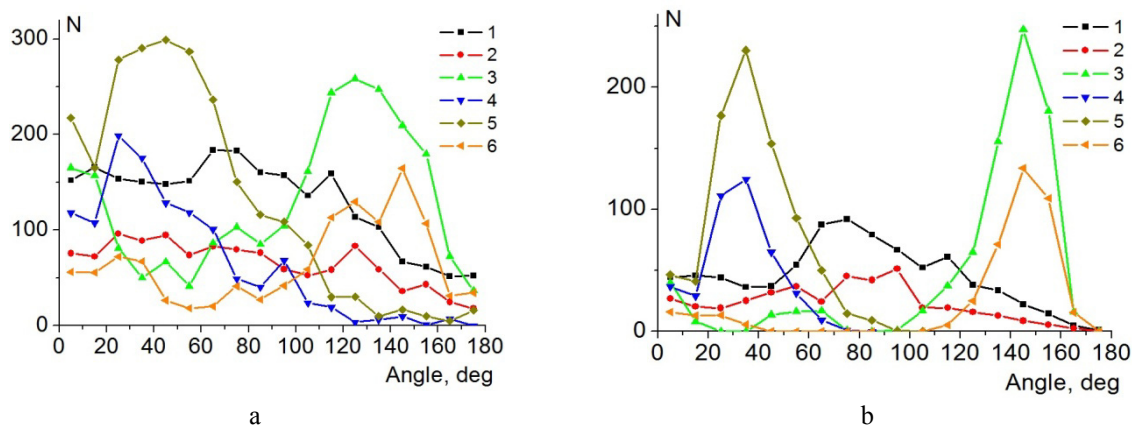


Fig.5. Dependences of the average angular distributions of the atoms of the charged Arg (1, 3, 5) and Asp (2, 4, 6) units of the A784R98D98 (a) and A880R54D54 (b) polypeptides over all conformations at the end of the MD simulation at 900 K on time intervals when nanowire is not polarized (1, 2), polarized in the transverse direction with a dipole moment $+0.97p_{2\max}^{nw}$ (3, 4) and $-0.97p_{2\max}^{nw}$ (5, 6)

According to the results of MD simulation with a periodic change in time of the polarity in the transverse direction of a gold nanowire with a temperature of 300 K at the peak value of the dipole moment of the nanowire $p_{1\max}^{nw}$, a displacement of the links of the adsorbed polyampholyte polypeptide to one side with respect to the plane perpendicular to the direction of the dipole moment of the nanowire and passing through its axis was observed (Fig. 6). The shift took place in the direction (Fig. 6b), where most of the polypeptide units were in the starting conformation (Fig. 1a). In this case, the swelling of the fringe of the adsorbed macrochain occurred, which can be seen if we compare the radial distributions of polypeptide atoms at the end of the MD simulation at 300 K (Fig. 6e) with the radial density distributions on the surface of the unpolarized nanowire (Figs. 2a and 4a). It can be seen that the peaks of radial distributions for the final conformations of polypeptides obtained at a temperature of 300 K are located at the surface of the nanowire (Fig. 6e), but they are several times lower than on the surface of an unpolarized nanowire.

The dependences of the angular distributions of the atoms of the adsorbed polypeptides (Figs. 6c and 6d) show that most of the polypeptide units are on the same side with respect to the horizontal plane passing through the nanowire axis. In this case, the peaks of the angular distributions are in this plane (angle 90 degrees). This region of the nanowire always remains neutral in the process of polarization reversal, and in the adjacent regions from above and below (Figs. 6a and 6b), the surface charges change insignificantly compared to the polar regions (angles of 0 and 180 degrees).

This nature of conformational changes is explained by the fact that at a low temperature of MD simulation, the forces arising as a result of the action of the local electric field are insufficient to overcome the mutual attraction between the polyampholyte links in the weakly charged region of the nanowire. When the nanowire is repolarized in the polar regions along the cross section, strong conformational changes in the macrochain occur, which lead to the fact that the links shift from one pole to the other and, passing through the weakly charged region, are localized in it. In contrast to the case of a spherical nanoparticle [18], where an annular macromolecular fringe was formed, encircling it in the equatorial region, the nanowire has an extended structure. Therefore, a part of the polypeptide units remains in the polar region, which bind amino acid residues, most of which are adsorbed in the weakly charged region (in Figures 6a and 6b, on the left and right of the nanowire).

At higher values of the peak dipole moment of the nanowire for the A400R100D100 and A480R60D60 polypeptides at $p_{3\max}^{nw}$, and for the A784R98D98 and A880R54D54 polypeptides at $p_{2\max}^{nw}$, desorption of polyampholyte from the nanowire surface took place. In this case, at the first steps of MD simulation, a conformational structure of the macrochain was formed, similar to the conformations obtained at lower peak values of the dipole moment of the nanowire (Fig. 6). However, then, due to a stronger change in the local electric field, the amplitude of the displacement of charged units in the weakly charged region of the nanowire increased. This led to the fact that the forces of attraction of the macrochain to the nanowire were overcome.

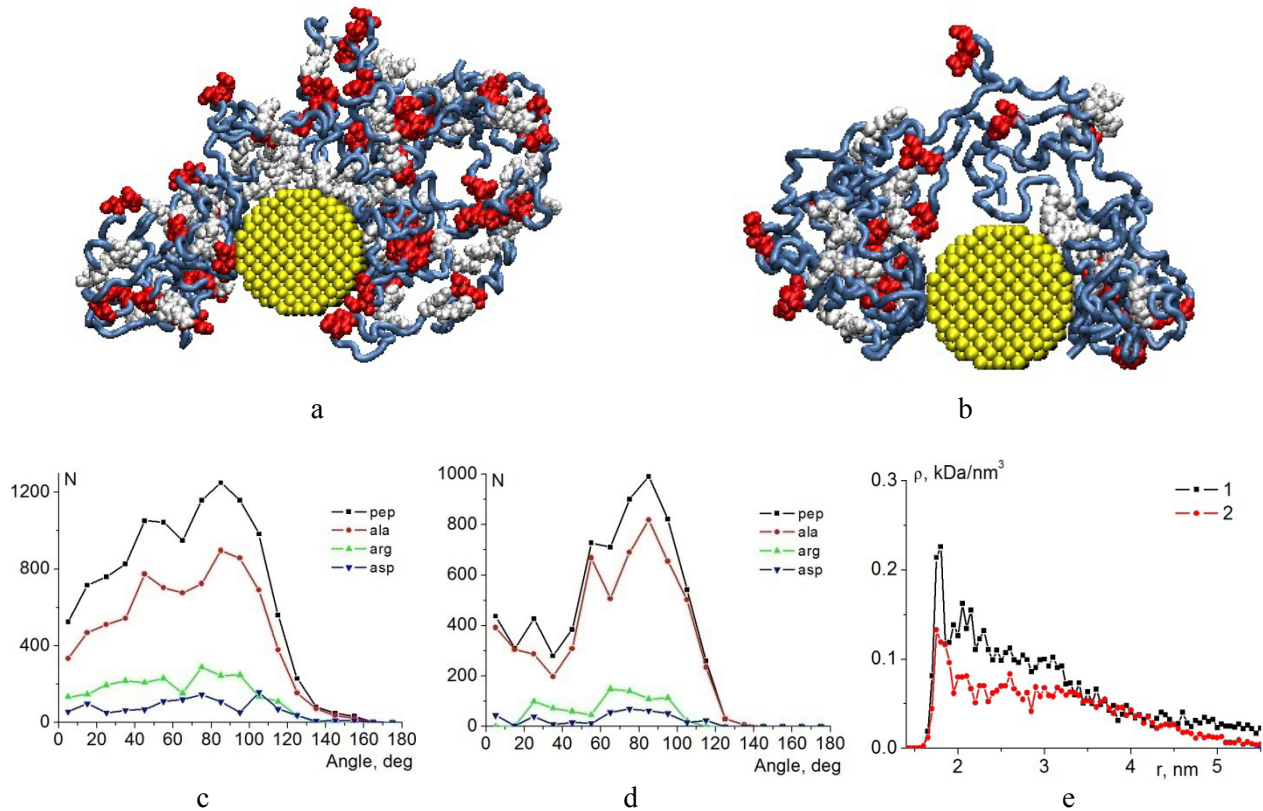


Fig.6. Conformations and dependences of the angular distributions of atoms of polypeptides A784R98D98 (a, c) and A880R54D54 (b, d), as well as radial distributions of atomic density (e) of polypeptides A784R98D98 (1) and A880R54D54 (2) after the end of MD simulation with periodic changes polarity of the nanowire in the transverse direction at a temperature of 300 K.

At the same time, due to the generally lower mobility of the links in comparison with the case of the higher temperature of the MD simulation, the movement of charged links between the poles of the nanowire along the cross section did not occur, and the macrochain was gradually desorbed from the surface.

5. Analytical model of conformational structure

Thus, the performed MD simulation showed that the change in the conformations of the macrochains of polyampholyte or polyelectrolyte adsorbed on the nanowire can be carried out by an external electric field polarizing the conductor. In the characteristic case of the transverse orientation of the external homogeneous monochromatic (at frequency ω) field intensity vector $\mathbf{E}(t) = \mathbf{E}_0 \exp(-i\omega t)$ relative to the z-axis of the cylinder, forced oscillations of the surface charge density occur – localized plasmons. In the simplest model, polymer molecules are represented by ideal Gaussian chains, but the attraction of the units to the adsorbent surface is taken into account. Such a model has great clarity, therefore it is convenient for analyzing changes in the conformational structure of the chain with a change in external conditions.

The intensity of the quasi-static field outside a cylinder of radius R , i.e. when $r > R$ and placing it in the field \mathbf{E}_0 has the form [28]

$$\mathbf{E}_2(r, \varphi) = E_0 \mathbf{n}_x + E_0 \frac{\varepsilon_1(\omega) - \varepsilon_2}{\varepsilon_1(\omega) + \varepsilon_2} \frac{R^2}{r^2} \left[(1 - 2 \sin^2 \varphi) \cdot \mathbf{n}_x + \sin 2\varphi \cdot \mathbf{n}_y \right]. \quad (1)$$

In the case of a circularly polarized monochromatic electromagnetic field propagating along the z axis, parallel to the axis of the nanocylinder

$$\mathbf{E}(t, z) = (E_0 \mathbf{n}_x + iE_0 \mathbf{n}_y) \exp(i\Omega t - ikz). \quad (2)$$

Here, in (2), \mathbf{n}_x , \mathbf{n}_y are the unit vectors of the coordinate Cartesian axes x and y. In the long-wavelength limit for the wavenumber $k \rightarrow 0$, the phases kz , $k(z + \Delta z)$ of wave (2) differ little from each other, and

over the length $l \ll 1/k$ we obtain an electric field of strength E_0 rotating with frequency Ω . In [29], a variant of the circular polarization of the microwave field in the problem of a cylinder with adsorbed macrochains was considered. In the adiabatically slow version of the field rotation, it is necessary that the frequency Ω be much lower than the characteristic frequencies of conformational transitions of macrochain fragments ~ 1 GHz (1 ns^{-1}).

The adsorption potential of the surface of a circular nanowire in the case of van der Waals adsorption can be effectively represented by a combination of the simplest model potentials “solid wall – delta-functional well”: $V_1(r) = V_\infty(R) - \alpha\delta(r - r_0)$ (R is the radius of the cylinder) [29]. When a nanowire is placed in a uniform electric field, its potential, as a result of the polarization of the conductor, becomes dependent on the angular variable φ in the cross-sectional plane. In an alternating monochromatic microwave field $\mathbf{E}(t) = E_0(\mathbf{n}_x + i\mathbf{n}_y)\exp(i\Omega t)$, there is a change in polarization according to a harmonic law with frequency Ω , and the potential $-eE_0r \cos(\varphi - \Omega t)$ of the external field $\mathbf{E}_x(t)$ is added to the adsorption potential $V_1(r)$, as well as the potential V_p of the field of the polarized surface of the nanocylinder: $V_2(r, \varphi, \Omega t) = -eE_0r \cos(\varphi - \Omega t) + V_p(r, \varphi - \Omega t)$. Then the potential of the total field in the space outside the nanowire with the polarized component $\mathbf{E}_x(t)$ can be written in the form

$$V(\mathbf{r}, t) = V_1(r) + V_2(r, \Phi(t)) = V_\infty(R) - \alpha\delta(r - r_0) - eE_0r \cos\Phi + V_p(r, \Phi), \quad (3)$$

where phase $\Phi(t) = \varphi - \Omega t$, and

$$V_2(r, \Phi) = -eE_0r \cos\Phi + \frac{\varepsilon_1(\omega) - \varepsilon_2}{\varepsilon_1(\omega) + \varepsilon_2} R^2 eE_0 \frac{\cos\Phi}{r} \quad (4)$$

- the energy of interaction of the polyelectrolyte link carrying the charge e with the primary external electric field and the polarization field of the wire. The dielectric constants $\varepsilon_1(\omega), \varepsilon_2$ in (4) characterize the metal of the nanowire and the environment, respectively. The intensity of the quasi-static field $\mathbf{E}_2(r, \varphi, t) = -\nabla V_2 / e$ outside the cylinder, i.e. for $r > R$, when placed in a field $\mathbf{E}(t)$ with circular polarization takes the form

$$\begin{aligned} \mathbf{E}_2(r, \varphi, t) = & E_0\mathbf{n}_x \cos\Omega t + E_0\mathbf{n}_x \frac{\varepsilon_1(\omega) - \varepsilon_2}{\varepsilon_1(\omega) + \varepsilon_2} \frac{R^2}{r^2} \left[(1 - 2\sin^2\varphi) \cdot \cos\Omega t + \sin 2\varphi \cdot \sin\Omega t \right] + \\ & + E_0\mathbf{n}_y \sin\Omega t + E_0\mathbf{n}_y \frac{\varepsilon_1(\omega) - \varepsilon_2}{\varepsilon_1(\omega) + \varepsilon_2} \frac{R^2}{r^2} \left[\sin 2\varphi \cdot \cos\Omega t - (1 - 2\sin^2\varphi) \cdot \sin\Omega t \right]. \end{aligned} \quad (5)$$

At $\Omega \rightarrow 0$, the circularly polarized field (5) transforms into a static field (1) with linear polarization.

In the case of macrochain polyampholyte, instead of the charge e of the link, one can introduce the effective dipole moment \mathbf{p} of the electrically neutral group of links. Using (5) we can write down the energy $V_2^p = -\mathbf{p}\mathbf{E}_2(r, \varphi, t)$ of interaction of the field $\mathbf{E}_2(r, \varphi, \Omega t)$ with the dipole moment \mathbf{p} of the polyampholyte.

In the case of a weak microwave field, taking into account potentials $V_2(r, \Phi)$ (4) and $V_2^p = -\mathbf{p}\mathbf{E}_2(r, \varphi, t)$ with field (5) when constructing an analytical model of rearrangement of the conformational structure of a macrochain, as was done, for example, in [17, 29], can be performed within the framework of quasi-static perturbation theory.

Thus, this section presents an analytical model for the rearrangement of the conformational structure of polyampholytic and uniformly charged polypeptides on the surface of a transversely polarized gold nanowire. If necessary, the results obtained can be easily generalized, including for the case of rotation of the polarizing electric field vector. To solve a differential equation of Schrödinger type [30]

$$\frac{a^2 kT}{6} \nabla^2 \psi(\mathbf{r}) = [V(\mathbf{r}) - \varepsilon] \psi(\mathbf{r}), \quad (6)$$

where a is the size of the chain link that determines the conformational function $\psi(\mathbf{r})$; in the case of a weak microwave field, the potential (3) can be taken into account within the framework of perturbation theory. Equation (6) with potential (3) contains an angular variable, so it should be written in the form

$$\frac{\alpha^2 kT}{6} \left[\frac{1}{r} \frac{\partial}{\partial r} r \frac{\partial}{\partial r} + \frac{1}{r^2} \frac{\partial^2}{\partial \varphi^2} \right] \psi(\mathbf{r}) = [V(\mathbf{r}) - \varepsilon] \psi(\mathbf{r}). \quad (7)$$

Solution (7) can be represented as $\psi(\mathbf{r}) = F(r)\Phi_m(\varphi)$, where $\Phi_m(\varphi)$ is the eigenfunction of the projection operator of the quantum orbital angular momentum with integer m : $\Phi_m(\varphi) = 1/\sqrt{2\pi} \exp(im\varphi)$.

Then, taking into account the spectrum of eigenvalues for the functions $\Phi_m(\varphi)$

$$\frac{\partial^2 \Phi_m}{\partial \varphi^2} = -m^2 \Phi_m(\varphi), \quad (8)$$

for the radial function $F_l(r)$ we obtain the equation

$$\frac{\alpha^2 kT}{6} \left[\frac{1}{r} \frac{d}{dr} r \frac{d}{dr} - \frac{m^2}{r^2} \right] F_m(r) = [V(r) - \varepsilon_m] F_m(r). \quad (9)$$

Here in (9) the radial potential $V(r) = V_1(r) + V_2(r)$, and $V_2(r)$ is defined by the relation $V_2(r, \theta) = V_2(r)\Phi_1(\varphi)$, or

$$V_2(r, \varphi) = - \left[1 - \alpha'(\omega) \left(\frac{R}{r} \right)^2 \right] r E_0 \cos \varphi$$

$$V_2(r, \varphi) = -eE_0 r \cos \varphi + \frac{\varepsilon_1(\omega) - \varepsilon_2}{\varepsilon_1(\omega) + \varepsilon_2} R^2 eE_0 \frac{\cos \varphi}{r}$$

For ease of writing (4), it is assumed that the frequency $\Omega \rightarrow 0$ (quasi-static mode). For the function $F_m(r)$, we obtain the equation

$$F_m''(r) + \frac{1}{r} F_m'(r) - \frac{m^2}{r^2} F_m(r) = \frac{6}{\alpha^2 kT} [V_1(r) - \varepsilon_l] F_m(r), \quad (10)$$

which in the absence of potential $V_1(r) = V_\infty(R) - \alpha\delta(r - r_0)$ is the Bessel equation for cylindrical functions $Z_m(\xi)$. Thus, the solution to (10) is the Bessel functions of the imaginary argument $I_m(q_m r)$ and $K_m(q_m r)$, $\xi = q_m r$, $q_m^2 = -\frac{6\varepsilon_m}{\alpha^2 kT}$. As solutions to equation (6) with a certain index m in the field

$V(r) = V_1(r)$, decaying at infinity, we can write the following

$$\begin{cases} F_m^I(r) = A_m I_m(q_m r) + B_m K_m(q_m r), & R < r < r_0 \\ F_m^{II}(r) = C_m K_m(q_m r), & r_0 < r < \infty \end{cases} \quad (11)$$

Constants A_m , B_m and C_m we find from the considerations that ψ - functions must satisfy the following boundary conditions

$$\psi_I(R) = 0, \quad \psi_I(r_0) = \psi_{II}(r_0), \quad \psi'_{II}(r_0) - \psi'_I(r_0) = -\frac{6\alpha}{\alpha^2 kT} \psi_{II}(r_0). \quad (12)$$

The last equation allows you to determine a single discrete spectrum level ε_m for each m . For $m = 0$, we arrive at the problem with circular symmetry, which we have already investigated in a number of works. In the general case of an arbitrary index m to determine the parameters q_m and ε_m (the important

case $m = 1$), it is necessary to use the equation

$$\frac{d}{dr} F_m^{II}(r)|_{r=r_0} - \frac{d}{dr} F_m^I(r)|_{r=r_0} = -\frac{6\alpha}{a^2 kT} F_m^{II}(r_0). \quad (13)$$

From (12) we find the relations between the constants A_m , B_m and C_m :

$$B_m = -A_m \frac{I_m(q_m R)}{K_m(q_m R)}, \quad C_m = A_m \left[\frac{I_m(q_m r_0)}{K_m(q_m r_0)} - \frac{I_m(q_m R)}{K_m(q_m R)} \right]. \quad (14)$$

Then solutions (11) take the form

$$\begin{cases} F_m^I(r) = A_m \left[I_m(q_m r) - \frac{I_m(q_m R)}{K_m(q_m R)} K_m(q_m r) \right], & R < r < r_0 \\ F_m^{II}(r) = A_m \left[\frac{I_m(q_m r_0)}{K_m(q_m r_0)} - \frac{I_m(q_m R)}{K_m(q_m R)} \right] K_m(q_m r), & r_0 < r < \infty \end{cases} \quad (11')$$

Substituting (11') into (13) we obtain the general transcendental equation for the eigenvalues q_m

$$\frac{a^2 kT}{6\alpha r_0} = I_m(q_m r_0) K_m(q_m r_0) - K_m^2(q_m r_0) \frac{I_m(q_m R)}{K_m(q_m R)}. \quad (15)$$

For $m = 1$, from (11) we obtain

$$\begin{cases} \psi_I^{(m=1)}(r, \varphi) = [A_1 I_1(q_1 r) + B_1 K_1(q_1 r)] \Phi_1(\varphi), & R < r < r_0 \\ \psi_{II}^{(m=1)}(r, \varphi) = C_1 K_1(q_1 r) \Phi_1(\varphi), & r_0 < r < \infty \end{cases} \quad (16)$$

Note that the density $n(r, \varphi) = \psi^2(r, \varphi)$ of the units of the adsorbed macrochain will still be determined by functions (11) or their equivalent (11') with the index $m = 0$, but not (16), since the eigenvalues ε_1 corresponding to (16) have a larger modulus than ε_0 . In addition, let us pay attention to the fact that the first-order corrections to the eigenvalue ε_0 , taking into account the disturbance $V_2(r, \varphi) = -eE_0 r \cos \varphi + V_p(r, \varphi)$, are equal to zero for states (11) and (11'). Correct use of the Rayleigh-Schrödinger perturbation theory requires taking into account states (16) to refine the basic state $F_0(r)$.

Microwave perturbation theory

Taking into account the orthogonality $\Phi_m(\varphi)$ with different indices m and the structure of the angular dependence of the perturbation operator $V_2(r, \varphi) \sim \cos \varphi$, we note that only functions (16) with $m = 1$ will contribute to the basic state corrections $\psi_{I,II}^{(m=0)}(r)$. The corrected basic state $\psi_{I,II}^{(m=0)}(r)$ in the second order in the small parameter $\eta = eE_0 a / |\varepsilon_1 - \varepsilon_0|$ can be written as

$$\begin{cases} \psi_I(r, \varphi) = \psi_I^{(m=0)}(r) + \frac{\langle \psi_I^{(m=0)} | V_2 | \psi_I^{(m=1)} \rangle}{\varepsilon_1^{(0)} - \varepsilon_0^{(0)}} \psi_I^{(m=1)}(r, \varphi) - \frac{1}{2} C_I^{(2)} \psi_I^{(m=0)}(r), & R < r < r_0 \\ \psi_{II}(r, \varphi) = \psi_{II}^{(m=0)}(r) + \frac{\langle \psi_{II}^{(m=0)} | V_2 | \psi_{II}^{(m=1)} \rangle}{\varepsilon_1^{(0)} - \varepsilon_0^{(0)}} \psi_{II}^{(m=1)}(r, \varphi) - \frac{1}{2} C_{II}^{(2)} \psi_{II}^{(m=0)}(r), & r_0 < r < \infty \end{cases} \quad (17)$$

Expressions for the radial-angular distribution of the density of the units of the adsorbed Gaussian macrochain can be written in the form

$$n_I(r, \varphi) = n_I^{(m=0)}(r) + n_I^{(1)}(r) \cos \varphi + n_I^{(2)}(r) \cos^2 \varphi, \quad R < r < r_0, \quad (18)$$

$$n_{II}(r, \varphi) = n_{II}^{(m=0)}(r) + n_{II}^{(1)}(r) \cos \varphi + n_{II}^{(2)}(r) \cos^2 \varphi, \quad r_0 < r < \infty, \quad (19)$$

where

$$n_{I,II}^{(1)}(r) = 2 \frac{\langle \psi_{I,II}^{(m=0)} | V_2 | \psi_{I,II}^{(m=1)} \rangle}{\varepsilon_1^{(0)} - \varepsilon_0^{(0)}} F_0^{I,II}(r) F_1^{I,II}(r), \quad n_{I,II}^{(2)}(r) = \frac{|\langle \psi_{I,II}^{(m=0)} | V_2 | \psi_{I,II}^{(m=1)} \rangle|^2}{|\varepsilon_1^{(0)} - \varepsilon_0^{(0)}|^2} |F_1^{I,II}(r)|^2.$$

We find the eigenvalues ε_1 from the equation $\varepsilon_1 = -q_I^2 a^2 kT / 6$, and the coefficients $\langle \psi_{I,II}^{(m=0)} | V_2 | \psi_{I,II}^{(m=1)} \rangle$ are the following integrals

$$\langle \psi_{I,II}^{(m=0)} | V_2 | \psi_{I,II}^{(m=1)} \rangle = \begin{cases} \int_R^{r_0} F_0^I(r) V_2(r) F_1^I(r) r dr, & I : R < r < r_0 \\ \int_{r_0}^{\infty} F_0^{II}(r) V_2(r) F_1^{II}(r) r dr, & II : r_0 < r < \infty \end{cases}, \quad (20)$$

where radial functions $F_{m=0,1}^{I,II}(r)$ are defined by expressions (11'). Calculations of the radial-angular distributions of the density of the links of the macrochain can be made on the basis of expressions (18-19).

Conclusion

Thus, as a result of MD simulation of polyampholyte polypeptides on the surface of a metal nanowire with periodic changes in time of its polarity in the transverse direction with an ultrahigh frequency, significant conformational changes of the adsorbed macromolecule are observed. In the case of MD simulation with a temperature high enough to overcome the interlink potential barriers of the macrochain adsorbed on the nanowire surface, temporary fluctuations in the polyampholyte conformations were observed. The conformational structure of the adsorbed polyampholyte polypeptide for half the period of change in the dipole moment of the nanowire changed from dense enveloping of the nanowire to the conformation in which the macromolecular fringe was extended in the transverse direction along the dipole moment of the nanowire, at those times when the dipole moment of the nanowire had the maximum absolute values.

At a comparatively low temperature of MD simulation and sufficiently low values of the nanowire dipole moment, a gradual swelling of the fringe of the adsorbed polyampholyte was observed with a displacement of most of its links to one side with respect to the plane perpendicular to the direction of the nanowire dipole moment and passing through its axis. In this case, the peaks of the angular distributions of the atoms of the adsorbed polypeptides were in this plane. At higher values of the dipole moment at a given temperature of MD simulation, such swelling of the macromolecular fringe led to desorption of polyampholyte from the nanowire surface.

Such changes in the conformational structure of polyampholyte adsorbed on the surface of the nanowire, induced by microwave electromagnetic radiation, will have a significant effect on the photochemical processes occurring in the layer of the macromolecular fringe formed by this polypeptide.

Therefore, they can be used to create and modify sensors with a conformational structure of macromolecules tunable under the influence of electromagnetic radiation, such as sensors based on the effects of surface plasmon resonance and surface-enhanced Raman scattering, as well as luminescence-optical meters for the concentration of molecular oxygen in the ground or electronically excited state.

In a number of works, including the work of the authors of [20], it was noted that plasmonic nanoparticles and nanowires significantly change the rate of spontaneous radiative transitions in electronically excited molecules located near conducting nanobodies. This circumstance allows one to consider plasmon nanoantennas as control elements in molecular luminescent sensors of chemical compounds. The mechanism for increasing the intensity of the spontaneous glow of the sensitive elements of such sensors is associated with the plasmon resonance in the nanoantenna, which is determined by the geometric parameters of the latter. In spherical nanoparticles, the oscillations of surface plasmons have been studied in sufficient detail, in contrast to extended quasi-one-dimensional conducting lines. Surface plasmon resonances in a cylinder can be determined by both local transverse oscillations of the electron density and waves traveling along the axis with different mode structures. Only further studies will make it possible to

determine which of the plasmon resonances in cylindrical bodies and shells will be more important for the formation of luminescent signals in composite, molecular-plasmonic nanostructures with axial symmetry.

Acknowledgments

This work was supported by the Ministry of Science and Higher Education of the Russian Federation within the framework of project No. FSGU-2020-0003.

REFERENCES

- 1 Li D., MaYa., Duan H., et al. Griess reaction-based paper strip for colorimetric/fluorescent/SERS triple sensing of nitrite. *Biosens Bioelectron.* 2018, Vol. 99, pp. 389 – 398.
- 2 Feng J., Xu L., Cui G., et al. Building SERS-active hetero assemblies for ultrasensitive Bisphenol A detection. *Biosens Bioelectron.* 2016, Vol. 81, pp. 138-142.
- 3 Zhao X., Dong J., Cao E., et al. Plasmon-exciton coupling by hybrids between graphene and gold nanorods vertical array for sensor. *Applied Materials Today.* 2019, Vol. 14, pp. 166-174.
- 4 Yilmaz M., Senlik E., Biskin E., et al. Combining 3-D plasmonic gold nanorod arrays with colloidal nanoparticles as a versatile concept for reliable, sensitive, and selective molecular detection by SERS. *Phys. Chem. Chem. Phys.* 2014, Vol. 16, p. 5563-5570.
- 5 Chandran G.T., Jha G., Qiao S., et al. Supercharging a MnO₂ nanowire: an amine-altered morphology retains capacity at high rates and mass loadings. *Langmuir*, 2017, Vol. 33, pp. 9324-9332.
- 6 Rong Y., Song L., Si P., et al. Macroscopic assembly of gold nanorods into superstructures with controllable orientations by anisotropic affinity interaction. *Langmuir*, 2017, Vol. 33, pp. 13867-13873.
- 7 Azman N.A., Thanh N.X., Kah J.C.Y. Sequestration of Cetyltrimethylammonium Bromide on Gold Nanorods by Human Serum Albumin Causes Its Conformation Change. *Langmuir*, 2020, Vol. 36, pp. 388-396.
- 8 Kesal D., Christau S., Krause P., et al. Uptake of pH-Sensitive Gold Nanoparticles in Strong Polyelectrolyte Brushes. *Polymers*, 2016, Vol. 8, p. 134.
- 9 Lee J., Chung K., Lee J., et al. LSPR Coupling: In Situ Studies of Surface-Plasmon-Resonance-Coupling Sensor Mediated by Stimuli-Sensitive Polymer Linker. *Adv. Funct. Mater.* 2015, Vol. 25, pp. 6716-6724.
- 10 Chen Y., Cruz-Chu E.R., Woodard J., et al. Electrically Induced Conformational Change of Peptides on Metallic Nanosurfaces. *ACS Nano*, 2012, Vol. 6, pp. 8847-8856.
- 11 Sotnikov D.V., Zherdev A.V., Dzantiev B.B. Detection of Intermolecular Interactions Based on Surface Plasmon Resonance Registration. *Biochemistry (Moscow)*, 2015, Vol. 80, pp. 1820-1832.
- 12 Zengin A., Tamer U., Caykara T. A new plasmonic device made of gold nanoparticles and temperature responsive polymer brush on a silicon substrate. *J Colloid Interface Sci.* 2015, Vol. 448, pp. 215-221.
- 13 Chen H., You T., Xu G., et al. Humidity-responsive nanocomposite of gold nanoparticles and polyacrylamide brushes grafted on Ag film: synthesis and application as plasmonic nanosensor. *Sci. China Mater.* 2018, Vol. 61, pp. 1201-1208.
- 14 Kruchinin N.Yu., Kucherenko M.G. Molecular dynamics simulation of electrically induced conformational changes of polyampholytic polypeptides on gold nanoparticle surface. *Colloid Journal*, 2019, Vol. 81, pp. 110-119.
- 15 Kruchinin N.Yu., Kucherenko M.G. Electrically induced conformational changes in gold cluster-bonded polyampholytic polypeptides on a surface of gold: molecular dynamic simulation. *Russian Journal of Physical Chemistry A*, 2020, Vol. 94, pp. 1433-1438.
- 16 Kruchinin N.Yu., Kucherenko M.G. A Molecular dynamics simulation of polyampholytic polypeptides associated with atomic clusters on the surfaces of metal-like nanoobjects. *Biophysics*, 2020, Vol. 65, pp. 186-194.
- 17 Kruchinin N.Yu., Kucherenko M.G. Molecular-dynamics simulation of rearrangements in the conformational structure of polyampholytic macromolecules on the surface of a polarized metal nanoparticle. *Colloid Journal*, 2020, Vol. 82, pp. 136-143.
- 18 Kruchinin N.Yu., Kucherenko M.G. Conformational rearrangements of polyampholytic polypeptides on metal nanoparticle surface in microwave electric field: molecular-dynamics simulation. *Colloid Journal*, 2020, Vol. 82, pp. 392-402.
- 19 Kucherenko M.G., Stepanov V. N., Kruchinin N. Yu. Inter molecular non radiative energy transfer in clusters with plasmonic nanoparticles. *Optics and Spectroscopy*, 2015, Vol. 118, pp. 103-110.
- 20 Kucherenko M.G., Stepanov V. N., Kruchinin N. Yu. Plasmon activation and luminescence quenching of solutions of polyphenylenevinylene (MEH-PPV) by single-walled and double-walled carbon nanotubes. *Optics and Spectroscopy*, 2020, Vol. 128, pp. 1298-1310.
- 21 Kucherenko M.G., Rusinov A.P., Chmereva T.M., et al. Kinetics of photoreactions in a regular porous nanostructure with cylindrical cells filled with activator-containing macromolecules. *Optics and Spectroscopy*, 2009, Vol. 107, pp. 480-485.

- 22 Kucherenko M. G., Izmodenova S.V., Kruchinin N.Yu., Chmereva T.M. Change in the kinetics of delayed annihilation fluorescence during rearrangement of polymer-chain structure in a nanocavity of a solid adsorbent. *High Energy Chemistry*, 2009, Vol. 43, pp. 592 – 598.
- 23 Phillips J.C., Braun R., Wang W., et al. Scalable molecular dynamics with NAMD. *J Comput Chem*. 2005, Vol. 26, pp. 1781-1802.
- 24 MacKerell A.D. Jr., Bashford D., Bellott M., et al. All-atom empirical potential for molecular modeling and dynamics studies of proteins. *J. Phys. Chem. B*. 1998, Vol. 102, pp. 3586-3616.
- 25 Heinz H., Vaia R.A., Farmer B.L., Naik R.R. Accurate Simulation of Surfaces and Interfaces of Face-Centered Cubic Metals Using 12–6 and 9–6 Lennard-Jones Potentials. *J. Phys. Chem. C*. 2008, Vol. 112, pp. 17281-17290.
- 26 Darden T., York D., Pedersen L. Particle mesh Ewald: An N·log(N) method for Ewald sums in large systems. *J.Chem. Phys.*1993, Vol. 98, pp. 10089-10092.
- 27 Jorgensen W.L., Chandrasekhar J., Madura J.D., et al. Comparison of simple potential functions for simulating liquid water. *J. Chem. Phys.* 1983, Vol. 79, pp. 926-935.
- 28 Novotny L., Hecht B. *Principles of nanooptics*. Cambridge: Cambridge University Press. 2006, 564p.
- 29 Kruchinin N.Yu., Kucherenko M.G. Rearrangements in the conformational structure of polypeptides on the surface of a metal nanowire in rotating electric field: molecular dynamics simulation. *Colloid Journal*, 2021, Vol. 83, pp. 79-87.
- 30 Grosberg A.Y., Khokhlov A.R., Pande V.S. *Statistical Physics of Macromolecules*. New York: AIP Press. 1994. 347p.

DOI 10.31489/2021No1/29-33

UDC 54.057+548.3+546.562:47:713-31:654:311

SYNTHESIS AND X-RAY INVESTIGATION OF NOVEL NANOSTRUCTURED COPPER-ZINC MANGANITES OF LANTHANUM AND ALKALI METALS

Kasenov B.K.¹, Kasenova Sh.B.¹, Sagintaeva Zh.I.¹, Nukhuly A., Turtubaeva M.O.²,
Bekturganov Zh.S.³, Zeinidenov A.K.³, Kuanyshbekov E.E.¹, Issabaeva M.A.²

¹Abishev Chemical-Metallurgical Institute, Karaganda, Kazakhstan

²Toraighyrov Pavlodar University, Pavlodar, Kazakhstan

³E.A. Buketov Karaganda University, Karaganda, Kazakhstan, kasenov1946@mail.ru

The aim of this work is to synthesize new nanostructured copper-zinc lanthanum and alkaline metal manganites. Polycrystalline copper-zinc manganites of lanthanum and alkali metals were synthesized by the method of ceramic technology from lanthanum (III), copper (II), zinc (II), manganese (III) oxides, and lithium, sodium, and potassium carbonates in the range of 800-1200 °C. Nanostructured particles were obtained by grinding the synthesized polycrystalline compounds at the «MM301» vibration mill of «Retsch» (Germany). By indexing X-ray images of nanostructured copper-zinc lanthanum and alkaline metal manganites, it was found that they crystallize in cubic syngony. Their lattice parameters are determined. There is a pattern in the change of the lattice parameters from the ionic radii of alkaline metals.

Keywords: copper-zinc manganite, lanthanum, alkali metals, synthesis, nanostructured particles of X-ray phase analysis.

Introduction

The development of modern branches of science and technology is impossible without directed synthesis and research of materials with a set of necessary physical and chemical properties. Currently, the object of close attention of researchers is oxide materials with semiconducting, ferroelectric, piezoelectric and pyroelectric and superconducting properties and high mixed (electronic and ionic or metallic) conductivity. These materials include rare-earth manganites of the composition $R_{1-x}M_xMnO_{3-\delta}$ (R – rare-earth elements, M – is a divalent cation). The discovery of a giant negative resistance in manganites (1993-1994) of the La (Ca, Ba) MnO₃ type with a perovskite structure was the beginning of work in the field of synthesis and research of new, previously unknown compounds formed in systems consisting of oxides of rare-earth elements, alkaline earth metals. and manganese (III).

Materials with colossal reluctance can be used as magnetic field sensors, high-density magnetic recording heads, displacement and temperature sensors. Compounds based on oxides of the transition 3d- and 4f-elements with a perovskite structure or close to it (manganites, zincates, cuprates, nickelates, cobaltites of rare-earth metals) and their solid solutions with oxides of the alkali and alkaline earth metals were widely used due to their interesting properties such as a high value of an electrical conductivity in a significant temperature range, the electronic conductivity character (semiconductor *n*- or *p*-type or metal), the magnetic and superconducting properties, etc. [1-7].

In addition, many publications of scientists from near and far abroad and also our papers on synthesis and investigation of the physicochemical properties of compounds of the above mentioned classes were summarized in our monographs [8-12]. It should also be noted that manganese-based compounds are widely applied in the ferroalloy industry [13, 14].

1. Experimental technique

In order to accumulate various unique properties of the individual compounds in a single complex, i.e. combining of cuprates, zincates and manganites as the copper-zinc manganites, the phases of composition of $LaMe_2CuZnMnO_6$ (Me^I – Li, Na, K) were synthesized. A similar work on the synthesis of lanthanum and sodium cobalt-copper manganite was published by us in [15]. To synthesize $LaMe_2CuZnMnO_6$ compounds

the source materials were oxides of lanthanum La_2O_3 (“puriss. spec.”), copper CuO , zinc ZnO , manganese Mn_2O_3 , carbonates of Li_2CO_3 , Na_2CO_3 and K_2CO_3 (“p.a.”), their stoichiometric quantities were milled well and mixed up in an agate mortar, then mixtures in the alundum crucibles were annealed in SNOL furnace at a temperature of $800\text{ }^\circ\text{C}$ for 10 h in the air. Then they were cooled to a room temperature, mixed and milled. Further they were heat-treated at $1200\text{ }^\circ\text{C}$ for 20 h. The mixtures were cooled again to a room temperature, milled and mixed. To obtain the stable equilibrium phases at low temperatures, the mixtures were annealed at $400\text{ }^\circ\text{C}$ for 10 h.

Further, to obtain the nanostructured particles of the copper-zinc manganites, their polycrystalline samples were mixed to the nanostructured particles on Retsch MM301 vibration mill (Germany) at the Karaganda Technical University. The particle sizes were determined on an electron microscope Mira 3 LMU, Tescan (Fig. 1) and an atomic-force microscope JSPM-5400 Scanning Probe Microscope “JEOL” (Japan) at the E.A. Buketov Karaganda University (Fig. 2).

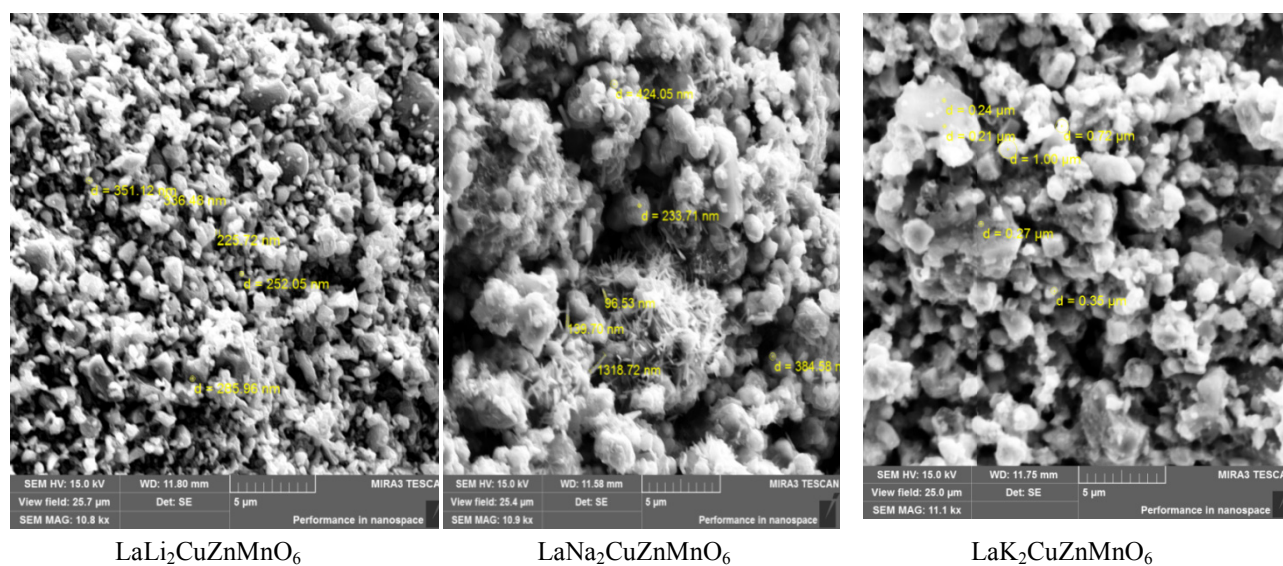


Fig. 1. SEM images

The data of Figure 1 demonstrates that $\text{LaLi}_2\text{CuZnMnO}_6$ is characterized with the particle sizes in the range of 226-285 nm, $\text{LaNa}_2\text{CuZnMnO}_6$ - 97-384 nm and $\text{LaK}_2\text{CuZnMnO}_6$ - 210-650 nm.

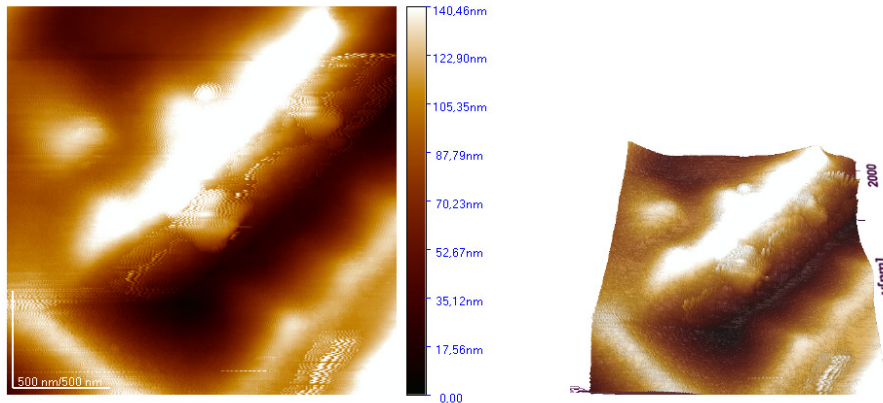
The X-ray analysis of the obtained nanostructured particles was performed on DRON-2.0. The conditions of exposure: CuK_α - radiation, $U = 30\text{ kV}$, $I = 10\text{ mA}$, a rotation speed - 100 pulses per second, time constant $\tau = 5\text{ sec}$, an angle interval -2θ from 10 to 90° . Intensity of the diffraction maxima was estimated on 100-point scale. The X-ray patterns were indicated by an analytical method [16]. Density of each compound was measured 4-5 times and the results were averaged. The procedure and calculating formula were taken from [17]. The table below shows results on assignment of indices of X-ray patterns of the nanostructured copper-zinc manganites.

2. Results and discussion

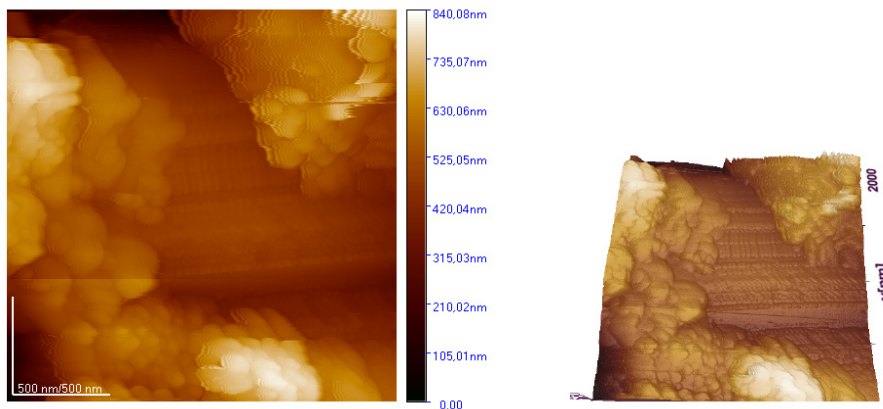
The obtained nanoscale particles of the copper-zinc manganites can be classified as the nanostructured. Referring to recommendations of the 7th International conference on nanotechnologies (Germany, Wiesbaden, 2004), the following types of nanomaterials were distinguished: the nanoporous structures, nanoparticles, nanotubes and nanofibers, nanodispersions (colloids), nanostructured surfaces and films, nanocrystals and nanoclusters. According to [18], if a nanoparticle has a complex shape and structure, then a linear size of a particle as a whole are not studied, but a size of its structural element is examined as characteristic. Such particles are generally referred to as the nanostructured particles, and their linear sizes can be significantly larger than 100 nm.

Based on the assignment of indices of X-ray patterns of the nanostructured copper-zinc manganites, it was defined that they crystallize in the cubic syngony with the following parameters of lattice: $\text{LaLi}_2\text{CuZnMnO}_6$ - $a = 13.94 \pm 0.02\text{ \AA}$, $V^0 = 2708.87 \pm 0.06\text{ \AA}^3$, $Z = 4$, $V^{\text{elec.cell}} = 677.22 \pm 0.02\text{ \AA}^3$, $\rho_{\text{roent.}} = 4.31$

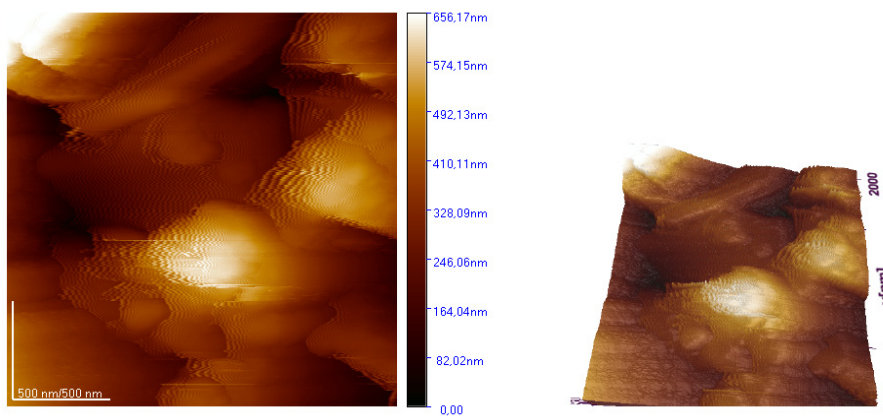
g/cm^3 ; $\rho_{pick.} = 4.28 \pm 0.02 \text{ g/cm}^3$; $\text{LaNa}_2\text{CuZnMnO}_6 - a = 14.82 \pm 0.02 \text{ \AA}$, $V^0 = 3254.95 \pm 0.06 \text{ \AA}^3$, $Z = 4$, $V^{0}_{elec.cell} = 813.74 \pm 0.02 \text{ \AA}^3$, $\rho_{roent.} = 4.13 \text{ g/cm}^3$; $\rho_{pick.} = 4.09 \pm 0.05 \text{ g/cm}^3$; $\text{LaK}_2\text{CuZnMnO}_6 - a = 15.30 \pm 0.02 \text{ \AA}$, $V^0 = 3581.58 \pm 0.07 \text{ \AA}^3$, $Z = 4$, $V^{0}_{elec.cell} = 895.39 \pm 0.02 \text{ \AA}^3$, $\rho_{roent.} = 3.91$; $\rho_{pick.} = 3.88 \pm 0.01 \text{ g/cm}^3$. The errors of the parameters "a" are determined by averaging all the diffraction lines (d, \AA) established on the X-ray images of the studied compounds, for $\text{LaLi}_2\text{CuZnMnO}_6$ out of 17 maxima of the diffraction lines, for $\text{LaNa}_2\text{CuZnMnO}_6$ out of 13, for $\text{LaK}_2\text{CuZnMnO}_6$ out of 15 d, \AA .



$\text{LaLi}_2\text{CuZnMnO}_6$



$\text{LaNa}_2\text{CuZnMnO}_6$



$\text{LaK}_2\text{CuZnMnO}_6$

Fig. 2. Atomic-force microscopic image and 3D surfaces

Table 1. Assignment of indices of X-ray patterns of the nanostructured of $\text{LaLi}_2\text{CuZnMnO}_6$ (I), $\text{LaNa}_2\text{CuZnMnO}_6$ (II) and $\text{LaK}_2\text{CuZnMnO}_6$ (III)

I/T^0	d, Å	$10^4/d^2$ (experimental)	hkl	$10^4/d^2$ (calculated)
$\text{LaLi}_2\text{CuZnMnO}_6$				
38	3.882	663.6	511	664.0
18	2.865	1218	710	1229
100	2.749	1323	721	1327
14	2.509	1588	810	1598
23	2.449	1667	420	1671
12	2.367	1785	830	1794
22	2.245	1984	900	1991
78	1.939	2660	10.2.2	2655
6	1.864	2878	10.4.1	2875
8	1.725	3361	10.6.1	3368
6	1.697	3472	11.4.2	3466
37	1.586	3975	12.3.3	3982
12	1.433	4870	14.1.1	4867
16	1.375	5289	14.3.1	5295
14	1.361	5399	13.5.5	5383
12	1.229	6620	16.3.3	6612
14	1.222	6697	16.4.0	6686
$\text{LaNa}_2\text{CuZnMnO}_6$				
14	3.902	656.8	520	657.0
100	2.757	1316	730	1314
11	2.604	1475	740	1472
10	2.525	1568	743	1562
13	2.475	1632	822	1631
11	2.321	1856	910	1857
16	2.247	1980	664	1993
35	1.945	2643	10.4.1	2650
7	1.737	3314	981	3307
34	1.572	4046	13.3.1	4054
9	1.475	4596	11.9.1	4598
17	1.374	5297	15.3.0	5300
15	1.229	6620	16.6.0	6613
$\text{LaK}_2\text{CuZnMnO}_6$				
17	3.890	660.8	440	661.0
100	2.756	1316	800	1322
15	2.600	1479	822	1487
13	2.526	1567	662	1569
16	2.364	1789	655	1776
14	2.249	1977	844	1982
50	1.945	2643	880	2643
7	1.740	3303	12.4.0	3304
8	1.624	3792	12.6.2	3800
30	1.588	3965	888	3965
7	1.459	4698	15.1.1	4688
5	1.410	5630	12.10.0	5039
17	1.375	5289	16.0.0	5286
4	1.295	5963	16.4.4	5947
13	1.229	6620	17.4.4	6629

A good fit of the experimental and calculated values of $10^4/d^2$ (Table 1), the X-ray and pycnometric densities points out the correctness and assurance of results of assignment of indices. Based on [16], the experimentally determined density refers to a real crystal and it should be slightly below than ideal. This statement also confirms that the pycnometric (experimental) densities of our obtained copper zinc manganites are relatively lower than the X-ray (ideal).

By analogy of [8, 19], the synthesized copper-zinc manganites can be assigned to the space group $Pm\bar{3}m$ of perovskite. In connection with raising the sizes of the ionic radiuses in a row of $\text{Li}^+ \rightarrow \text{Na}^+ \rightarrow \text{K}^+$, the values of «a» parameter is increased, and the values of volumes of the crystalline lattices and the elementary cells are increased in a row of $\text{LaLi}_2\text{CuZnMnO}_6 \rightarrow \text{LaNa}_2\text{CuZnMnO}_6 \rightarrow \text{LaK}_2\text{CuZnMnO}_6$.

Conclusion

The polycrystalline copper-zinc manganites of the composition of $\text{LaLiMe}^1_2\text{CuZnMnO}_6$ ($\text{Me}^1 - \text{Li, Na, K}$) were first synthesized by a method of the ceramic technology. By milling them on a vibration mill, their nanostructured particles were obtained. It was found that all obtained nanostructured copper-zinc manganites crystallize in the cubic syngony. Their lattice parameters, X-ray and pycnometric densities were determined.

It was found that with an increase in the ionic radii in the series Li and K, the lattice parameters of the studied manganites increase. The research results work make a certain contribution to the inorganic materials science, nanotechnology, radiography and crystal chemistry of nanostructured inorganic compounds and serve as the basis for further research in order to identify valuable and promising physicochemical properties of these new obtained nanomaterials.

Acknowledgments

This research was funded by the Science Committee of the Ministry of Education and Science of the Republic of Kazakhstan (Grant No. AP08855601).

REFERENCES

- 1 Tretyakov Yu.D., Brylyov O.A. New generations of inorganic functional materials. *Journal of the Russian Chemical Society named after D.I. Mendeleev*, 2000, Vol. 44, No. 4, pp. 10-16. [in Russian].
- 2 Grunberg P.A. From spin waves to giant magnetoresistance and beyond. *Physics-Uspexhi*, 2008, Vol. 178, Iss. 12, pp. 1349-1358. DOI: 10.3367/ufnr.0178.200812g.1349. [in Russian].
- 3 Erin Yu. Substance with high value of dielectric capacitivy was found. *Chemistry and Chemists*, Part 1, 2009. Available at the: http://chemistry-chemists.com/N1_2009/16-22.pdf [in Russian].
- 4 Kuznetsov M.V., Morozov Yu.G., Belousova O.V., Ortega D. Ferromagnetic nanoparticles of Zn/ZnO. *Inorganic Materials*, 2014, Vol. 50, No. 4, pp. 399-409. DOI: 10.7868/s0002337x14040101. [in Russian].
- 5 Solin N.I., Naumov S.V. Magnetic and electrical properties of weakly doped manganese-deficient $\text{La}_{1-x}\text{Ca}_x\text{Mn}_{1-z}\text{O}_3$ manganites. *Journal of Experimental and Theoretical Physics*, 2013, Vol. 116, No. 1, pp. 145-158.
- 6 Nagaev E.L. *Physics of magnetic semiconductors*. Moscow, Nauka, 1983, 220 p. [in Russian].
- 7 Perekalina T.M., Sivokon T.A., Cherkezzyan S.A. et al. Magnetic and electrical properties of $\text{La}_{1-x}\text{Sr}_x\text{MnO}_3$. *Physics of the Solid State*, 1989, Vol. 31, No. 9, pp. 87-89. [in Russian].
- 8 Kasenov B.K., Kasenova Sh.B., Sagintaeva Zh.I., et al. *Double and triple manganites, ferrites and chromites of alkali, alkaline earth and rare earth metals*. Moscow, 2017, 416 p. [in Russian].
- 9 Kasenov B.K., Kasenova, Sh.B., Sagintaeva, Zh.I., et al. *Physical properties of manganites*. Karaganda, 2017, 123 p.
- 10 Kasenov B.K., Kasenova, Sh.B., Sagintaeva Zh.I., Kuanyshbekov E.E. *New materials based on oxides of s-, d- and f-elements*. Karaganda, 2017, 117 p. [in Russian].
- 11 Ermaganbetov K.T., Chirkova L.V., Kasenov B.K. Physics of magnetic and kinetic phenomena in manganites of lanthanides. Karaganda, 2017, 251 p.
- 12 Kasenov B.K., Kasenova Sh.B., Sagintaeva Zh.I., et al. *New substituted polycrystalline and nanodimensional manganites*. Karaganda, Ecozhan, 2019, 108 p. [in Russian].
- 13 Baisanov S.O., Gabdulin G.G., Takenov T.D. About organization of production of manganese ferroalloy from Kazakhstan raw materials. *Steel*, 1997, Vol. 7, pp. 29-32. [in Russian].
- 14 Baisanov S.O., Takenov T.D., Tolymbekov M.Zh. About conditions of selective reduction in the Fe–Mn–O system]. *Bulletin of the Karaganda University. Chemistry series*, 2005, No. 4(40), pp. 65-70. [in Russian].
- 15 Kassenova Sh.B., Sagintayeva Zh.I., Kassenov B.K., Kuanyshbekov E.E., Bekturganov Zh.S., Zeinidenov A.K. Electrophysical characteristics of nanodimensional cobalte-cuprate-manganite $\text{LaNa}_2\text{CoCuMnO}_6$ and nickelite-cuprate-manganite $\text{LaNa}_2\text{NiCuMnO}_6$. *Bulletin of the Karaganda University. Physics Series*, 2020. No. 2(98), pp. 43-49.
- 16 Kovba L.M., Trunov V.K. *X-ray phase analysis*. Moscow, 1976, 256 p. [in Russian].
- 17 Kivilis S.S. *Technique of measuring of the density of liquids and solids*. Moscow, 1959, 191 p. [in Russian].
- 18 Tretyakov Yu.D. Challenges of nanotechnological development in Russia and abroad. *Herald of the Russian Academy of Sciences*, 2007, Vol. 77, No.1, pp. 15-21. DOI: 10.1134/s1019331607010030.
- 19 Vest A. *Chemistry of solid state*. Moscow, World, 1988, 588 p. [in Russian].

DOI 10.31489/2021No1/34-42

UDC 621.313.333.07:621.315.616.9

IMPROVING THE HEAT RESISTANCE OF POLYMER ELECTRICAL INSULATION SYSTEMS FOR THE MODERNIZATION OF INDUCTION MOTORS

Leonov A.¹, Usacheva T.¹, Lyapunov D.¹, Voronina N.¹, Galtseva O.², Rogachev A.³¹National Research Tomsk Polytechnic University, Tomsk, Russia, voronina@tpu.ru²Tomsk State University of Control Systems and Radioelectronics, Tomsk, Russia³Belarusian State University of Transport, Gomel, Belarus

Ensuring high power, efficiency and reliability of induction motor operation while providing small weight-size parameters represents an up-to-date problem. One of the factors limiting the reduction of weight-size parameters when increasing capacities of induction motors is the failure of the insulation system. Therefore, there is a strong need for studying the issues of slot fill when designing an induction motor, taking into account an increase in the heat resistance class of electrical insulation systems. The purpose of the present research is to develop a polymeric electrical insulation system of increased heat resistance for the modernization of an induction medium-capacity motor to reduce weight-size parameters and to evaluate the possible savings of winding material. The paper deals with an analysis on the stator-slot fill for the induction motor. Modern conductor and insulation materials were selected. The necessary calculations for a medium-power induction motor of different heat resistance classes were performed. The usage of the proposed electrical insulation system was substantiated. The analysis shows the possibility of increasing the heat resistance of the polymer electrical insulation systems to save winding material for induction motors without reducing the specified quality level.

Keywords: electrical insulation system, polymeric materials, heat resistance, induction motor, weight-size parameters.

Introduction

The problems of ensuring high capacity, economical efficiency and reliability of induction motor operation while ensuring small weight-size parameters are among the most acute problems associated with the development of modern electrical engineering [1]. The primary purpose of induction motors modernization lies in energy performance enhancement [2]. At the same time, issues of material saving have faded into the background. At present, the issues of increasing capacity and reducing the size-weight parameters of electrical devices are often solved simultaneously [3 - 6]. Among the factors limiting the reduction of weight-size parameters while increasing the induction motor capacities is the failure of the insulation system [7- 11]. In this case, under the insulation system of an induction motor we mean the stator winding and its various elements. In addition to the winding, the machine slot is filled with the case insulation, turn separator and conductor insulation as well as various insulating spacers.

During the motor operation, the currents flow through the windings causing the insulation heating leading to its aging. Thus, the insulation lifetime and, consequently, the entire electrical device lifetime are sharply reduced [12 - 14]. To ensure the reliability of the motor operation [15, 16], the motor insulation must provide the following requirements:

1) high electric strength, which prevents turn-to-turn short-circuit and winding short-circuit with metal parts of the electric motor;

2) high thermal conductivity, that increases the efficiency of heat transfer to the environment to prevent insulation overheating.

The motor weight-size parameters are largely determined by the thickness of the inter-turn and slot insulation. The thickness and design of the insulation is determined by its purpose and type, by the level of the rated voltage, and motor operating conditions [17 - 19]. On the other hand, the large insulation thickness determines the reliability of the electric motor. To increase the heat resistance of polymer electrical insulation systems we need to employ the trend of miniaturization in the production of ultra-thin enameled wires. Therefore, to reduce the weight-size parameters of an induction motor we need to investigate deeper the problem of stator slot filling using polymer insulators with a higher class of heat resistance.

1. Winding and Insulation Materials for Medium Power Induction Motors

Conventionally, the stator windings of medium-power induction motors are made of copper wires. The durability of the winding wires determine safe motor operation throughout the life cycle. The durability depends on a bunch of the wires' properties. However, the heat resistance was chosen throughout the world as the most important characteristic of electrical and insulation materials. This characteristic is directly related to a long-term permissible operating temperature [20].

Belonging to one or another class of heat resistance determines the insulation properties. The heat resistance class of enamel insulation of wires depends on the chemical composition of enamel varnish. Electrical insulating varnishes represent solutions of high molecular weight film-forming compounds or low molecular weight reactive oligomers in organic volatile liquids. When the varnish is heated in a furnace, the molecular weight of the film-forming compounds increases and the solvent evaporates. Finally, a solid enamel film forms on the wire. Some vegetable oils and synthetic resins are used as film-forming agents. Synthetic varnishes form more stable and heat-resistant enamel films on the wire.

For the production of enameled wires of heat resistance class B (130°C), F (150°C), H (180°C) manufacturers use varnishes on polyester, polyetherimide and polyamide bases. Heat resistance improvement of polymer electrical insulation systems will increase the heat resistance class of electrical devices with the same geometry of the winding wire. Consequently, this will lead to a rise in the slot fill factor of induction motors. Therefore, the power of the motors will rise, and weight–size parameters will drop significantly. These outcomes allow recommend employing the winding wire of a heat resistance class of H as a perspective way to manufacture a winding insulation system for induction motors. Thus, while improving the induction motors, the insulation thickness remains unchanged. However, the winding wires enamel will be the subject to change during fabrication. Moreover, the required heat resistance class of the windings is expected to strongly depend on the heat resistance class.

The conducted review of winding materials shows the relevance of using the copper winding wires to increase the heat resistance of polymer electrical insulation systems when developing an insulation system for medium-power induction motors with the heat resistance of class F. The cross-section the conductor wire is 1.767 mm². For the slot insulation system with heat resistance of class N, a copper winding wire with a cross-section of 1.539 mm² was chosen. Both wires are enameled with polyesterimide varnish.

Since we improve the heat resistance class of the windings, we also need to choose more heat resistant materials for the case and slot insulation. The insulation thickness is determined by the characteristics of the insulating material, such as heat resistance, dielectric strength, and others. The thickness affects to a greater extent the geometric dimensions of the slots and their filling. Limiting the size of the slot makes it necessary to design slot insulation in the form of a thin layer having high mechanical strength and corresponding to the requirements of induction motor insulation. Generally, imidoflex 292 based film-glass fiber with the thickness of 0.25 mm is used as the case insulation. Imidoflex 292 is an insulating glass wrapping, glued on both sides with a heat-resistant polyimide film. A characteristic feature of imidoflex is the resistance to high temperatures and maintaining the required level of performance with increasing in temperature. The heat resistance class of imidoflex is H. Sintoflex 82 and 828 have the same heat resistance class. Sintoflex 82 represents a film insulating material with high resistance to electrical, thermal and mechanical stress. This material is composed of a polyimide film (the most heat-resistant polymer material) and aramid paper on both sides, which possesses an original combination of characteristics. The only drawback of this material is its high cost, which is justified by the high operational characteristics of the material and long operating lifetime. The main technical characteristics of insulating materials discussed above are given in Table 1.

Table 1. Technical characteristics of insulating materials

Material grade	Thickness, mm	Surface density, [g/m ²]	Breakdown voltage, [kV], not less than	Heat resistance class, [°C]
Imidoflex 292	0.13 – 0.50	170 – 892	8	180
Syntoflex 82	0.18	191	10	180
Syntoflex 828	0.15 – 0.24	170 – 248	10	180

2. Change in Electrical Insulation System with Heat Resistance Increasing of Induction Motors

The insulation system construction is located in the stator slots of the induction motor. When designing, it is reasonable to choose the smallest slot sizes that ensure the placement of the required number of wires and their insulation. The degree of the slot volume utilization characterizes by the fill factor. The margin of the stator permissible overheating can be substantially increased by choosing the proper materials for the electrical insulation system with increased heat resistance. Reducing the insulation thickness results in an improvement in heat dissipation in the active parts of the motor. Besides, this enhances the cooling conditions. This gives grounds to reduce the geometry of the slots as well as the sizes of the motor [21]. The efficiency of using active materials, taking into account the geometry of electric motors, is determined by electromagnetic loads being the linear load A and the magnetic flux density in the air gap $B\delta$. Permissible heating of the active parts of induction motors determines the allowable levels of electromagnetic loads, since with the growth of A and $B\delta$ the losses per unit volume in the motor increase. Choosing large values of the linear load and the magnetic flux density in the air gives the best usage of active materials. This leads to sufficient material savings.

The ranges of permissible values of A and $B\delta$ are determined on the basis of experience gained during the design and operation of the induction motors of various ratings. The above mentioned values ensure that the over temperature does not exceed the allowable one for the adopted class of insulation heat resistance. Implementing electrical insulation systems with increased heat resistance demands recalculating the number of turns per motor phase, the number of effective conductors in the slot and the cross-section of the stator winding wire. The number of turns in the phase of the stator winding is determined by the following relation:

$$w = \frac{k_e U_{1n}}{4k_v k_w f \Phi} \quad (1)$$

where k_e is the ratio of the EMF of the stator winding to the rated voltage; U_{1n} is rated voltage; k_v is the field shape factor; k_w is the winding factor; f is the power supply frequency; Φ is a magnetic flux.

The number of effective conductors in the slot is calculated as follows:

$$u_c = \frac{\pi D A}{I_{1n} Z_1} \quad (2)$$

where D is the inner diameter of the stator; A is the previously accepted value of the linear load; I_{1n} is rated current of the stator winding; Z_1 is the number of stator slots.

The cross section of the stator winding wire:

$$q_{eff} = \frac{I_{1n}}{a J_1} \quad (3)$$

where I_{1n} is the rated current of the stator winding; a is the number of parallel branches of the stator winding; J_1 is the current density in the stator winding.

Updating the number of the effective conductors is performed through the Equation:

$$u'_p = \frac{u_p}{a} \quad (4)$$

where u_p is the number of effective conductors in the slot; a is the number of parallel branches of the stator winding.

The above parameter variation depends on electromagnetic loads. The total values are determined by the Equations:

$$A_{total} = \frac{2 I_{1n} w m}{\pi D} \quad (5)$$

$$B_{\delta total} = \frac{p \cdot \Phi}{D \cdot l_{\delta}} \quad (6)$$

where I_{1n} is the rated current of the stator winding; w is the number of turns in the phase of the stator winding; m is the number of phases; D is the inner diameter of the stator; p is the number of pole pairs; Φ is magnetic flux; l_{δ} is the estimated length of the magnetic circuit.

The relation to check the permissible current density is expressed by the following relation:

$$J_1 = \frac{AJ}{A_{total}}, \quad (7)$$

where AJ is the product of linear load and current density; A_{total} is the final linear load value.

Figure 1 illustrates clearly the change in the geometry of the stator slot and its filling when implementing electrical insulation systems with increased heat resistance. Changing the geometry of the slot leads to a change not only in the number of turns, the sizes of the winding wire and the values of electromagnetic loads, but also in other parameters, affecting, in turn, the parameters of the operating mode of induction motors such as power loss, efficiency η and power factor $\cos \varphi$. Therefore, the need to assess the required performance level of the improved induction motor arises. The determining factors of such an assessment are technological factors, performance indicators and allowable error band imposed on them.

As technological factors we consider the geometric sizes of the parts (e.g. slots), and requirements imposed on them in terms of accuracy in manufacturing. When designing the correctness of the proposed modernization method is evaluated by performance indicators, normalized by GOST 26772-85. For medium-power induction motors we adopted the following performance indicators, where η is efficiency, $\cos \varphi$ is power factor, M_s is starting torque ratio, I_s is starting current ratio. The performance indicators for electrical devices are given as either the accurate values or acceptable ranges of the values.

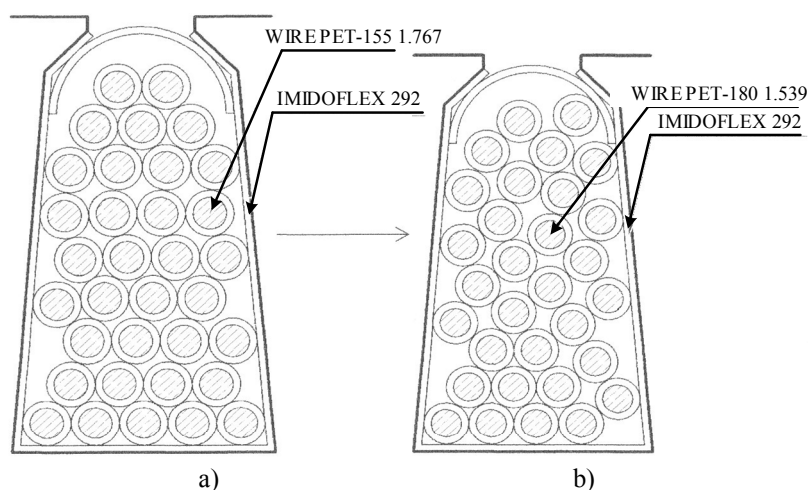


Fig.1. The change in the geometry of the stator slot and its filling for:
a) heat resistance class F; b) heat resistance class H

The characteristic feature of the electric motors lies in the presence of one-sided error bands for the performance indicators, which expands the leverage for electrical devices modernization by taking into account the accuracy of the theoretical results adjustment and determining optimal conditions for the modernization of induction motors [22]. Changing the geometry or the stator slot fill will probably lead to a change in the thermal state of the induction motor, which can cause a decrease in the nonfailure operating time. Thus, the heat fluxes, as well as the temperature changes in the internal volume of the machine and on the cooling surfaces represent the important factors that need to be evaluated. In order to verify compliance with the requirements for the permissible heating level of an induction motor, the average temperature rise of the stator winding Δ_{vav} is determined. The valid values for this parameter are given in the specification papers. The block diagram of the induction motors modernization when changing electrical insulation systems with increased heat resistance is represented in Figure 2. The basis of the given block diagram is a set of interconnected electromagnetic and thermal calculations. This allows us to assess the performance of the designed induction motor, to evaluate its possible technical characteristics, to establish the relationship between the characteristics and the weight-size parameters, and, finally, to determine the optimal values of the parameters for successful construction modernization. To render complex processes, such as the induction motor modernization, we need to establish the relationship between the information about the input of each element in the block diagram and its output. In this case the basic data (ratings, motor sizes, electrical quantities) and auxiliary data (coefficients and per unit values of the parameters) are used as initial data. At this modernization stage, changes in electromagnetic loads were chosen as independent variables. We

consider the opportunity of reducing the specific material consumption. Therefore, the block diagram should comprise the calculation of the mass and specific material consumption of the materials used to manufacture induction motors. The performance indicators and average over temperature of the stator windings represent the limitations in the block diagram (Fig. 2). The variation of the independent variables must be carried out until at least one of the limitation is not satisfied.

3. Calculation of Induction Motor Parameters when Implementing Electrical Insulation System with Improved Heat Resistance

The design of induction motors comes down to repeatedly calculating the dependencies between the performance indicators. Basically, these indicators are defined by a system of equations, empirical coefficients, graphical dependencies, which are considered as a set of equations for design. The block diagram (Fig. 2) is based on standard electromagnetic and thermal calculations. Electromagnetic calculations are used to design the manufacturing process of an induction motor, whereas thermal calculations allow to evaluate the thermal state of the machine in the course of modernization.

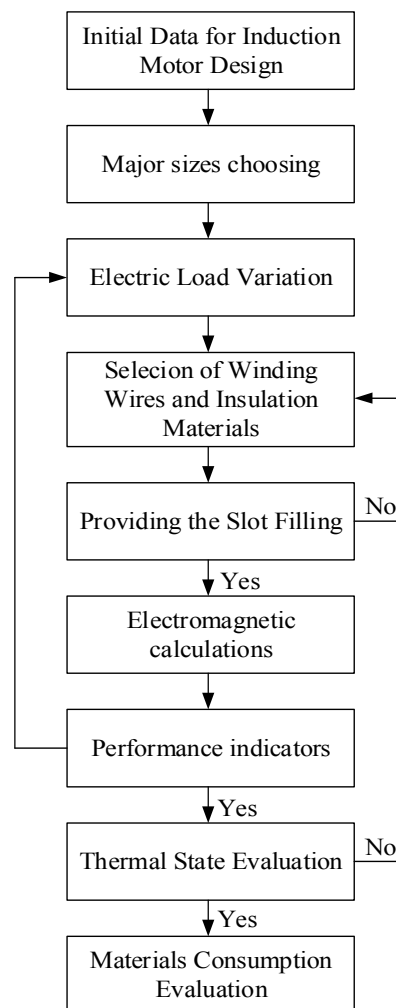


Fig.2. The block diagram of the induction motor design procedure by varying electrical insulation systems with improved heat resistance

To verify the calculations, we choose the medium-power induction motor AIR112M4 with the heat resistance class of F. The calculation results are shown in Table 2. The table presents a comparison of the calculated values for the standard induction motor with insulation system of heat resistance of class F and the improved induction motor AIR12M4 with insulation system of heat resistance of class H with decreased slot geometry. The calculated values of the main electrical quantities, performance indicators and the average

temperature rise of the stator winding are given for a comparative analysis. When solving problems of reducing the geometry of the stator slot it should be noted that usually electric motors are mass-produced. When designing a line of electrical motors, the issues of the component unification and the normalization of motor sizes are of utmost importance. Reducing the height of the axis of rotation beyond the standard values will lead to changes in the geometry of the cross section of the motor.

This will entail a change in the stamps for manufacturing and will require large capital costs for foundry, stamping, machining and other equipment [23]. When changing the height of the axis of rotation from 112 mm to the standard value of 100 mm we left the geometry of the cross section of the machine unchanged (corresponding to $h = 100$ mm). To ensure the rated power for smaller sizes of the cross section, we can only change the lengths of the stator and rotor cores. The height of the axis of rotation is the main installation parameter by which the motor is coupled to the mechanism. In our case, different external diameters of the stator core will correspond to one height of the axis of rotation. It is possible to realize the unification of the stator core for different dimensions of the induction motor by increasing the arms or developing the design of the frames with removable arms. All this is only possible within the framework of mass production, since it will entail only a retooling of the equipment and changes in equipment.

Table 2. Total calculation results for induction motor AIR112M4 when utilizing electrical insulation systems with increased heat resistance

Class	F (155 ⁰ C)	H (180 ⁰ C)
h , [mm]	112	100
P_{2H} , [W]	5500	5500
D_a , [m]	0.191	0.168
l_1 , [m]	0.125	0.155
I_1 , [A]	11.265	11.419
η	0.858	0.849
$\cos \varphi$	0.863	0.86
M_s	2.873	2.206
I_s	6.582	6.54
Δv_{av} , [°C]	68.998	92.797
Δv_{per} , [°C]	92	112

The quantitative assessment of the induction motor AIR112M4 modernization showed that the real limitation is the motor efficiency. Though, if the efficiency value takes a minimum acceptable value, the power factor value is acceptable. The average over temperature of the stator winding when decreasing the geometry parameters is below the limit value $\Delta v_{av} = 92.797^{\circ}\text{C}$. Thus, the average over temperature of the stator winding is within acceptable limits and has a significant margin. This confirms the possibility of using the proposed high-temperature-resistant electrical insulation systems for induction motors in order to reduce the material consumption for electrical devices.

4. Assessment of the Potential of Reducing Material Consumption when Using an Electrical Insulation System with Increased Heat Resistance

One of the most important areas of increasing the competitiveness of electric machines is the reduction of material consumption, which leads to a decrease in weight – size parameters. To evaluate the motor modernization conducted, it is necessary to find a variant of the designed induction motor that ensures the performance of the specified technical functions with lower weight–size parameters. The most important criterion, from the point of view of reducing the material consumption of electric machines, is materials saving: electrical steel, copper, aluminum. We consider the minimum material consumption as an optimization criterion for constructing the target function:

$$f(l_1, l_2) = (M_{st} - D_a^2 l_1 \gamma_{st}) \cdot C_{st} + (M_{Cu} - \gamma_{Cu} \cdot 2(l_1 + l_f) w_1 q_{eff}) \cdot C_{Cu} + (M_{Al} - \gamma_{Al} (Z_2 S_c l_2 + 2\pi D_r q_r)) \cdot C_{Al} \quad (8)$$

where M_{st} is the mass of steel for the stator and rotor cores in mass production; M_{Cu} is the mass of copper stator winding; M_{Al} is the mass of aluminum rotor winding in; C_{st} , C_{Cu} , C_{Al} are the costs of 1 kg of electrical steel, copper for stator winding and aluminum for rotor winding, respectively; γ_{st} , γ_{Cu} , γ_{Al} are specific masses of steel, copper and aluminum, respectively; l_f is the length of the frontal part of the winding; S_c is the cross section of the rotor slot; D_a is the outer diameter of the stator core; D_r is the average diameter of the closing rings; q_r is the cross section of the closing rings.

To assess the reduction in mass without the cost of materials, it is advisable to calculate the target functions in percent separately for each type of material:

$$\Delta M_{st} = \frac{(M_{st} - D_a^2 l_1 \gamma_{st})}{M_{st}} 100\% \quad (9)$$

$$\Delta M_{Cu} = \frac{M_{Cu} - \gamma_{Cu} \cdot 2(l_1 + l_f) w_1 q_{eff}}{M_{Cu}} 100\% \quad (10)$$

$$\Delta M_{Al} = \frac{M_{Al} - \gamma_{Al} (Z_2 S_c l_2 + 2\pi D_r q_r)}{M_{Al}} 100\% \quad (11)$$

The potential of reducing the material consumption of induction motors is determined by calculating the reduction in the material consumption of the improved induction motors expressed in percent (ΔM) and the specific material consumption of the improved induction motors (number of materials per unit power G) for each type of material, namely steel, copper, aluminum, i.e. a quantitative assessment of the reduction in the material consumption of induction motors is given:

$$\Delta M = \frac{M_B - M_I}{M_B} 100\% \quad (12)$$

$$G = \frac{M_I}{P_{2n}} \quad (13)$$

where M_B is the mass of the induction motor taken as a base, M_I is the mass of the improved induction motor.

Table 3 shows the values of the change in mass and specific material consumption of active materials for induction motor AIR112M4 with different versions of electrical insulation systems with increased heat resistance.

Table 3. Changes in mass and specific material consumption of active materials for induction motor AIR112M4 for different types of electrical insulation systems with increased heat resistance.

Insulation class	F (155 ⁰ C)	H (180 ⁰ C)
h , [mm]	112	100
M_{st} , [kg]	35.569	34.123
M_{Cu} , [kg]	1.356	1.117
M_{Al} , [kg]	1.529	1.458
G_{st} , [kg/kW]	6.467	6.204
G_{Cu} , [kg/kW]	0.247	0.203
G_{Al} , [kg/kW]	0.278	0.265

The histogram (Figure 3) presents visual representation of the change in the mass of copper for different versions of electrical insulating systems with increased heat resistance.

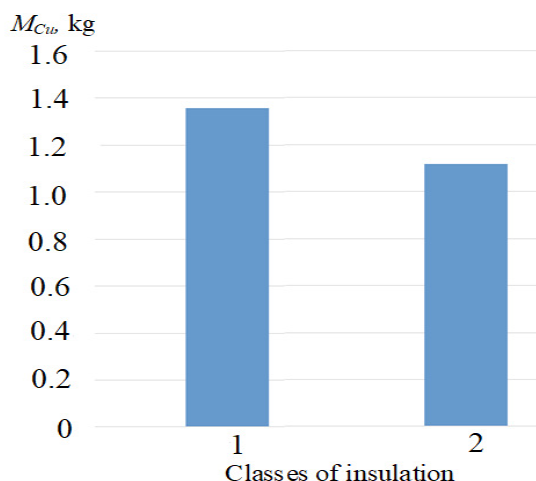


Fig.3. Change in the mass of copper in the windings of different heat resistance classes, where 1 is F; 2 is H

Undoubtedly, specific material consumption is an important indicator for comparing machines of the same power ratings and different designs. This indicator characterizes the degree of materials use for the active parts of induction motors and evaluates the manufacturability of the design.

The analysis showed a clear decrease in specific material consumption for steel, copper and aluminum. Possible savings of copper winding material equals to 17.6% with respect to the base value. It should be noted that steel savings amount to 4.1%. For aluminum this value is 4.6%. This means that with a substantial decrease in material consumption in the course of modernization, induction motors still remain heavy in mass. Thus, when applying an electrical insulation system with increased heat resistance for induction motors, the potential of reducing the weight–size parameters and saving the electrical materials used in the manufacturing process were revealed.

Conclusions

Undoubtedly, modernization of asynchronous motors by increasing the heat resistance of polymer electrical insulating systems are urgent tasks of improving electrical products, requiring the search of optimal solutions at designing and manufacturing. These studies are the part of the complex work carried out in the School of Power Engineering of Tomsk Polytechnic University. The theory of electrical machines, the theory of the foundations of electrical insulation technology, the theory of accuracy, probability and mathematical statistics were used for solving the research tasks. These studies allowed making it possible to develop calculated algorithms and recommendations for the modernization of asynchronous motors at the design and manufacture, aimed at increasing the efficiency of asynchronous motors, namely:

1. Increasing the heat resistance of polymer electrical insulation systems can be achieved through the use of materials with improved characteristics. This makes it possible to subsequently increase the value of electromagnetic loads, which leads to a better use of active materials of induction motors and reduces material consumption by reducing the slot geometry while maintaining the capacity of the induction motor.

2. As a result of increasing the heat resistance class of the insulation system while reducing the motor sizes, it is possible to save copper for winding by 17.6% with respect to the base value.

3. The analysis of the results shows good grounds for saving the winding material of induction motors without reducing the specified performance level applying an insulation system with increased heat resistance. Performing the optimal design of electric motors without taking into account standardization issues of transverse geometry leads to the savings of winding materials.

REFERENCES

- 1 Muravleva O. Resource saving prospects based on accuracy theory. *Proceeding of the Intern. Conference on Computer as a Tool. In EUROCON 2007*. 2007, 4400413, pp. 1845-1850, doi: 10.1109/EURCON.2007.4400413.
- 2 Payuk L.A., Voronina N.A., Logvinenko A.A. Modernization of electric drive of compressor station. *Bulletin of the Tomsk Polytechnic University. Geo Assets Engineering*. 2019, Vol. 330, No. 3, pp. 73 – 83. doi: 10.18799/24131830/2019/3/165.

- 3 Muravleva O., Muravlev O. Power effective induction motors for energy saving. *Proceedings of the 9th Russian-Korean Intern. Symp. on Science and Technology KORUS-2005*. 2005, Vol. 1, No. 1507731, pp. 358-362. doi: 10.1109/KORUS.2005.1507731.
- 4 Abramov B.I., Ivanov G.M., Leznov B.S. Power saving by electric drive means in the town municipal service. *Russian Electrical Engineering*. 2001, Vol. 1, pp. 6 – 11.
- 5 Han P.-W., Chun Y.-D., Choi J.-H., Kim M.-J., Koo D.-H., Lee J. The study to substitute aluminum for copper as a winding material in induction machine. *Proceedings of INTELEC*. 2009, pp. 5352008.
- 6 Payuk L. A., Voronina N. A., Galtseva O.V. Energy Characteristics of Electric Drive of Oscillatory Motion at the Shock-Free Start. *Journal of Physics: Conference Series*. 2016, Vol. 671, pp. 012044.
- 7 Guastavino F., Cordano D., Torello E., Secondo G. Electrical aging tests on different kind of insulating systems adopted for induction stator motor. *Proceedings of Conference of CEIDP*. 2015, pp. 7352068. doi: 10.1109/CEIDP.2015.7352068.
- 8 Bonnett A.H., Soukup G.C. Cause and analysis of stator and rotor failures in three-phase squirrel-cage induction motors, *IEEE Transactions on Industry Applications*. 1992, Vol. 28, No. 4, pp. 921-937, doi: 10.1109/28.148460.
- 9 Chapman M., Frost N. Insulation systems for rotating low-voltage machines. *IEEE International Symposium on Electrical Insulation*. 2008, 4570323. doi: 10.1109/ELINSL.2008.4570323.
- 10 Hwang D., Lee K., Kim Y., Lee I., Lim T., Kim D. Accessing the insulation characteristics for stator windings of low-voltage induction motors for adjustable-speed drive applications. *IEEE Industry Application Conference*. 2003, Vol. 1, pp. 432-438.
- 11 Rehder R.H., Draper R.E., Moore B.J. How Good is Your Motor Insulation System. *IEEE Electrical Insulation Magazine*. 1996, Vol. 12, No. 4, pp. 8-14, doi: 10.1109/57.526942.
- 12 Fabiani D., Montanari G.C., Contin A. Aging acceleration of insulating materials for electrical machine windings supplied by PWM in the presence and in the absence of partial discharges. *IEEE 7th Intern. Conference on Solid Dielectrics*. 2001, pp. 283-286.
- 13 Fenger M., Campbell S.R., Pedersen J. Motor winding problems caused by inverter drives. *IEEE Industry Applications Magazine*. 2003, Vol. 9, No. 4, pp. 22-31, doi: 10.1109/MIA.2003.1206913.
- 14 Frost N., Chapman M., Bruetsch R. Considerations for rotating low-voltage machine insulation designs. *IEEE Insulation*. 2008, 4570397, doi: 10.1109/ELINSL.2008.4570397.
- 15 Shevchuk V.P., Muravlev O. P. The estimation of technical state and reliability of electric machines in the process of operation. *Proceeding of MTT*. 2008, 4897500, pp. 73 – 76. doi: 10.1109/SPCMTT.2008.4897500.
- 16 Leuzzi R., Monopoli V.G., Rovere L., Cupertino F., Zanchetta P. Analysis and Detection of Electrical Aging Effects on High-Speed Motor Insulation. *IEEE Transactions on Industry Application*. 2019, pp. 1 – 8.
- 17 Grubic S., Aller J.M., Lu B., Habetler T.G. A survey on testing and monitoring methods for stator insulation systems of low-voltage induction machines focusing on turn insulation problems. *IEEE Transactions on Industrial Electronics*. 2008, Vol. 55, No. 12, pp. 4127 – 4134. doi: 10.1109/TIE.2008.2004665.
- 18 Lahoud N., Faucher J., Malec D., Maussion P. Electrical aging of the insulation of low voltage machines: model definition and test with the design of experiments. *IEEE Transactions on Industrial Electronics*. 2013, Vol. 60, No. 9, pp. 4147 – 4155. doi: 1109/TIE.2013.2245615.
- 19 Schemmel F., Bauer K., Kaufhold M. Reliability and statistical lifetime-prognosis of motor winding insulation in low-voltage power drive systems. *IEEE Electrical Insulation Magazine*. 2009, Vol. 25, No. 4, pp. 6 – 13.
- 20 Bohm F.R., Nagel K., Schindler H. A new generation of wire enamel for the production of magnet wires with outstanding corona resistance. *Electrical Insulation and Electrical Manufacturing and Coil Winding Technology Conference*. 2003, pp. 109 - 113.
- 21 Gedzurs A. Temperature protection methods of induction motor. Research for Rural Development, 21st International Scientific Conference Research for Rural Development. 2015, Vol. 1, pp. 258 – 263.
- 22 Ionel M., Stan M.-F., Virjoghe E.-O., Ionel O.-M. Algorithm for exact determination of three-phase induction machine parameters. *Proceeding of International Conference on Systems*. 2010, Vol. 1, pp. 636-643.
- 23 Boglietti A., Cavagnino A., Lazzari M., Vaschetto S. Preliminary induction motor electromagnetic sizing based on a geometrical approach. *IET Electric Power Applications*. 2012, Vol. 6, No. 9, pp. 583-592.

DEVELOPMENT OF HIGH POWER MICROFOCUS X-RAY TUBE

Trubitsyn A.A.¹, Grachev E.Yu.¹, Kozlov E.A.¹, Shugayeva T.Zh.^{2*}

¹Ryazan State Radio Engineering university, Ryazan, Russia

²K.Zhubanov Aktobe Regional University, Aktobe, Kazakhstan, assur@bk.ru

In this paper, we propose and study a new method for increasing the power of a microfocus X-ray tube of transmission type. The proposed method is based on the idea of using a heat pipe as a tube anode. A theoretical expression is obtained for the maximum power dissipated at such an anode, depending on the diameter of the electron beam and the thickness of the tungsten target. It is shown that the power of the proposed tube can be many times higher than the power of tubes with standard composite anodes. An electron-optical scheme of a tube with electrostatic focusing is proposed and analyzed.

Keywords: microfocus X-ray tube, composite anode, heat pipe, electron-optical circuit

Introduction

Currently there is a trend that a share of microfocus tubes is increasing in the market of X-ray equipment [1-4]. Microfocus x-ray tubes are tubes having about 10 μm diameter of radiation area. Advantages of microfocus sources of x-ray radiation in comparison with macrofocus ones are the following:

- high locality of the impact onto observable or processed objects;
- decrease of the radiation dose into areas being adjacent with the object;
- better quality of shadow images under the similar radiation dose;
- ability to obtain magnified x-ray images.

There are two known variants to perform anodes of microfocus tubes: reflecting and transmission types which consist of an anode body (substrate) and target, as a rule [5]. The target is most often deposited onto the anode body electrochemically. Material of the anode body (substrate) should have high heat conductivity for effective heat removal from the area of X-ray generation in the target. Besides, in the case of transmission type anodes, a substrate plays an additional role of the output window that is why most often made of metal having a high coefficient of the X-ray transmittance. Main purpose of the target is emission of x-ray quanta, so according to the Moseley law it is made of material with a high atomic number. Natural requirements of high melting temperature and low vapor tension are applied to the target.

Advantages of microfocus x-ray tubes can be maximally realized using anodes of the transmission type as opposed to anode of the reflecting type due to placing of the observable object at a short distance (fractions mm \div units mm) from the radiating surface. Main disadvantage of classical sources of the transmission type is that the upper limit of power dissipating on the planar anode is not high and does not exceed 1 W on 1 μm^2 of the electron beam cross-sectional area [1, 5]. Following increase of the power density leads to destruction of the anode material. The higher the power dissipating on the anode as well as x-ray radiation intensity is, the more qualitative and informative shadow images are. So, the researches main direction aimed at improvement of microfocus x-ray tubes of the transmission type are connected with increase of their power. Part of researches is directed at optimization of multilayer solid structures applied as an anode. Main concept of such anodes is a sequential deposition of several pairs of layers "target-substrate" [6]. Experiments have shown a practical reasonability to create multilayer structures of the "sandwich" type for dissipation of high heat powers and increase of effectiveness of the X-ray radiation generation ("fluorescence yield"), for example structures with such sequence as Ta-Cu-Ta-Cu-Ta. Another part of researches is connected with a search of nontraditional or new materials characterized by significant heat conductivity, for example, diamonds [1] used as substrates.

However, such methods cannot provide with qualitative increase of power. At present microfocus tubes with anodes of new type based on "liquid" metals have the greatest luminosity. Liquid metal anode differs because metal has been already melted and there is no reason to worry about its melting. In liquid jet sources having a record intensity of radiation diverging from a small area, a strong local heating of liquid metal is

prevented by regeneration of the material in the area of radiation due to its replacement by a fresh portion at velocity 100 m/s [7]. Main disadvantage of X-ray sources with liquid metal anodes is their technical complexity and, as a consequence, high cost. The present paper has suggested a method of qualitative increasing microfocus tube power due to usage of the so called “heat pipe” as an anode [8]. Heat pipes (HP) [9] are able to dissipate a record number of heat from small areas of local heating.

1. Development idea

Technical problem solved in the present paper is a creation of a microfocus x-ray tube with an transmission type anode which construction allows dissipating great heat powers released as a result of bombardment of the target surface by focused high-energy electrons. Design of the anode 1 of the suggested x-ray source is represented as a heat pipe which case bottom 2 faced to the cathode is a target and heated due to bombardment by accelerated and focused electrons 6 (Fig. 1).

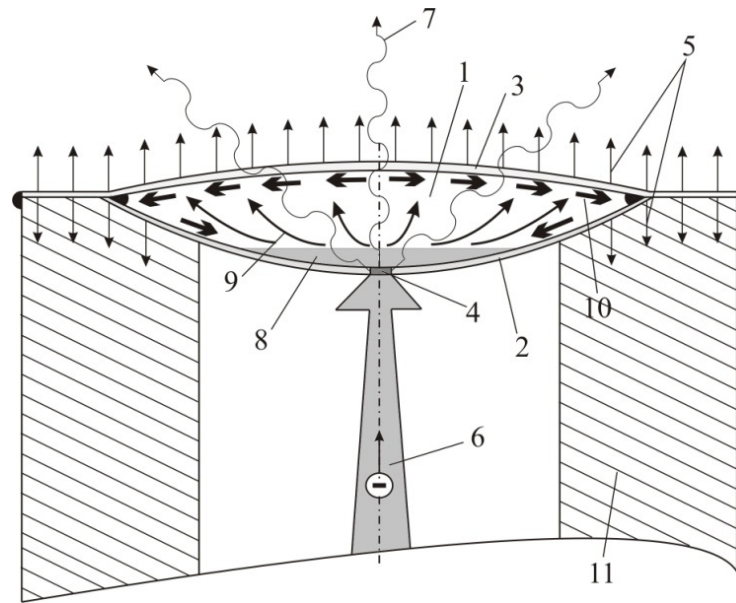


Fig.1. Anode unit of the microfocus x-ray tube executed in the form of a simple type of the HP-thermosyphon:
 1 – a heat pipe (anode), 2 – a heat pipe bottom (anode target), 3 – a heat pipe cap (anode output window), 4 – a zone of heat release (area of x-ray emission), 5 – a heat sink, 6 – a electron flow, 7 – X-ray radiation, 8 – a heat carrier, 9 – vapor, 10 – a condensate, 11 – an anode case.

Heat carrier 8 contacted with target 2 converting into vapor 9 carries energy away from the small area 4 of target heating and transfers it to another cold and forced cooling cap 3 of the heat pipe case and also a thick case of the anode 11 where a heat carrier is condensed and in a liquid phase 10 returns to the evaporation zone. Cap 3 of the heat pipe case plays an additional role of the window for bringing of x-ray radiation 7 outside. Heat pipe is an effective tool for heat removal since a molecular mechanism for transfer of kinetic and vibrational energy of the chaotic motion of single particles of the evaporator substance operates here instead of rather slow electron mechanism for heat transfer in the continuous metal thermal transmission line. Heat flow evaluated by a lot of kilowatts passes away under velocity of the liquid evaporation about several grams per second. Generated condensate returns to the evaporation zone or under influence of capillary forces provided by placement of the specialized capillary structure inside the heat pipe or, as it is shown in Fig.1, due to gravity action (the last construction is usually called as a thermo-syphon).

Thickness of the target 2 should be enough small for effective transfer of heat to the heat carrier 8 but not less than a length of the electron free path in the metal which it is made of. For effective generation of x-ray quanta, the target 2 is better to be made of metal with a high atomic number, for example tungsten. Cap 3 material should have a good heat conductivity for the effective heat sink 5 and low coefficient of the x-ray 7 decay for their effective bringing outside. Beryllium is a suitable metal for these purposes.

2. Evaluation of a value of the power dissipated by the anode "heat pipe"

The functional diagram of the heat pipe includes two elements: a target locally heated by an electron beam and a volume adjacent to the target containing a coolant and providing heat removal from it to the surrounding space. As already noted, the same "target / heat-conducting substrate" scheme underlies composite anodes. Paper [10] solved the task of the composite anode heating by an electron beam which focal spot diameter is 2δ . The anode is represented as a thick cylindrical substrate with diameter $2R$ and height h_2 made of metal with good heat conductivity k_2 (for example, Cu or Be) with a layer of refractory metal (for example, W) deposited on its base and having thickness h_1 and heat conductivity k_1 , being a target (Fig.2). Main heat exchange with external environment is performed through the anode base being opposed to the target which temperature is considered as equal to T_0 .

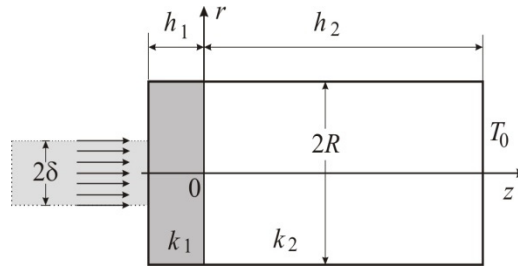


Fig.2. Diagram of the composite anode design.

For the steady-state condition a mathematical formulation of the axially symmetric task includes two steady-state heat conduction equations into cylindrical coordinates r, z in relation to the target temperature T_1 and substrate temperature T_2

$$\frac{\partial^2 T_1}{\partial r^2} + \frac{1}{r} \frac{\partial T_1}{\partial r} + \frac{\partial^2 T_1}{\partial z^2} = 0,$$

$$\frac{\partial^2 T_2}{\partial r^2} + \frac{1}{r} \frac{\partial T_2}{\partial r} + \frac{\partial^2 T_2}{\partial z^2} = 0,$$

and boundary conditions

$$\left. \frac{\partial T_1}{\partial r} \right|_{r=R} = \left. \frac{\partial T_2}{\partial r} \right|_{r=R} = 0,$$

$$-k_1 \left. \frac{\partial T_1}{\partial z} \right|_{z=-h_1} = \frac{Q}{\pi \delta^2},$$

$$T_1|_{z=0} = T_2|_{z=0},$$

$$k_1 \left. \frac{\partial T_1}{\partial z} \right|_{z=0} = k_2 \left. \frac{\partial T_2}{\partial z} \right|_{z=0},$$

$$T_2|_{z=h_2} = T_0,$$

$$-k_2 \left. \frac{\partial T_2}{\partial z} \right|_{z=h_2} = \frac{Q}{\pi R^2},$$

where, $\frac{Q}{\pi \delta^2}$ is a density of the heat flow Q in the tube focus in the case of uniform distribution of the electron beam density along the cross-section, $\frac{Q}{\pi R^2}$ is a density of the heat flow dissipating into the external environment from the butt end $z=h_2$.

Solution of the boundary-value problem in a center of the focal spot surface ($z=-h_1, r=0$) on the target surface where the temperature is maximum, has the form [10]

$$T_{max} = T_0 + \frac{P}{\pi R^2} \left(\frac{h_1}{k_1} + \frac{h_2}{k_2} \right) + \frac{P}{\delta k_1} \sum_{n=1}^{\infty} L_n \frac{J_1 \left(\mu_n \frac{\delta}{R} \right)}{\mu_n}, \quad (1)$$

where $L_n = \frac{\frac{k_1}{k_2} \operatorname{th} \left(\mu_n \frac{h_2}{R} \right) + \operatorname{th} \left(\mu_n \frac{h_1}{R} \right)}{\frac{k_1}{k_2} \operatorname{th} \left(\mu_n \frac{h_1}{R} \right) \operatorname{th} \left(\mu_n \frac{h_2}{R} \right) + 1}$, $J_1(x)$ is a first-order Bessel function of the first kind, μ_n are roots of the function $J_1(x)=0$, $n=1, 2, 3 \dots$ is a serial number of the root, P is power of the electron flow on the anode surface.

Formula (not mentioned here) for temperature in the point $z=0$, $r=0$ has the same form at the border of the target and substrate partition. Calculations for the composite anode have shown that overheating of the target depends on its thickness. Overheating is considered as exceeding T_{max} of the permissible temperature T_{adm} . So, for tungsten $T_{adm}=1600$ °C [10]. Under thick layer of the target its surface can be heated up to the limiting values, while the heat-conducting substrate has a low temperature. Under decreasing of the target thickness, the substrate will be heated more and more and ultimate power of the electron beam will be determined by the permissible temperature T_{adm} of its heating. For copper $T_{adm}=750$ °C [10]. It is obvious that there is an optimal target thickness when useful peculiarities of the target (high temperature of melting) and substrate (high heat conductivity) will be used. In the present paper evaluation of the power dissipated by the anode performed in the form of a heat pipe is executed in approximation of the equivalent heat conductivity. Concept "equivalent heat conductivity" is often used for determination of heat pipe efficiency [9]. For example, classical cylindrical pipes with water under temperature 150°C as a heat carrier have heat conductivity in hundred times more than copper. Heat pipes can be created for operation in the temperature range from 4 to 2300 K by the appropriate choice of the coolant and the housing material. For operation in the temperature ranges greater than 750 K and comparable to the melting temperatures of structural metals in vacuum electronics devices, high-temperature heat pipes are used. High temperature heat pipes are often called heat superconductors. Indeed, pipes with liquid metal coolants, for example, sodium, are capable of providing effective thermal conductivity thousands and even tens of thousands of times more than the best heat conductors: silver and copper [9].

A metal with a high atomic number, for example, tungsten, can be used as the target material for the heat pipe anode. The thermal conductivity of tungsten is 0.98 W / (cm K). Since the thermal conductivity of the substrate, the role of which in our case is played by the volume of the heat pipe, is tens of thousands of times higher than the thermal conductivity of tungsten, then setting $k_2 \gg k_1$ in formula (1) we obtain the following expression for evaluation of the maximum temperature of the anode consisting of a target with heat conductivity k_1 and substrate having a significant heat conductivity k_2 :

$$T_{max} = T_0 + \frac{P}{k_1} \left[\frac{h_1}{\pi R^2} + \frac{1}{\delta} \sum_{n=1}^{\infty} M_n \frac{J_1 \left(\mu_n \frac{\delta}{R} \right)}{\mu_n} \right], \quad (2)$$

where $M_n = \operatorname{th} \left(\mu_n \frac{h_1}{R} \right)$.

Correctness of the obtained expression (2) is confirmed by practical coincidence of calculation results (absolute calculation error does not exceed 0.0001 K) performed according to equations (1) and (2), firstly, for thick targets ($h_1 > 1$ mm), when the influence of the thermal conductivity of the substrate is insignificant; secondly, for thin targets ($1 \mu\text{m} < h_1 < 1$ mm) and substrates of real thickness with a high thermal conductivity $k_2 > 10000$ W / (cm K). All of the above allows us to consider formula (2) as an adequate estimate of the maximum heating temperature of the target of the "heat pipe" anode.

Let's mention again that T_{max} cannot exceed T_{adm} of the target material. i.e. condition $T_{max} \leq T_{adm}$ should be fulfilled. Designating $\Delta T = T_{adm} - T_0$ we obtain a formula for evaluation of the maximally permissible power absorbed by the target of the anode "heat pipe"

$$P_{max} = \frac{k_1 \Delta T}{\frac{h_1}{\pi R^2} + \frac{1}{\delta} \sum_{n=1}^{\infty} M_n \frac{J_1 \left(\mu_n \frac{\delta}{R} \right)}{\mu_n}}. \quad (3)$$

Power in formula (3) has a dimension [Watts], and distances and radiuses are measured in [cm].

In table 1 results of calculations of the permissible power dissipating on the tungsten target of the anode “heat pipe” (W-HP) according to expression (3) under various values of thickness h_1 of the target and diameter 2δ of the focal spot of a beam of electrons are shown in columns 3÷8. Target parameters are $k_1=0.98\text{W/cm}\cdot\text{K}$, $\Delta T=1500\text{ K}$, $2R=0.8\text{ cm}$.

Table 1 - Ultimate power dissipating by the W target of the anode “heat pipe”.

2δ	Thin layer W (W-Be)	h_1 (W-HP)					
		3 mm	1 mm	100 μm	10 μm	1 μm	100 nm
1	2	3	4	5	6	7	8
2 μm	0.4 W	0.46 W	0.461 W	0.464 W	0.48 W	0.68 W	4.64 W
10 μm	2.2 W	2.31 W	2.313 W	2.35 W	2.78 W	11.56 W	115.77 W
30 μm	6.7 W	6.94 W	6.97 W	7.31 W	12.51 W	103.9 W	1.04 kW
100 μm	22.3 W	23.22 W	23.52 W	27.82 W	115.6 W	1.16 kW	11.6 kW
200 μm	44.6 W	46.69 W	47.91 W	68.12 W	462 W	4.62 kW	46.2 kW

Paper [11] constructed a simulation model for heating of the composite anode of transmission type. The anode is considered as a homogeneous disk made of material of the substrate. It is explained by the fact that thickness of the target is small (several μm), temperature drop is insignificant, so target temperature can be considered as equal to the substrate surface temperature. Column 2 of the table 1 shows results of evaluation of the ultimate power dissipated by such anode (thin W target on thick Be substrate) for comparison. According to results of calculations (see table 1) dependencies of the ultimate dissipating power on thickness of the target of the anode “heat pipe” under two values of the focal spot diameter are shown in Fig.3. To visually assess the advantages of such an anode design the dotted lines (a) and (c) show levels of maximum powers which a standard composite W-Be anode of the transmission type can dissipate according to evaluations [11].

Let's analyze data from Table 1 and Fig.3. Under great thicknesses ($h_1 > 1\text{ mm}$) of the W target of the anode “heat pipe”, a value of the dissipated power is determined by heat resistance of tungsten and heat pipe does not ensure heat removal from the heating zone. So, in this case ultimate heat power only insignificantly exceeds the power dissipated by the standard composite W-Be anode described in [11]. Tangible benefit in the dissipating power is reached only under very small ($h_1 < 100\ \mu\text{m}$) thickness of the target of the anode “heat pipe”, since in this case the thermal resistance of the target becomes insignificant and the thermal power begins to be actively dissipated by the working volume of the heat pipe.

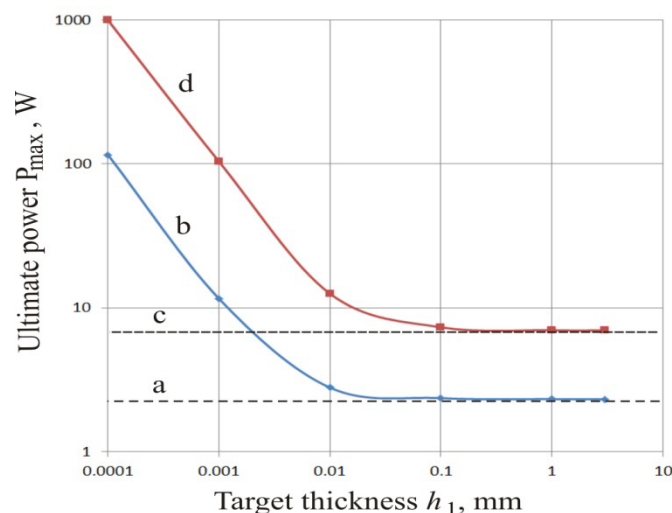


Fig.3. Ultimate power dissipating by the W target of the anode “heat pipe”: b - $2\delta=10\ \mu\text{m}$, d - $2\delta=30\ \mu\text{m}$. Levels of the ultimate power [11] dissipated by a standard composite W-Be anode of the transmission type: a - $2\delta=10\ \mu\text{m}$, c - $2\delta=30\ \mu\text{m}$.

It is obvious that application of material with such small thickness is technologically complicated, i.e. the scientific problem becomes the technological problem. But it has a solution. In particular, melting of the

“thick” layer of tungsten by an electron beam with the specified power under the first switching of a microfocus tube provides a required thickness of the material in the area of focus. Additionally, we note that calculations according to formula (3) have shown a slight growth of P_{max} under increase of the anode diameter $2R$ up to several centimeters, i.e. the anode diameter is not a critical parameter. Thus, in the case of usage of a heat pipe as an anode there is no optimal thickness of the target, the thinner the target is, the greater power can be dissipated from the heating area. It is main advantage of usage of the heat pipe as an anode of the microfocus x-ray tube.

3. Tools for simulation of the electron-optical scheme of the microfocus tube

At the end of the theoretical stage of the development of a high-power microfocus tube its electron optical scheme is simulated. Numerical methods have the most accurate evaluations regarding forecasting parameters of devices of electron optics with the complicated electrode configuration. Numerical simulation of the electron-optical systems (EOS) traditionally includes three independent sections calculation of:

- electrostatic and magnetic fields in operating volume;
- charges particles trajectories in the system electromagnetic field;
- EOS integrated characteristics such as angular focusing of the specified order, dispersion, resolving power, aberration distortions, etc.

For effective solution of problems of numerical simulation of electron-optical systems in the framework of the present paper the home made software CAE «FOCUS» [12 - 14] has been used. It is a combination of several software modules: *Design*, *Field_E*, *Field_M*, *Path_S*, *Path_D*, each of which solves an independent task:

- module *Design* is intended for formation and modification of the EOS construction,
- module *Field_E* realized a method of boundary elements for calculation of the EOS potential distribution function,
- module *Field_M* ensures a calculation of the distribution function of the magnetic field induction of a set of solenoids by the method developed by authors and called as the Current Elements Method,
- module *Path_S* is intended for the trajectory express-analysis of static EOS,
- module *Path_D* suggests a more powerful set of user functions and analytical possibilities under execution of the three-dimensional trajectory analysis of systems with variable electric and constant magnetic fields.

4. Development of the x-ray tube electron-optical scheme

Electron-optical scheme of the tube should ensure acceleration of the electron flow and its focusing on the anode surface. Classical scheme of the low-voltage emission system construction used in electron guns of spectrometers, electron microscopes and others is represented as a sequence of the cathode lens and several single lenses, besides the first electrode of each single lens is an inter mediate accelerating anode where a hole diaphragm is performed. This diaphragm ensures an electron transit and decreases an angular spread of the electron beam in order to set a required focus sharpness at the output.

Microfocus tube cannot be constructed according to the classical scheme because of several reasons. Firstly, due to high voltages applied to electrodes of the tube, placement of focusing lenses between the cathode and anode (anti-cathode) taking into consideration requirements for electric strength of the constructions will lead to a sharp increase of its dimensions along the axis z . Secondly, restriction of the angular spread of the already accelerated electron beam by means of intermediate diaphragms will cause a spurious emission of X-rays from walls of these diaphragms. That is why we suggest such electron-optical scheme when after the primary formation of the electron beam, its focusing begins immediately, i.e. space of acceleration and focusing becomes combined. Moreover, the tube operates in the mode without restrictions of the cathode emission current. Besides, effective cathodes with indirect heating, for example impregnated ones, are better to be used as a cathode for provision with high power on the anode. Emitting surface of such cathodes is more often represented as a planar circle with large diameter. CAE “FOCUS” has allowed developing an electron-optical scheme of the x-ray tube under conditions of high reliability of results.

Results of the trajectory analysis of the microfocus tube are shown in Fig.4. Trajectory analysis has been performed not taking into account influence of the space charge, since level of current in the tube does not exceed several mA. The tube operates in the following way. Electrons 1 emitting from the base of the cylindrical thermal emissivity cathode 2 arrive to the accelerating electric field between the cathode 2 with a

potential V_c and the anode 3 having a positive potential V_a . Hereinafter, all potentials are considered in relation to the potential of cathode V_c . Electron flow 1 forms an image with diameter 2δ on the anode 3 target. Formation of the image is performed by the electric field created by a small negative potential V_w on the Wehnelt electrode 4 and also positive potential V_f on the focusing electrode 5 and accelerating potential V_a on the anode 3. Area of interaction of accelerated electrons 1 with material of the anode 3 target becomes a source of emission of x-rays 6. Tube electrodes are located in the ceramic case 7.

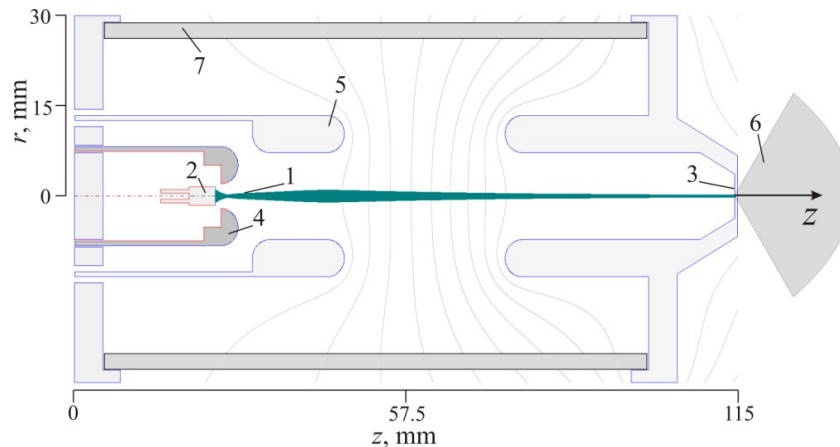


Fig. 4. Electron-optical scheme of the axially symmetrical microfocus tube: results of the trajectory analysis.

Wehnelt electrode serves for the primary formation of the electron flow and adjustment of dimensions of the effective area of electron emission from the cathode due to change of the potential V_w , value because diameter d_0 of the zero-equipotential close to the cathode surface (Fig. 5) depends on a value of this potential. Zero equipotential divides a cathode area into two sub-areas: I and II. Electrons emitted by the cathode (including its lateral surface) higher than the zero equipotential (sub-area I) return to the cathode; electrons emitted lower than the zero equipotential (sub-area II) become a part of the flow moving to the anode. This effect is a result of action of the electrostatic force F_e which directions are shown in Fig.5 in corresponding sub-areas.

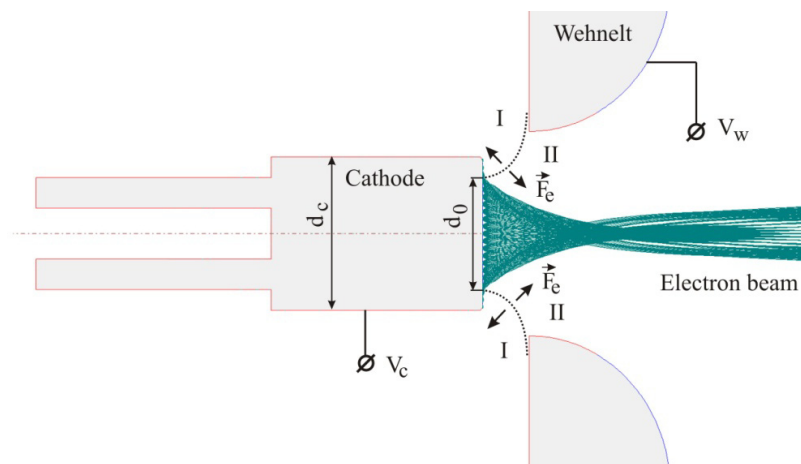


Fig.5. Formation of the electron beam in the cathode area. Pointed line is a zero equipotential.

Fig. 6 shows a dependence in relation to diameter d_0/d_c of the zero equipotential on a value of the potential V_w of the Wehnelt electrode, where d_c is a cathode diameter. Dependence shows a possibility of significant decrease of the emission area diameter by increasing of an absolute value of the negative potential V_w . Let's note that for positioning of the smallest cross-section (focus) of the electron flow on the anode target surface, a corresponding adjustment of the potential V_f of the focusing electrode (fig. 6, curve V_f) is required. Unfortunately, decrease of the emission area does not lead to decrease of the focal spot diameter 2δ (fig. 6, curve $2\delta/d_c$). It is connected with presence of angular aberrations of the researched EOS. Following stage of current researches suggests a development and optimization of the anode "heat pipe" construction,

minimization of the electron flow focal spot diameter due to optimization of the electron-optical scheme of the microfocus tube, production of the experimental sample and performance of experimental researches.

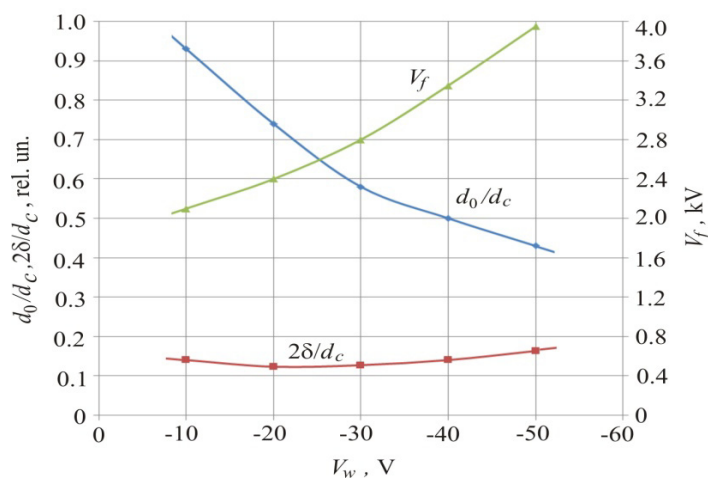


Fig.6. Dependencies of geometrical and electrical parameters of the microfocus tube on the Wehnelt electrode potential. Anode potential is $V_a=80$ kV.

Conclusion

The present paper has suggested an idea to increase power of the microfocus x-ray tube due to usage of the heat pipe as an anode. Values of the limiting power dissipated on the anode have been evaluated depending on a diameter of the electron flow focal spot. The power of the tube with the anode of the heat pipe can be tens and hundreds of times higher than the power of standard tubes with composite anodes of the transmission type. Electron-optical scheme of the microfocus tube has been developed, which provides acceleration of the electron flow and its transportation from the emission region to the focal point with a 10-fold compression of the section radius.

Acknowledgments

The research has been carried out at expenses of the Russian Science Foundation grant. Project No 18-79-10168.

REFERENCES

- 1 X-ray W or X Microfocus Tubes. Available at: www.x-ray-worx.com/x-ray-worx/index.php/en/microfocus-x-ray-tubes-overview (Jan13, 2020).
- 2 X-ray Hamamatsu Microfocus Tubes. Available at: www.hamamatsu.com/eu/en/community/xndt/x-ray_sources.html (Jan13, 2020).
- 3 X-ray Comet Microfocus Tubes. Available at: www.globalspec.com/industrial-directory/x-ray_tube_comet (Jan13, 2020).
- 4 X-ray Oxford-Instruments Microfocus Tubes. Available at: www.oxford-instruments.com/products/x-ray-tubes-and-integrated-sources/microfocus-x-ray-systems (Jan13, 2020).
- 5 Ivanov S.A., Schukin G.A. *X-ray tubes for engineering*. Leningrad, 1989, 200p. [in Russian]
- 6 Korenev S. *Target from Production of X-rays*. USA Patent: US 6,463,123, 2002.
- 7 Hemberg O., Otendal M., Hertz H. M. Liquid-metal-jet anode electron-impact x-ray source. *Applied Physics Letters*. 2003, Vol. 83, No. 7, pp. 1483-1485.
- 8 Trubitsyn A.A. *Microfocus transmission X-ray tube with high level of dissipated power*. Russian Patent No. 2653508, 2018, 9 p.
- 9 Dunn D., Reay D.A. *Heat pipes*. Oxford, New York: Pergamon Press, 1976, 299 p.
- 10 Haradzha F. N. *Common X-ray engineering course*. Leningrad, 1966, 568 p. [in Russian]
- 11 Podymskiy A.A. *Power X-ray tubes to X-ray imaging*. PhD Thesis, S-Petersburg, 2016, 148 p. [in Russian]
- 12 Gurov V., Saulebekov A., Trubitsyn A. *Analytical, Approximate-Analytical and Numerical Methods in the Design of Energy Analyzers*. In Advances in Imaging and Electron Physics. Hawkes P.W. (Ed.). 2015, London: Academic Press. Vol. 192, 209 p.
- 13 Trubitsyn A., Grachev E., Gurov V., Bochkov I., Bochkov V. *CAE «FOCUS» for Modelling and Simulating Electron Optics Systems: Development and Application. Proceedings of SPIE*. 2017, Vol. 10250, p.10250V-1.
- 14 Software CAE FOCUS: Available at: www.focuspro-soft.com.

DOI 10.31489/2021No1/51-56

UDC 533.682; 533.6.01; 621.548

NUMERICAL SIMULATION OF THE FLOW AROUND A WIND WHEEL WITH ROTATING CYLINDRICAL BLADES

Tanasheva N.K.¹, Bakhtybekova A.R.^{1*}, Sakipova S.E.¹, Minkov L.L.²,
Shuyushbaeva N.N.³, Kasimov A.R.³

¹E.A. Buketov Karaganda University, Karaganda, Kazakhstan, asem.alibekova@inbox.ru

²National Research Tomsk State University, Tomsk, Russia

³Sh.Ualikhanov Kokshetau State University, Kokshetau, Kazakhstan

The article discusses the results of numerical simulation of the flow around a wind wheel with blades in the form of rotating cylinders using the software package ANSYS. The advantage of a wind turbine with rotating cylindrical blades in comparison with traditional blade installations is the starting moment and the beginning of energy production at a wind speed of (2 - 3) m/s. A mathematical model has been developed based on three-dimensional Navier-Stokes equations in a rotating system. The corresponding boundary conditions are formulated. A calculated pattern of the flow around the wind wheel with rotating cylindrical blade is obtained. There are shown regions of the velocity field with turbulent vortices, which are formed at high Reynolds numbers. The degree of influence of the angular speed of rotation of the wind wheel on the magnitude of the moment of forces at various speeds of the incoming air flow has been determined.

Keywords: wind wheel, ANSYS, rotating cylinder, mathematical model, moment of forces.

Introduction

Experimental research of a wind power plant is a rather time-consuming process, and requires certain climatic conditions with wind components. In such cases, it is advisable to use a theoretical study using mathematical modeling [1]. A wind power plant with rotating cylinders is distinguished by the Magnus effect involved in its operation from existing blade wind turbines. The Magnus force that occurs on a rotating cylinder due to the asymmetry separation of the flow from its surface can be an order of magnitude higher than the lifting force of the traditional blade. Based on this, in the case of the installation under consideration, we can expect an increase in the driving force of the wind wheel, as well as other operational advantages. One of the main advantages of a wind power plant with cylindrical blades is the start of energy generation at low wind speeds starting from 2 m/s, in contrast to the blades with 5 m/s [2].

In the modern scientific world, numerical and theoretical studies of the aerodynamic characteristics of a mathematical model of a wind power plant with a rotating cylinder reach a qualitative level using the Navier-Stokes equations. This type of research is necessary to optimize the model configuration parameter [3, 4]. It should be noted that there are some difficulties in solving problems of the dynamics of continuous media, with the modeling of media due to the small values of the Mach number ($M < 0.1$) [5-8]. To solve this problem, the ANSYS program was chosen as a CFD solver tool for the simulation procedure, since it provides flexible and accurate capabilities when working with non-stationary flow conditions, and also offers a wide range of turbulence models. In three-dimensional (3D) modeling, you can set real operating boundary conditions and measure the values of interest at any given location [9-13].

1. The mathematical model of a wind wheel

1.1. System of equations

In the simulation of rotation, the three-dimensional Navier-Stokes equations in a rotating frame of reference have the form:

continuity equations (conservation of mass)

$$\frac{\partial \rho}{\partial t} + \nabla \cdot \rho \vec{v}_r = 0, \quad (1)$$

conservation of momentum equation

$$\nabla \cdot (\rho \vec{v}_r \cdot \vec{v}_r) + \rho (2\vec{\omega} \times \vec{v}_r + \vec{\omega} \times \vec{\omega} \times \vec{r}) = -\nabla p + \nabla \vec{\tau}_r, \quad (2)$$

where ρ – air density; \vec{v}_r – relative speed; $\vec{\omega}$ – angular velocity; $\vec{\omega} \times \vec{v}_r$ – coriolis acceleration; $\vec{\omega} \times \vec{\omega} \times \vec{r}$ – centripetal acceleration; $\vec{\tau}_r$ – viscous stress, p – pressure.

Since the simulation of a rotating wind wheel involves non-stationary aerodynamic effects, choosing the right turbulence model is of great importance. The realizable k- ε turbulence model was used to model the currents around the rotating wind wheel. This model is used to model single-phase flows at high Reynolds numbers. The physical interface is suitable for incompressible flows, weakly compressible flows, and compressible flows at low M (Mach number), usually M less than 0.3).

The main assumptions made when describing the flow of air flowing around a wind power plant:

1. Due to the low values of M, when the ratio of the gas velocity to the local speed of sound $M \ll 0.1$, the motion of the air flow is described by the equations valid for an incompressible medium.

2. Due to the large Re (the ratio of the inertial forces to the viscosity forces, $Re > 10^4$), the flow is turbulent.

3. Due to the low values of M and slight temperature changes in the vicinity of the wind wheel, the flow is isothermal.

The equations implemented at the k- ε interface for solving turbulent flow problems include the Navier-Stokes equations (RANS) averaged by Reynolds for momentum conservation and the continuity equation for mass conservation (3). The flow near the walls is modeled using wall functions f_i .

$$\rho \bar{u}_j \frac{\partial \bar{u}_i}{\partial x_j} = \rho \bar{f}_i + \frac{\partial}{\partial x_j} \left[-\bar{\rho} \delta_{ij} + \mu \left(\frac{\partial \bar{u}_i}{\partial x_j} + \frac{\partial \bar{u}_j}{\partial x_i} \right) - \rho \overline{u'_i u'_j} \right], \quad (3)$$

where $\rho \bar{f}_i$ – external forces; $-\bar{\rho} \delta_{ij}$ – pressure forces; $\mu \left(\frac{\partial \bar{u}_i}{\partial x_j} + \frac{\partial \bar{u}_j}{\partial x_i} \right)$ – viscous forces; $\rho \overline{u'_i u'_j}$ – Reynolds stresses.

The left-hand side of this equation is the change in the average momentum of the liquid element due to the instability of the average flow and the convection of the average flow. This change is balanced by the averaged external forces, pressure forces, viscous forces, and apparent stress $-\rho \overline{u'_i u'_j}$ due to the fluctuating velocity field, commonly referred to as the Reynolds stress. Equations (4 - 6) are an implementation of the k- ε turbulence model:

$$\frac{\partial}{\partial t} (\rho k) + \frac{\partial}{\partial x_i} (\rho k u_i) - \frac{\partial}{\partial x_j} \left[\left(\mu + \frac{\mu_t}{\sigma_k} \right) \frac{\partial k}{\partial x_j} \right] = G_k - \rho \varepsilon, \quad (4)$$

$$\frac{\partial \rho \varepsilon}{\partial t} + \frac{\partial \rho \varepsilon u_j}{\partial x_j} = \frac{\partial}{\partial x_j} \left[\left(\mu + \frac{\mu_t}{\sigma_\varepsilon} \right) \frac{\partial \varepsilon}{\partial x_j} \right] + \rho \varepsilon \left(C_1 S - C_2 \frac{\varepsilon}{k + \sqrt{v \varepsilon}} \right), \quad (5)$$

$$\mu_t = \rho C_\mu \frac{k^2}{\varepsilon}, \quad (6)$$

where G_k – the turbulence kinetic energy of due to the average velocity gradients; k – is the turbulent kinetic energy; ε – turbulent dissipation; μ_t – eddy viscosity; σ_k , σ_ε , C_1 , C_2 – model constants ($\sigma_k = 1.0$, $\sigma_\varepsilon = 1.2$, $C_1 = 1.44$, $C_2 = 1.9$); $S = \sqrt{2 S_{ij} S_{ij}}$ – is the modulus of the strain rate tensor; C_μ – dimensionless empirical constant.

1.2 Boundary conditions and computational model

To increase the computational efficiency, it was decided to use the symmetric and rotational nature of the wind turbine operation [9, 10]. Figure 1 shows the computational domain and the built - in grid with boundary conditions. The boundary conditions are presented in Table 1.

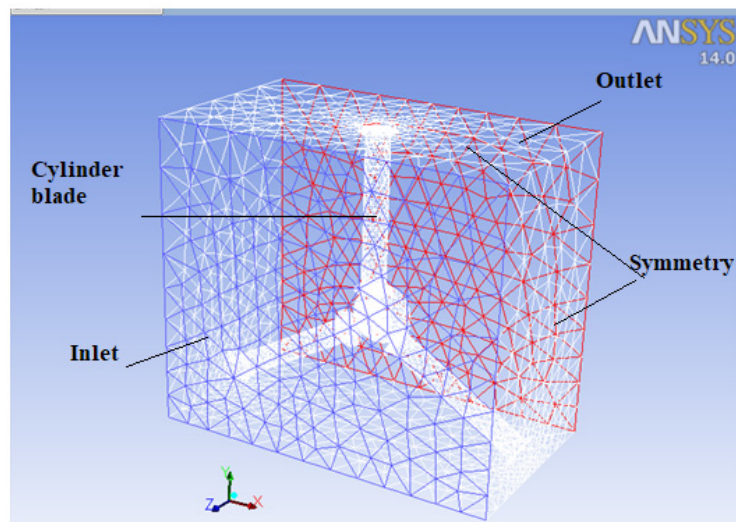


Fig.1. Computing area of the wind wheel

Table 1–List of boundary conditions

Boundary conditions	
Inlet	
Type	Inlet speed
Initial pressure gauge (Pa)	0
Air flow velocity, m / s	3, 5, 7, 10, 15
Turbulence intensity (%)	5
Coefficient of turbulent viscosity	10
Outlet	
Type	Outlet pressure
Pressure gauge (Pa)	0
Reverse flow of turbulent intensity (%)	5
Coefficient of backflow of turbulent intensity (%)	10
Blade surface	
Type	Wall
Shift condition	Nosliping
Periodic conditions	
Type	Rotation
Wind wheel rotation speed (rpm)	300, 500, 700

2. Discussion of numerical simulation results

As a result of numerical simulation, a picture of the air flow around the wind wheel was obtained (Figure 2). As can be seen from the figure, a three-dimensional vortex characteristic of a turbulent flow at high Reynolds numbers is observed in the rear part. This phenomenon is characterized by the constant distribution's formation of air flow characteristics's inconsistent pulsations in wavelength range from the minimum determined by the viscosity forces to the maximum determined by the flow conditions at the boundary. Studying the methods of numerical study of wind power plants, it was found that the result of modeling should be the dependences of mechanical parameters, namely:

- 1) The functional dependence of mechanical power on air flow parameters and speed:

$$P_m = f(v, n_1),$$

where P_m – mechanical output power; v – air flow rate; n_l – the number of revolutions of the wind wheel.

2) The directly proportional dependence of the mechanical moment on the mechanical power:

$$M_m = \frac{P_m}{\omega}$$

where M_m – mechanical moment; ω – the angular speed of rotation of the propeller.

3) The equation describing the motion of the wind wheel:

$$J \cdot \frac{dw}{dt} = M_m - M_g$$

where J – wind wheel moment of inertia; M_g – useful moment load on the shaft [1, 6].

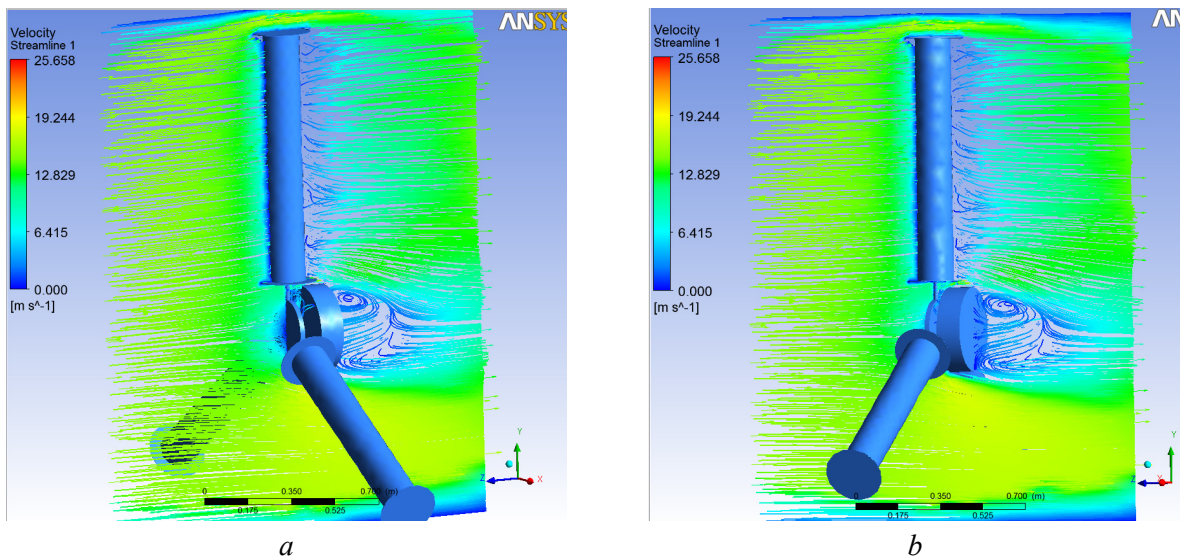


Fig.2. Pictures of the flow around the wind wheel velocity field at $v = 15$ m/s: a) front view; b) rear view.

The above dependencies show the complete dynamic picture of the wind wheel. Figure 3 shows influence diagram of the equivalent concentrated forces Q_v , Q_w and the force F_g , which forms the moment of the payload on the propeller shaft.

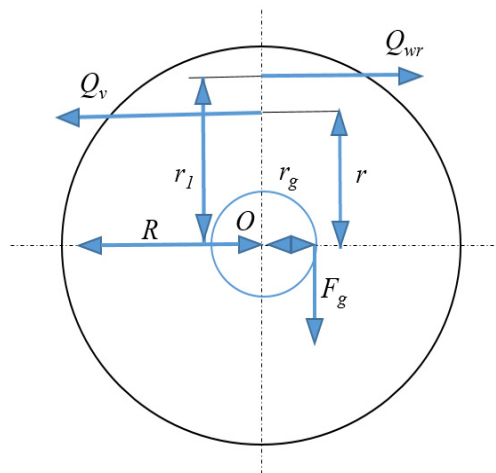


Fig.3. Scheme of action of the resulting equivalent forces on the wind wheel:

R – outer radius of the wind wheel; r_g – force application shoulder F_g ; O – the axis of the wind wheel; r – force application shoulder Q_v ; r_l – force application shoulder Q_w .

The moments of forces affecting the propeller, relative to the axis of rotation, is the product of the above forces by the length of the shoulder (Fig.). Let's define the moments value:

$$M_v = Q_v \cdot r ;$$

– the moment made by the air flow with a speed v :

$$M_{wr} = Q_{wr} \cdot r_1 ;$$

– the moment made by the payload of the wind turbine:

$$M_g = F_g \cdot r_g .$$

The total mechanical moment made by the blades of the propeller [1]:

$$M_m = M_v - M_{wr} - M_g ,$$

where Q_v – force application shoulder r ; Q_{wr} – force application shoulder r_1 ; F_g – force application shoulder r_g .

Figures 4 (a-d) show the effect of the speed of rotation of the wind turbine n_1 on the moment of forces M acting on the wind turbine for different speeds of the incoming flow v and different speeds of rotation of the cylinders n . According to the given dependencies, it is possible to determine the speed of free rotation of the wind wheel, i.e. without taking into account the moment of friction forces in the bearings and the moment of forces arising in the generator. The nature of the linear dependence of the values of the moment of forces on the speed of free rotation of the wind wheel does not contradict the results [1] n_1 , rpm.

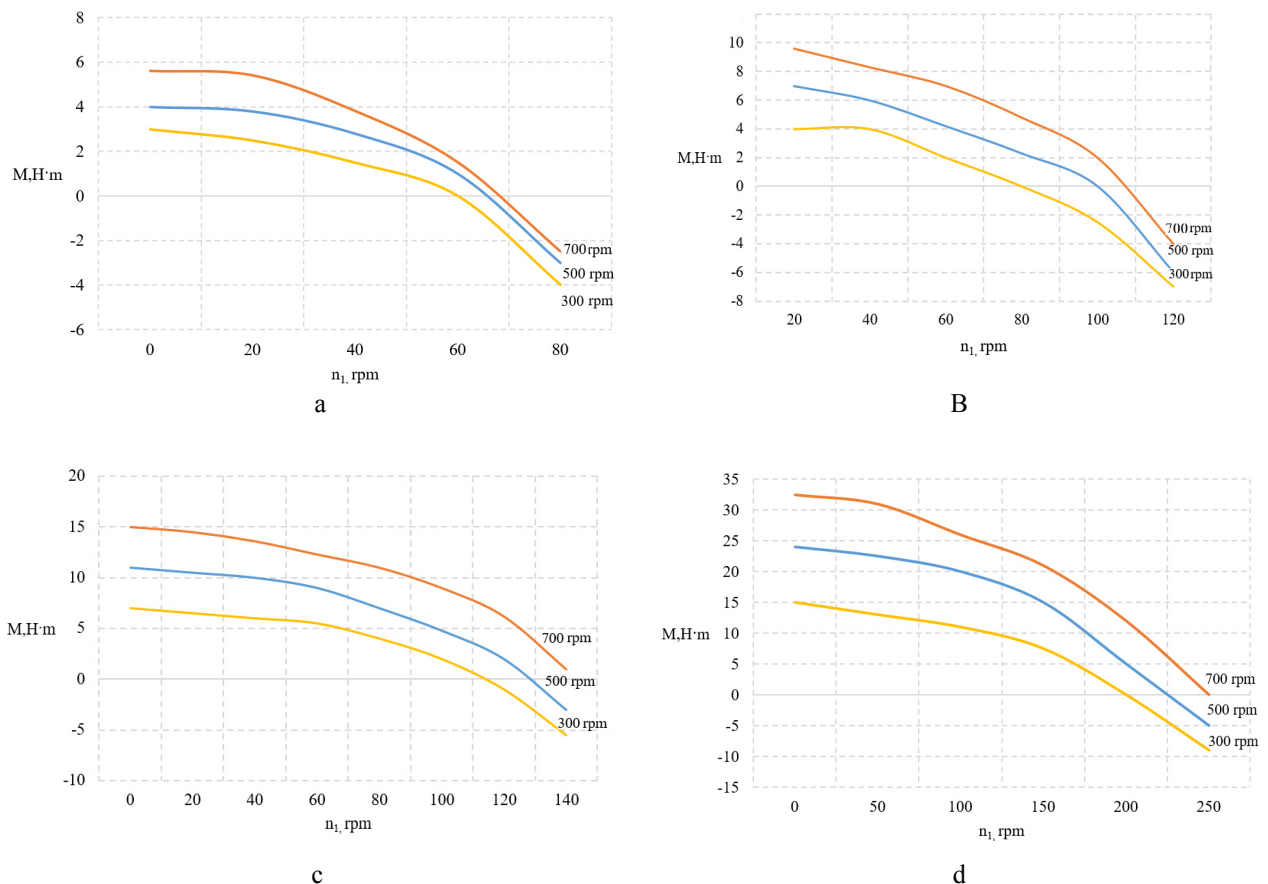


Fig.4. Dependence of the moment of forces on the speed of free rotation of the wind wheel at:
a) $v = 3$ m/s; b) $v = 5$ m/s; c) $v = 7$ m/s; d) $v = 15$ m/s;

As you can see, the results obtained with a sufficient degree of accuracy ($R^2 > 0.9972$) are approximated by dependences of the form:

$$n_1(n, v) = A(n)v^{B(n)} .$$

In this formula the free stream velocity is given in m/s, and the rotation speeds of the cylinder's n and n_1 in rpm. It can be shown that the functions $A(n)$ и $B(n)$ and have the following form: $A(n) = 12.958n^{0.1224}$, $B(n) = 0.4483n^{0.0881}$.

Conclusions

A mathematical model with the computational domain of the wind wheel has been developed using the ANSYS program. A picture of an air flow with a three-dimensional vortex characteristic of a turbulent flow at high Reynolds numbers is obtained. The dependences of the influence of the rotation speed of the wind turbine on the moment of forces acting on the wind wheel are numerically determined at various speeds of the incoming air flow and different speeds of rotation of the cylinders. It has been established that the magnitude of the wind wheel the moment of forces increases in direct proportion to the revolutions number of rotating cylinder and the angular velocity of the wind wheel. It should be noted that the results obtained are valid within the framework of given mathematical model with the accepted assumptions and boundary conditions.

REFERENCES

- 1 Shedlovskii I. A. Experimental study of a multi-blade wind wheel model. *Tekhn. Mekhanika*. 2017, No. 2, pp. 61 – 72. [in Russian]
- 2 Bychkov N.M., Dovgal A.V., Kozlov V.V. Magnus wind turbines as an alternative to the blade ones. *Journal of Physics: Conference Series*. 2007, Vol. 75, pp. 012004.
- 3 Isaev S.A., Baranov P.A., Kudriavtsev N.A., Zhukova Iu.V. Numerical simulation of unsteady heat exchange at a turbulent flow around a circular cylinder. Part 1. Methodic study. *Thermophysics and Aeromechanics*. 2005, Vol.12, No.1, pp. 27-38.
- 4 Marzuki O.F., Mohd Rafie A.S., Romli F.I., et al. An overview of horizontal-axis Magnus wind turbines. AEROTECH VII - Sustainability in Aerospace Engineering and Technology. *Proceeding of the IOP Conf. Series: Materials Science and Engineering*. 2018, Vol. 405, pp. 012011.
- 5 Bobkov V. G., Bondarev A.E., Zhukov V. T., Manukovskii K.V., Novikova N.D., Feodoritova O. B. *Numerical simulation of dynamics of vertical-axis wind turbines. Preprint*. The Keldysh Institute of Applied Mathematics of the RAS. 2019, No. 119, 25 p. doi:10.20948/prepr-2019-119 [in Russian]
- 6 Obukhov S.G. A method for modeling the mechanical characteristics of low-power wind turbines. *Alternative energy and ecology*. 2011, No. 1(93), pp. 12 – 17.
- 7 Lee K.-J., Yang H.-D., Park S.-H., et al. Characteristics of Mechanical and Electrical Power Transmission for Small-Scaled Wind Turbine. *World Journal of Engineering and Technology*. 2016, Vol.4, No. 3D, October 2016. DOI: 10.4236/wjet.2016.43D011 .
- 8 Singh M., Santoso S. *Dynamic Models for Wind Turbines and Wind Power Plants*. National Renewable Energy Laboratory. Texas, University of Texas at Austin, 2011, 115 p.
- 9 ANSYS Fluent software. Available at: www.ansys.com/products/fluids/ansys-fluent
- 10 Computer modeling of 3D-models of aviation equipment and engineering calculations. Available at: www.ipmce.ru/custom/vsop/themes/3dmodel/
- 11 Kussaiynov K., Sakipova S.E., Tanasheva N.K., Kambarova Zh.T., et al. *Wind turbine based on the Magnus effect*. Innovative patent No. 30462. Publ. 23.09.2015, 7 p.
- 12 Sakipova S.E., Tanasheva N.K., Minkov L.L. Modeling aerodynamics of a wind turbine with cylindrical blades in a turbulent air flow. *Eurasian Physical Technical Journal*. Karaganda, 2020, Vol.17, No. 1(33), pp. 106 -112.
- 13 Moon J.S., Manuel L. Toward understanding waked flow fields behind a wind turbine using proper orthogonal decomposition. *Journal of Renewable and Sustainable Energy*. 2012, Vol. 13, pp. 023302; doi.org/10.1063/5.0035751

Article accepted for publication 12.02.2021

DOI 10.31489/2021No1/57-64

UDC 621.577 + 697.1

EFFICIENCY ANALYSIS OF USING A COMBINATION OF AIR AND GROUND HEAT PUMPS FOR HEATING AND VENTILATION

Bezrodny M.K., Oslovskiy S.A.

National Technical University of Ukraine "Igor Sikorsky Kyiv Polytechnic Institute", Kyiv, Ukraine,
work.oslovskiy@gmail.com

The article considers the energy efficiency of the combination of two most common heat sources for heat pumps, namely soil and ambient air. A feature of such a system is the connection of air and ground heat pumps in series with water. A computational model of the proposed system is developed, based on the system of equations for heat and material balances of the system. The result of the analysis was a system of equations, the analysis of which made it possible to study the two main characteristics of energy efficiency, namely, the relative heat load of the ground heat exchanger and the specific total costs of external work for the drive of the system, depending on the depth of utilization of the heat of ventilation emissions. It is shown that a positive effect from the use of a heating and ventilation system with two heat pumps, both in terms of energy and investments, can be achieved with the utilization depth of ventilation emissions corresponding to the condition of equality of the conversion factors for air and ground heat pumps.

Keywords: heat pump, ventilation emissions, soil heat, energy efficiency, specific work, atmospheric air, combination of heat sources.

Introduction

According to the statistics of the International Energy Agency (IEA), in 2019, residential and commercial buildings accounted for 49% of the total final consumption (TFC) of global electricity and 15% of the TFC of fossil fuels [1]. Heating, ventilation and air conditioning (HVAC) systems account for a significant share of total energy consumption in residential and public buildings [2]. Consequently, energy savings in HVAC systems play an important role in improving the overall energy savings of a building. Significant success in solving these problems has been achieved in European countries [3], in the USA [4], in Japan [5], in China [6] and in other regions of the world through the use of heat pump technologies with high energy efficiency in HVAC systems.

At the same time, a number of problems with the use of existing heat pump technologies are determined by the conditions of their application and require their solution. To provide year-round heat supply to buildings, air HP is the most popular type among others [8, 9]. However, it cannot be used in areas with cold winters due to the risk of freezing of the evaporator. When air heaters are used in winter, low ambient temperatures cause a drop in the evaporation temperature, which leads to a catastrophic decrease in efficiency, a drop in condensation temperature or even a system shutdown [10]. In other cases, when air-to-water heat transformers can operate in winter to heat a building, their COP (coefficient of performance) is usually much lower than that of ground-water heat transformers, due to the higher temperature of the heat source - the ground [7].

Therefore, it can be concluded that the use of atmospheric air as a lower source of heat in heat pump heating of buildings is ineffective in latitudes with cold winters [11]. The temperature level of the outside air does not allow achieving the required effect from the use of a heat pump. The authors [12-14] considered various combinations of low-grade heat sources with both air and ground heat pumps, their efficiency and productivity were shown. However, there was a problem of low productivity of a single HPU to provide heat supply for ventilation and air conditioning systems in public buildings with a large volume. For such purposes, it is necessary to choose a heat carrier with a higher temperature potential, but at the same time, it is also easily accessible. This source is the exhaust air from ventilation systems. It should be noted that the use of ventilation emissions as a source of heat has a number of advantages, namely: high and constant temperature potential, reliability, cyclicity of the heat recovery system (the heat spent on heating the supply air is reused) [15]. However, when using an air-to-water heat pump operating on ventilation emissions at

facilities where the consumption of thermal energy by the heating system significantly exceeds that in the ventilation system, the capacity of such a HPU to provide both heating and ventilation may not be enough [16]. This problem can be solved with the help of cascade use of heat pumps with air and ground source of heat. The peculiarity of the proposed solution lies in the use of a series connection by water of condensers of air and ground HP. The use of such a solution at the design stage of the heating and ventilation system will allow balancing the advantages and disadvantages of the two most used types of HP and will create conditions for a more efficient use of heat pump technologies in general.

1. Description of the scheme and problem statement

A schematic diagram of the above-described solution for heat supply of heating and ventilation systems of a building using two series-connected heat pumps (air and ground) is shown in Fig. 1. The main specific characteristic of the presented scheme is the use of air and ground HP connected in series along the water circuit. Analyzing the scheme, you can see that the ventilation emissions with a temperature t_{in} (temperature inside) are injected into the evaporator of the air HP, where it gives off heat to the freon, evaporating it and thereby cooling to the temperature t_{ev} . Next, the coolant is heated in the condenser from the t_r (return water) to the t_g (intermediate). The coolant is heated to the required design temperature t_c by means of ground HP.

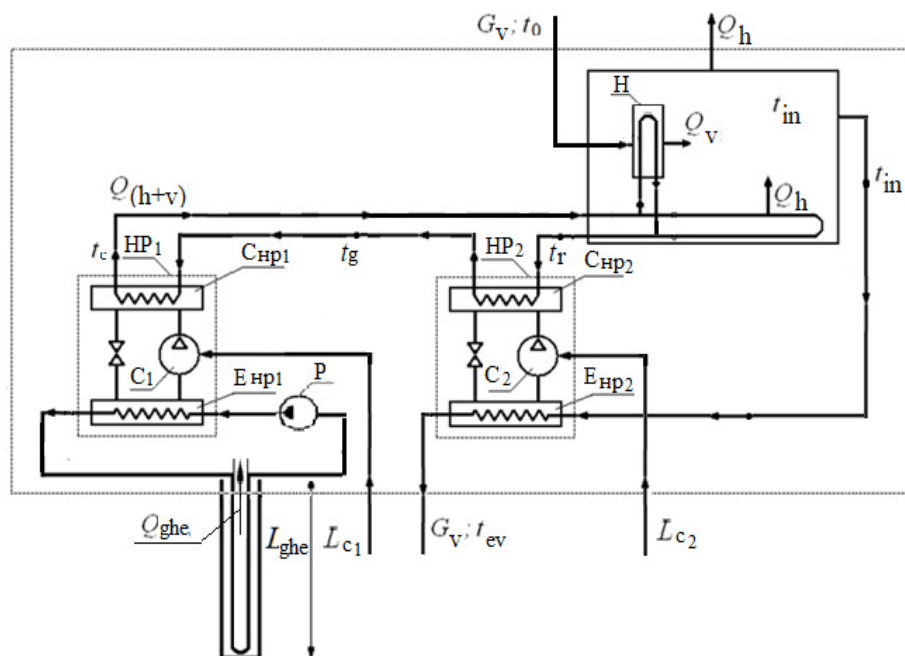


Fig.1. Schematic diagram of a cascade connection of air and ground heat pumps to provide heating and ventilation of the facility: $HP_{1,2}$ – ground and air heat pumps; $C_{HP1,2}$ – condensers of ground and air heat pumps; E_{HP1}, E_{HP2} – evaporators of ground and air heat pumps; C_1, C_2 – compressors of ground and air heat pumps; H – heater of fresh air; P – pump of ground heat pump.

The main objective of the development of this combined solution is the pursuit of waste-free heat production, maximum energy efficiency of the system, as well as minimization of capital costs for the construction of the system. The qualitative and quantitative indicators of these values were determined based on thermodynamic analysis.

2. Efficiency analysis of the considered system

A feature of this scheme is the sequential use of two lower heat sources (heat of ventilation emissions and heat of the ground), which, together with the energy of the compressor drives, must be provided by the heating and ventilation system of the facility. The task is to optimize the use of each of these sources of increasing the system efficiency as a whole. At the same time, an increase in the efficiency of the system implies a decrease in both the energy costs for driving heat pumps and a decrease in the share of the heat load covered by the use of soil heat, which is associated with a decrease in capital costs for the construction

of a ground heat exchanger. It is most convenient to change the proportion of use of individual heat sources by changing the depth of use of the heat of ventilation emissions, setting different levels of air temperature t_{ev} after the evaporator of the air HP. Then, assuming the given temperature t_{ev} , the part of the total heat consumption for heating and ventilation can be determined from the heat balance equation of the entire circuit, which has the form

$$G_v C_v t_0 + Q_{ghe} + L_{c1} + L_{c2} = Q_h + G_v C_v t_{ev}. \quad (1)$$

Introducing into consideration (for the sake of convenience) the base air temperature t_{in} inside the room, equation (1) can be written as

$$G_v C_v (t_{in} - t_{ev}) - G_v C_v (t_{in} - t_0) + Q_{ghe} + L_{c1} + L_{c2} = Q_h \quad (2)$$

Taking into account the balance ratios for the quantities L_{c1} , L_{c2} и Q_{ghe}

$$L_{c1} = \frac{Q_{EV1}}{\varphi_1 - 1} \quad (3)$$

$$L_{c2} = \frac{Q_{EV2}}{\varphi_2 - 1} \quad (4)$$

$$Q_{ghe} = Q_{EV1}, \quad (5)$$

where φ_1 and φ_2 - coefficient of performance (COP) of air and ground HP, equation (2) takes form

$$Q_{EV2} \frac{\varphi_2}{\varphi_2 - 1} + Q_{ghe} \frac{\varphi_1}{\varphi_1 - 1} = Q_h + Q_v. \quad (6)$$

The sum of heat consumption for heating and ventilation is conveniently represented in the form

$$Q_h + Q_v = Q_v \left(1 + \frac{1}{m}\right) = Q_v \frac{m+1}{m}, \quad (7)$$

where $m = Q_v / Q_h$ - the ratio of the heat consumption for ventilation to the heat consumption for heating.

Then, taking into account (7), equation (6) can be written in the form

$$\frac{Q_{EV2}}{Q_v} \frac{\varphi_2}{\varphi_2 - 1} \left(\frac{m}{m+1}\right) + \frac{Q_{ghe}}{Q_h + Q_v} \frac{\varphi_1}{\varphi_1 - 1} = 1, \quad (8)$$

whence the expression for the part of heat of the ground heat exchanger in the total heat consumption for heating and ventilation follows

$$\frac{Q_{ghe}}{Q_h + Q_v} = \left[1 - \frac{t_{in} - t_{ev}}{t_{in} - t_0} \frac{\varphi_2}{\varphi_2 - 1} \frac{m}{m+1}\right] \frac{\varphi_1 - 1}{\varphi_1}. \quad (9)$$

COP φ_1 and φ_2 can be represented in the form of ratios:

$$\varphi_1 = \eta_{HP} \varphi_1^i = \eta_{HP} \frac{1}{1 - \frac{273 + t_{ev}^{ex} - \Delta t_{ev}}{273 + t_c + \Delta t_c}}, \quad (10)$$

$$\varphi_2 = \eta_{HP} \varphi_2^i = \eta_{HP} \frac{1}{1 - \frac{273 + t_{ev}^{ex} - \Delta t_{ev}}{273 + t_g + \Delta t_c}}, \quad (11)$$

where η_{HP} - heat pump loss factor; φ_1^i и φ_2^i - theoretical COP of ground and air HP; t_c - outlet water temperature; t_g - intermediate water temperature; t_{ev}^{ex} and t_{ev} - evaporator outlet water temperature, air and ground HP, respectively.

Water temperature between two HP condensers t_g can be determined from the heat balance of the ground HP

$$Q_{ev} + L_c = Q_c. \quad (12)$$

Taking into account expressions (3), (5) and the expression for the heat flow in the condenser of the ground heat pump

$$Q_c = G_w c_w (t_c - t_g), \quad (13)$$

equation (12) can be written as

$$Q_{\text{ghe}} \frac{\varphi_1}{\varphi_1 - 1} = G_w c_w (t_c - t_g), \quad (14)$$

where the water equivalent $G_w c_w$ can be determined from the heat balance of the upper circuit and has the form

$$G_w c_w = \frac{Q_v}{t_c - t_r} \frac{m+1}{m}. \quad (15)$$

Taking into account equation (15), equation (14) takes the form

$$\frac{Q_{\text{ghe}}}{Q_v} \frac{\varphi_1}{\varphi_1 - 1} = \frac{(t_c - t_g)}{(t_c - t_r)} \frac{m+1}{m}. \quad (16)$$

Determining from (7) and (9) the ratio Q_{ghe}/Q_v and substituting it into (16), we obtain an equation for the intermediate water temperature between air and ground HP

$$t_g = t_c - (t_c - t_r) \left[\frac{t_{\text{in}} - t_{\text{ev}}}{t_{\text{in}} - t_0} \frac{\varphi_2}{\varphi_2 - 1} \frac{m}{m+1} \right] \quad (17)$$

Along with equation (9) for determining the relative power of the ground heat exchanger, an important characteristic of the system efficiency is the specific total consumption of external energy for HP drives

$$l_{\text{h+v}} = \frac{L_{\text{c1}} + L_{\text{c2}}}{Q_h + Q_v}. \quad (18)$$

Taking into account the above relations (3) - (5), as well as (7) and (9), the equation for determining the specific total costs of external energy can be represented in the form

$$l_{\text{h+v}} = \frac{1}{\varphi_1} - \frac{(t_{\text{in}} - t_{\text{ev}})}{(t_{\text{in}} - t_0)} \frac{1}{\varphi_2 - 1} \frac{m}{m+1} \left(\frac{\varphi_1}{\varphi_2} - 1 \right). \quad (19)$$

3. Discussion of results

To implement the numerical solution of the compiled mathematical model of the system under consideration, the following initial data were taken. A low-temperature heat supply system with a temperature schedule of 40/30 was accepted for analysis, taking into account changes in the temperature of the coolant in the supply and return pipelines according to the recommendations [17]. The calculated temperature of the atmospheric air was taken at the level $t_0^e = -20^\circ\text{C}$, and the air temperature in the heat supply facility was $t_{\text{in}} = 20^\circ\text{C}$. The values of the characteristic temperatures of the coolant in the lower circuit of the ground HP were taken taking into account the measurement data in [18, 19], and the temperature difference in the evaporator, taking into account the maintenance of the optimal value in accordance with the analysis in [7]. The ratio of heat consumption for ventilation and heating was taken in the range $m = 0.5 \dots 4.0$ and covers working conditions from individual residential buildings to large shopping centers. The above mathematical model was solved numerically by preliminary determination of the intermediate water temperature t_g according to equation (17) taking into account equations (10), (11) by the method of successive approximations. At the first stage, the determination of the rational depth of use of each of the two lower sources of heat (ventilation emissions and soil) is carried out on the basis of minimizing the specific costs of external energy for the drive of the system by changing the depth of use of the heat of ventilation emissions, setting different levels of air temperature t_v after the evaporator of air heat pump. The calculation results are shown in Fig. 2 in the form of the dependence of the specific energy consumption on the air temperature after the evaporator of the air HP. It can be seen that for all parameters there is an optimal value of the air temperature t_v , at which a minimum of total energy consumption is

provided. This is determined by the different nature of the dependence of the COP of the ground and air HP on the temperature t_v and their different contribution to ensuring the total heat consumption.

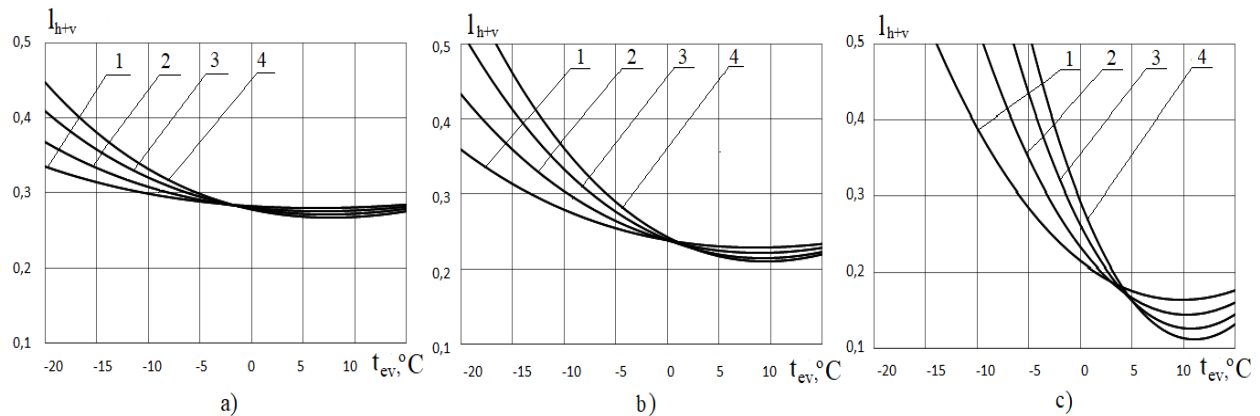


Fig.2. Dependence of the specific consumption of external energy on the temperature at the outlet of the evaporator of the air HP: a-c – temperature $t_0 = -20; 0; 15$ °C respectively; 1-4 – $m = 0,5; 1; 2; 4$ respectively.

In fig. 3 shows the dependence of the detected optimal values of the air temperature t_v on the temperature of the atmospheric air and the parameter m . It can be seen that the optimal values of the temperature t_v increase with an increase in both the outside air temperature and the parameter m . At the same time, attention is drawn to the high level of temperatures of the air discharged into the atmosphere, that is, the low depth of use of the heat of the exhaust ventilation air [20]. As a result, the total heat load on the system is covered mainly by the operation of the ground heat exchanger, which is associated with an increase in the productivity of the ground heat exchanger and, as a consequence, the capital costs of its construction.

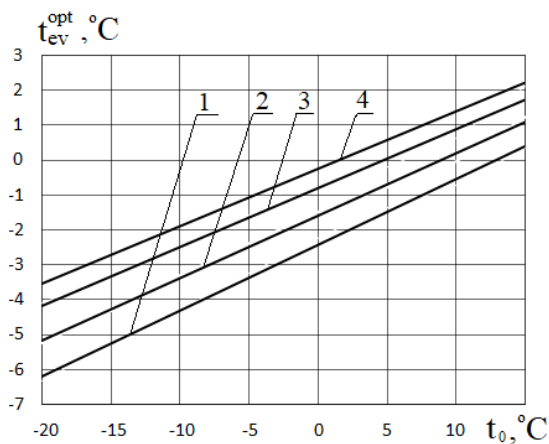


Fig.3. Dependence of the optimum air temperature at the outlet from the evaporator of the air HP on the outside air temperature: 1-4 – $m = 0,5; 1; 2; 4$ respectively.

In this regard, it becomes expedient to consider other options (levels) of the heat load of the air HP or the depth of use of the heat of ventilation emissions [21]. Such an option can be the heat load of the air HP, selected from the condition of the same efficiency of operation of both heat pumps, that is, from the condition of equality of their COP. For this purpose, the corresponding COPs of two HP are shown in Fig. 4 depending on the temperature t_v at different values of the parameter m and the outside air temperature. As seen from Fig. 4, the points of intersection of individual curves for the air HP and the dashed line for the ground HP correspond to different values of the air temperature at the outlet from the evaporator of the air HP, which satisfies the condition of equality of COP for both HP [22]. The dependence of these temperatures on the outside air temperature and parameter m is shown in Fig. 5. The data in Fig. 5 indicate that the level of air temperatures at the outlet of the evaporator of the air HP under this condition is significantly lower than in Fig. 3 under the previously considered condition of the minimum total external work.

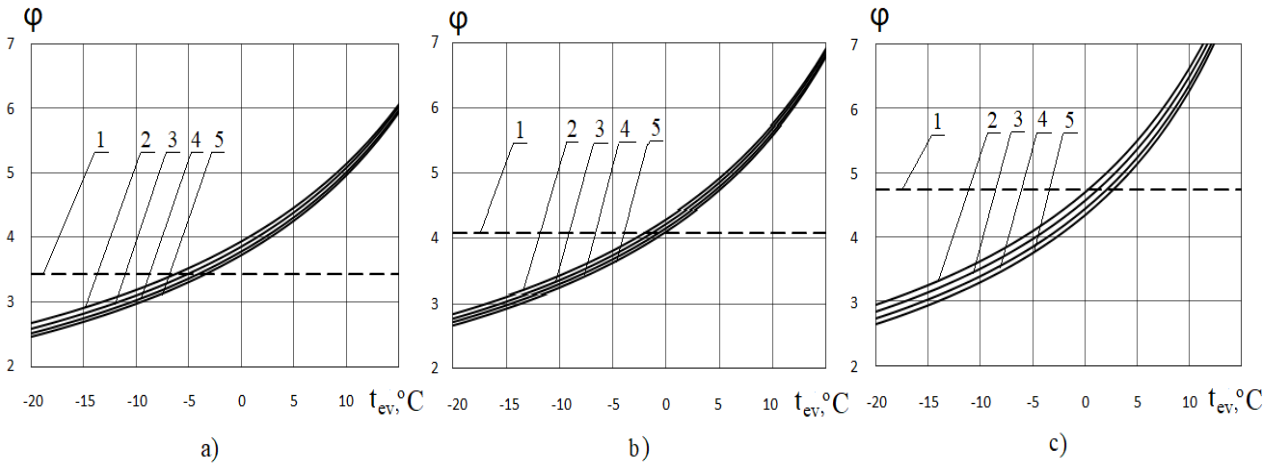


Fig. 4. Dependence of the transformation ratio on the air temperature at the outlet of the evaporator of the air HP: a-c – $t_0 = -20; 0; 15$ °C respectively; 1 – φ_1 ; 2-5 – φ_2 at $m=0.5$; 1; 2; 4 respectively.

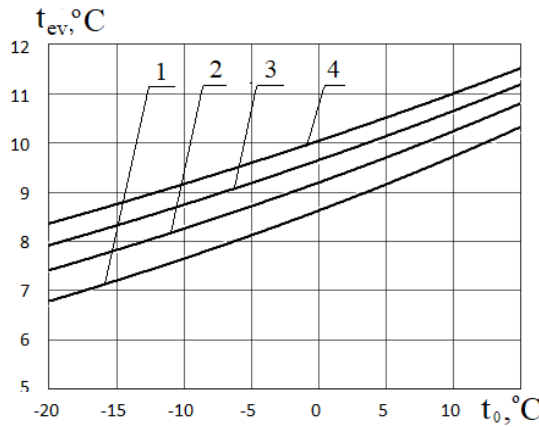


Fig. 5. Dependence of the air temperature at the outlet from the evaporator of the air HP on the outside temperature (COP equality condition): 1-4 – $m=0.5; 1; 2; 4$.

This indicates a greater load of the air HP and a lower thermal load of the ground HP, and, consequently, the lower required performance of the ground heat exchanger and the corresponding capital costs for its installation. Fig. 6 shows the dependence of the relative heat load of the ground heat exchanger on the outside air temperature and parameter m under three comparison conditions (minimum external work, equal COP and complete heat recovery from the exhaust ventilation air).

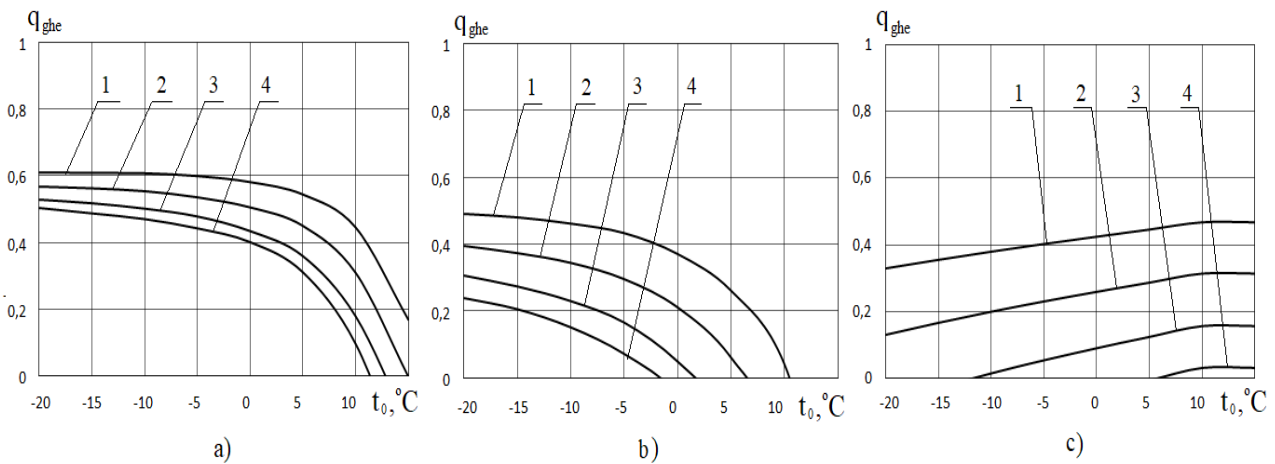


Fig. 6. Dependence of load part of the ground heat exchanger in the total heat flow for heating and ventilation on the outside air temperature: a) condition for minimum unit energy consumption; b) COP equality condition; c) $t_{ev} = t_0$ condition, where 1-4 – $m = 0.5; 1; 2; 4$.

It can be seen that a relatively small decrease in temperature t_v to the level at which the equality of COP is observed (Fig. 6, b), significantly reduces the relative power of the ground heat exchanger. A further decrease in the temperature t_v to the outside air temperature (Fig. 6, c) leads to a qualitative change in the nature of the dependences, but does not cause particularly sharp quantitative changes in the value of q_{ghe} .

The dependence of the second important characteristic of the heat pump system - the specific consumption of external energy for the drive of the system - is shown in Fig. 7. It can be seen that the achievement of the COP equality condition (Fig. 7, b) has almost no effect on the amount of external work on the system drive, which does not depend on the ratio of heat consumption for ventilation and heating.

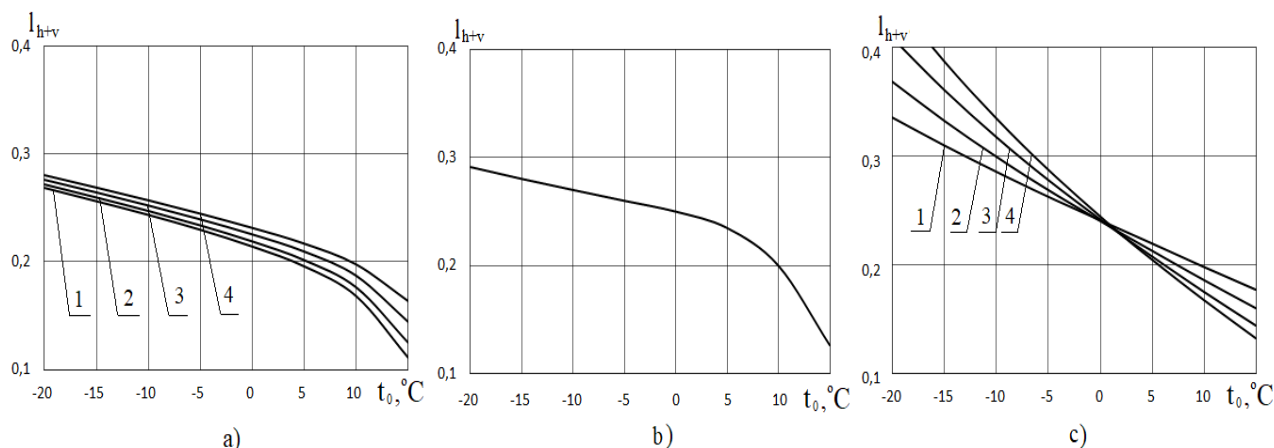


Fig.7. Dependence of the specific consumption of external energy for the system on the outside temperature: a) condition for minimum unit energy consumption; b) COP equality condition; c) $t_{ev} = t_0$ condition, for 1-4 $m=0,5; 1; 2; 4$.

At the same time, a further decrease in the temperature t_v to the level t_0 leads to a sharp increase in the specific work in the region of low outdoor temperatures. As a result, it can be concluded that the utilization of the heat of ventilation emissions in the considered heat pump system may be advisable when the air temperature after the evaporator of the air HP is reduced only to a level corresponding to the condition of equality of the COP of the air and ground heat pumps.

Conclusions

1. The use of a combined heat pump system for heating and ventilation of large facilities using air and ground heat pumps with its rational design can give a positive effect both in terms of energy and investment.
2. Rational design of a heating and ventilation system with two heat pumps can be carried out on the basis of a joint analysis of two most important characteristics of such a system, namely, the relative heat load of the ground heat exchanger and the specific total costs of external work on the system drive, depending on the depth of use of the heat of the ventilation emissions.

The analysis showed that a positive both energy and investment effect can be achieved at the depth of utilization of ventilation emissions, corresponding to the condition of COP equality of air and ground heat pumps.

REFERENCES

- 1 IEA, Renewable Energy Policies in a Time of Transition. *International Energy Agency*. 2020. Available at: <https://webstore.iea.org/download/direct/426>.
- 2 Katsura T. Development of optimum design method for the heat recovery ground source heat pump system. *Proceeding of the 12th IEA heat pump conference 2017*. Rotterdam, 2017, No. 17, pp. 4 – 8.
- 3 Ürge-Vorsatz D., Cabeza L., Serrano S., Barreneche C., Petrichenko K. Heating and cooling energy trends and drivers in buildings. *Renewable and Sustainable Energy Reviews*, 2015, No. 41, pp. 31–52.
- 4 Willem H., Lin Y., Lekov A. Review of energy efficiency and system performance of residential heat pump water heaters. *Energy and Buildings*, 2017, No. 143, pp. 191–201.
- 5 IEA, World Energy Outlook. *International Energy Agency*, 2019. Available at: www.iea.org/reports/world-energy-outlook-2019.

- 6 Chang J., Liu H., Wang C., Liu M. The applications and economic analysis of Ground Source Heat Pump (GSHP) in certain national games sports centre. *Procedia Engineering*, 2017, No. 70, pp. 12–36.
- 7 Bezrodny M. K., Pritula N.O. *Thermodynamic and energy efficiency of heat pump heat supply circuits: monography*, Kyiv, Polytechnica, 2016, 272 p.
- 8 Menberg K., Heo Y., Choi W., et al. xergy analysis of a hybrid ground-source heat pump system. *Applied Thermal Engineering*, 2017, No. 46, pp. 949–958.
- 9 Christodoulides P., Aresti L., Florides G. Air-conditioning of a typical house in moderate climates with ground source heat pumps and cost comparison with air source heat pumps. *Applied Thermal Engineering*, 2019, No. 158, pp. 77–83.
- 10 Wang Z., Wang F., Liu J., et al. Field test and numerical investigation on the heat transfer characteristics and optimal design of the heat exchangers of a deep borehole ground source heat pump system. *Energy Conversion and Management*, 2017, No. 153, pp. 15–34.
- 11 Sarbu I., Sebarchievici C. General review of ground-source heat pump systems for heating and cooling of buildings. *Energy and Buildings*, 2014, No. 54, pp. 27 - 51
- 12 Bezrodny M.K., Prytula N.O., Oslovskiy S.A. Thermodynamic efficiency of the heat pump heating scheme using ground and waste water heat. *Research Bulletin of the National Technical University of Ukraine "Kyiv Polytechnic Institute"*, 2018, No. 1, pp. 7–15.
- 13 Bezrodny M.K., Prytula N.O., Oslovskiy S.A. Analysis of the combined heat pump heating scheme using heat of atmospheric air and sewage water. *Energy technology and resource conservation*, 2018, No. 5, pp. 12–20.
- 14 Bezrodny M.K., Oslovskiy S.A. Energy efficiency of the heat pump recuperative heating and ventilation system using heat of ground and ventilation emissions. *Power engineering: economics, technique, ecology*, 2018, No. 3, pp. 95–103.
- 15 Ishehri F., Beck S., Ingham D., et al. Techno-economic analysis of ground and air source heat pumps in hot dry climates. *Journal of Building Engineering*, 2019, No. 26, pp. 144 - 151.
- 16 Puhovy I., Postolenko A., Radchuk U. Analysis of heat supply schemes with two heat pumps and the use of ventilation emissions and air heated by the heat of water crystallization. *Renewable Energy*, 2014, No. 4, pp. 75–80.
- 17 Slastin A. Temperature dependence. 2020. Available at: www.ktto.com.ua/calculation/temperaturnyy_grafik [in Russian]
- 18 Kostikov A. O. Kharlampidi D. K. Influence of the thermal state of the soil on the efficiency of a heat pump installation with a ground heat exchanger. *Power engineering: economics, technique, ecology*, 2009, No. 1, pp. 32–40.
- 19 Basok B. I., Avramenko A.A., Ryzhkov S.S., Lunina A.A. The dynamics of heat transfer of liquid in a single rectilinear soil pipe element (heat exchanger). *Industrial heat engineering*, 2009, No. 1, pp. 62–67.
- 20 Qu M., Li T., Deng S., Fan Y, Li Z. Improving defrosting performance of cascade air source heat pump using thermal energy storage based reverse cycle defrosting method. *Applied Thermal Engineering*, 2017, No. 36, pp. 67–74.
- 21 Zeng C., Liu S., Shukla A. A review on the air-to-air heat and mass exchanger technologies for building applications. *Renewable and Sustainable Energy Reviews*, 2017, No. 75, pp. 137–144.
- 22 Bezrodny M.K., Misiura T.O. The heat pump system for ventilation and air conditioning inside the production area with an excessive internal moisture generation. *Eurasian phys. tech. j.*, 2020, Vol. 17, No. 2(34), pp. 78 – 86.

DOI 10.31489/2021No1/65-69

UDC 577.31

INFLUENCE OF THE IMPACT OF ACOUSTIC CAVITATION ON THE PHYSICAL AND CHEMICAL PROPERTIES OF WATER

Dyussenov K. M., Sakipov K.E., Shayakhetova R.T., Nedugov I.A.,
Aitmagambetova M. B., Yessimseit A.K.

L.N. Gumilyov Eurasian National University, Nur-Sultan, Kazakhstan, sakamer2100@gmail.com

The article presents the results of an experimental study of the changing the ionic composition of water under the influence of acoustic cavitation. The effect of acoustic radiation on the physical and chemical properties of water was studied in the frequency range 20 Hz - 50 kHz. It is shown that the ultrasonic range leads to an increase in the concentration in the area of metal traces and affects the change in the pH of water. The mechanism of action of cavitation leads to a change in the structural characteristics of water. It is shown that one of the manifested effects of ultrasonic cavitation can be used for various applications.

Keywords: ultrasound, acoustic emission, cavitation, mass spectrometric analysis.

Introduction

The data of the materials of the International Committee on Water Resources at the UN (United Nations), WHO (World Health Organization) and other generally recognized and specialized international expert organizations that fresh and especially drinking water will become a strategic resource by 2025 are well known. Water quality issues for drinking, agricultural irrigation and irrigation are becoming more acute. The relevance and relevance of practical applications in the field of water treatment and treatment is beyond doubt. The boom in demand for nanotechnology, new technologies in various ways of structuring water, other liquids and solutions is growing exponentially. In work [1], a wide range of applications of acoustic (ultrasonic) and hydrodynamic cavitation in various fields of science and high technologies was thoroughly investigated. Changes in the properties of water under the influence of hydrodynamic cavitation were also noted in [2], where studies were carried out on the basis of numerical modeling. The range of technical applications of hydrodynamic and ultrasonic cavitation in the world is rapidly expanding when they are directly used in medicine, naval affairs, pharmaceuticals, chemical technologies, cosmetics and cosmetology, etc. pressure of hydraulic microjets up to 40 MPa causes ionization of water and aqueous solutions and is accompanied by many poorly studied processes.

Studies of the influence of hydrodynamic cavitation on the change in the physicochemical properties of aqueous solutions are devoted to works [3-5], and works [6, 7] are shown to purify water both from bacteria and other contaminants, and to disinfect water. Ultrasonic cavitation can also lead to changes in cellular structures, as shown in [8], and can be used in cancer therapy. The phenomenon of hydrodynamic cavitation was also used to purify water from pharmaceutical contaminants [9]. It is known that it influences the growth and development of cell structures and the transfer of various substances into cells under the influence of acoustic frequencies and cavitation of a different spectrum [10, 11]. For example, in [12, 13], the influence of ultrasonic acoustic emission, accompanied by cavitation, on various structural characteristics of water, including some aspects of physical chemistry and microbiological composition, was studied.

It is obvious that the use of hydrodynamic and ultrasonic cavitation is an example of nanotechnology, and many aspects of this effect are poorly understood. The questions were studied in detail and the results of the influence of the infrasonic spectrum of oscillations on the growth of some types of cereals were used. The issues of structuring water under the influence of cavitation continue to be studied and are of interest in various fields, including crop production and agricultural technology.

1. Experimental part. Materials and method

For this, two experimental installations were created for the generation of infrasound and ultrasound with the subsequent transfer of the pulse to piezoelectric transducers (emitters). The generator unit consists of a pulse generator and a frequency amplification unit of a special shape, a power supply unit and a control

panel. Direct action on water is carried out in a radiation installation through piezoelectric transducers using a device for generating infrasound and ultrasound (Fig.1), [14]. The frequency spectrum of radiation before and after experiments on the effect of irrigation with acoustic vibrations was recorded using a VALLEMAN PC SGU250 broadband oscilloscope and the adjustment range was from 20-50 Hz on the first block to 20-50 kHz per second.

The water was subjected to ultrasonic action using the emitters shown schematically in Fig. 2. Ultrasonic emitters are made in the form of flat piezoelectric emitters for generating ultrasonic pulses located on the inner surface equidistantly relative to the flow path of the cavitation generator on two opposite sides and connected in parallel with the formation of a cavitation field directed perpendicular to the fluid flow.



Fig.1. The device for generating infrasound and ultrasound.

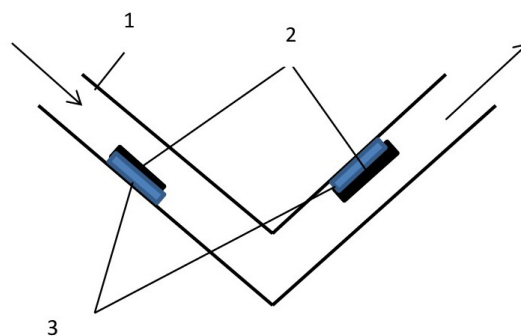


Fig.2. Emitter layout.

Ultrasonic piezoelectric emitters are made of barium titanite, which allows generating a high-frequency spectrum of ultrasonic radiation. The ultrasonic emitters are rigidly fixed to the nozzle, for example, using a composite adhesive and are completely sealed against the corrosive effects of a liquid medium. Water flows through the inlet nozzle 1 and under the influence of ultrasonic transmitters 2 rigidly fixed to the inner surface of the dielectric wall nozzle using an adhesive or adhesive material such as composite adhesive 3 (Fig. 2). The coolant is exposed to ultrasonic action due to pulses supplied from ultrasonic transducers 2, which are turned on perpendicular to the direction of fluid flow. The frequency spectrum of ultrasonic transducers varies from 20 KHz to 50 MHz, and the "traveling wave" is generated by an adjustable microprocessor and is automatically correlated with the flow rate of the coolant. Since the frequency of the radiation spectrum is adjustable, this makes it possible to control the processes of the intensity of the generation of cavitation cavities, depending on a number of physical factors, including both the speed and flow rate of the coolant flow, and the diameter of the inlet pipe. Along the length of the zone of action of ultrasonic emitters 2, cavitation cavities begin to form in the entire volume of the inlet pipe of the moving coolant, which, after passing the inlet pipe, begin to "collapse" (collapse), while releasing the amount of heat adequate to the breaking energy of intermolecular bonds. In addition, the effect of "cold boiling" or the formation of cavitation cavities with their subsequent collapse (collapse) leads to ionization of the coolant throughout the volume of the supply pipe and a controlled change in its physicochemical properties.

In [15] on physical and technical acoustics, ultrasonic cavitation usually means the formation of discontinuities in the continuity of a liquid medium under the action of tensile stresses in the rarefaction phase, the emergence of unstable vapor-gas cavities and the subsequent collapse of these cavities in the compression phase.

2. Results and Discussion

The frequency spectrum of the radiation in the range 20-50 Hz virtually did not affect the pH of irrigation water. The most characteristic effects on the structure of irrigation water at 20 Hz manifested in increasing cadmium concentration by almost 92% zinc and almost 7 times. As seen from the integrating spectrograms where abscissa mg dm⁻³ drawn on generalized results of analyzes of samples (Fig. 3, 4) with a sharp increase in the concentration of cadmium Cd (about 4 times), and tin Sn (by 11 times) the remaining group trace metals have remained virtually unchanged.

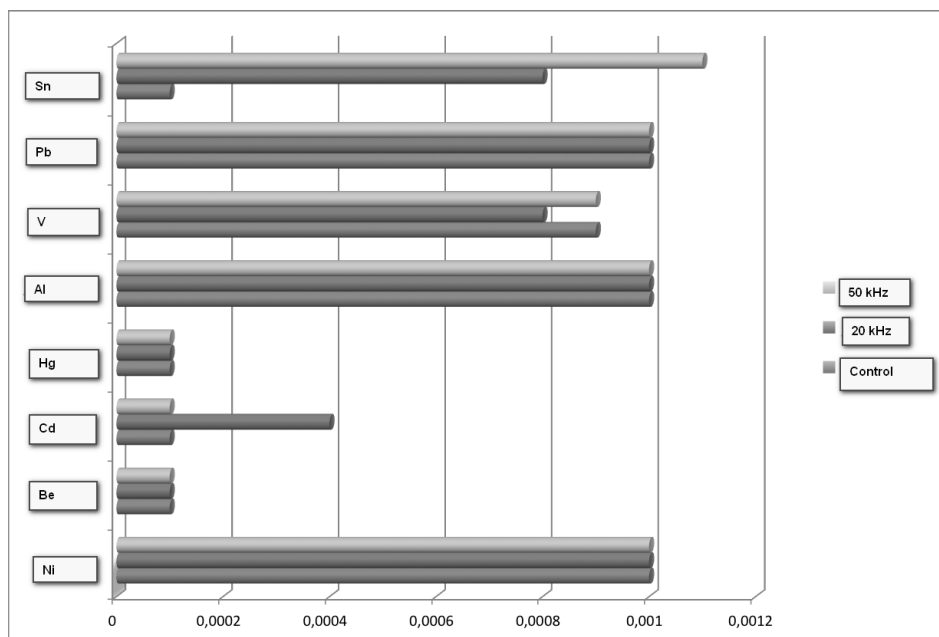


Fig. 3. The increasing of Sn and Cd concentration in water after ultrasound influence

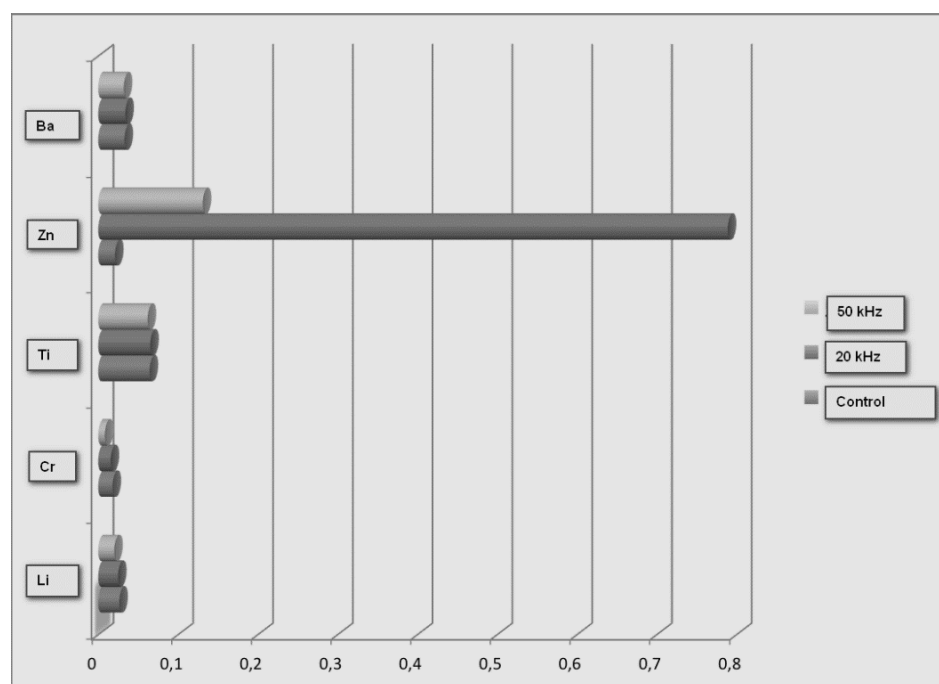


Fig.4. The increasing of Zn concentration in water after ultrasound influence.

At the same time, the content is within the MPC as the EU countries and the United States, Russia and the MAC recommended by WHO. For example, MPC WHO compared with the obtained data are shown in Table. 1. The highest efficiency of irrigation water gave exposed to ultrasound in a range close to 20 kHz, the second pilot unit.

Table 1. The comparative characteristics of the content of trace minerals

MAC (WHO), mg/dm ³	After influence 20 kHz, mg/dm ³	After influence 50 kHz, mg/dm ³
Cu 0.20	0.14	0.136
Zn 0.30	0.231	0.148
Cd 0.003	0.00039	0.00011

Results of averaged spectrograms in mg/dm^3 (Fig. 5 - 6) show that a pronounced positive effect on the growth of tomato at a frequency range of 20 kHz the radiation had growth of concentration iron of 22%, copper Cu in 1.6 times and manganese Mn by 8 times.

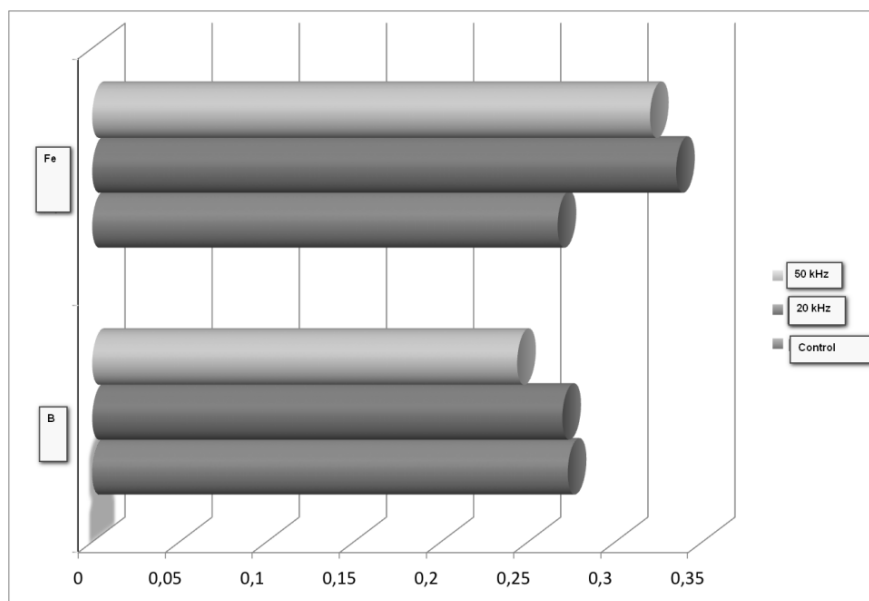


Fig.5. The increasing of Fe concentration in water after ultrasound influence

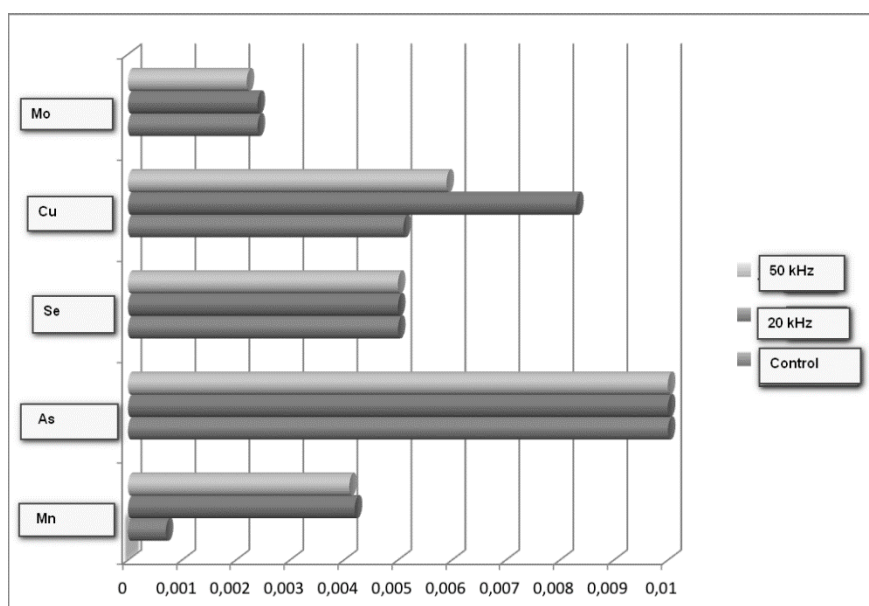


Fig.6. The increasing of Cu and Mn concentration in water after ultrasound influence

Thus, minor, an average of 1.14 - 2.01% grew acidity (pH) of the treated water for irrigation at 20 kHz and at a frequency of 50 kHz pH values increased to 3.28%. Analysis of the spectrograms and measurement of irrigation water pH after ultrasonic treatment led to the conclusion that the water gets new properties related to its partial ionization leading to changes in its molecular structure.

A number of works are known, among them [15], where various scientific explanations of the phenomenon of hydrodynamic and ultrasonic cavitation are given, accompanied by the processes of changing the mechanism of microalgae development. It is the cavitation mechanism that causes new effects of molecular changes in the structural characteristics of algal cells was shown in these studies.

It is quite obvious that ultrasonic and hydrodynamic cavitation has a rather complex mechanism of affecting water and aqueous solutions and is manifested in many physical and chemical aspects. Mass spectrometric analysis of irrigation water allowed to illustrate that partial ionization of irrigation water

occurs with activation of metal ions dissolved in it. In all probability, the activated metal ions, the concentration of some of which increased several times in the form that ultrasonic cavitation caused, greatly improve and intensify plant growth and appear as one of the factors contributing to this.

Conclusions

For the first time, data were obtained on the change in the physicochemical properties of water under the influence of ultrasonic cavitation in the radiation range from 20 to 50 kHz. The accuracy and reproducibility of all experimental data in the specified frequency range fully meet the standard requirements. The measuring equipment used in the work meets international quality and accuracy standards. Changes in the physicochemical properties of water affect the complex mechanism of the physical effects of cavitation, which were analyzed on the basis of data from other authors. The effects of sono luminescence, the collapse of cavitation microbubbles lead to additional ionization and activation of water. The data presented on the change in the structure of water after exposure allow us to conclude that cavitation has a significant effect on the molecular composition of water. The analysis of the effect of ultrasonic cavitation on water brings new knowledge and data in a deeper study of the phenomenon of cavitation. The data on the increase in the concentration of ions of dissolved metals obtained using mass spectrometry and changes in the pH of water make it possible to expand the range of scientific data on the practical use of this effect in various agrotechnical and engineering applications.

REFERENCES

- 1 Li B., Gu Yo., Chen M. Cavitation inception of water with solid nanoparticles. A molecular dynamics study. *Ultrasonics –Sonochemistry*. 2019, Vol. 51, pp. 120–128.
- 2 Yusvika M., et al. Cavitation Prediction of Ship Propeller Based on Temperature and Fluid Properties of Water. *Journal of Marine Science and Engineering*, 2020, Vol. 8, Iss. 6, pp. 2-21.
- 3 Loraine G., Chahine G., Hsiao C.T., Choi J.K., Aley P. Disinfection of gram-negative and gram-positive bacteria using DynaJets ® hydrodynamic cavitating jets. *Ultrasonics Sonochemistry*, 2012, Vol. 19(3), pp. 710 – 715.
- 4 Badve M., et al. Hydrodynamic cavitation as a novel approach for wastewater treatment in wood finishing industry. *Separation and Purification Technology*. 2013, Vol.106, pp. 15 – 21.
- 5 Vasenin I.M., Narimanov R.K., Perchatkina E.V., Shrager L.A. Investigation of two phase flow motion with small-size gas bubbles. *Eurasian Physical Technical Journal*, 2019, Vol.16, No.2 (32), pp. 48 – 54.
- 6 Al-Mahrouki A.A., Karshafian R., Giles A., Czarnota G.J. 2012. Bioeffects of ultrasound-stimulated microbubbles on endothelial cells: Gene expression changes associated with radiation enhancement in vitro. *Ultrasound Med Biol*. 2012, Vol.38, pp. 1958 – 1969.
- 7 Kuwabara Mamoru, Yo Ken, Kubo Takashi. Sono-processing of materials based on an acoustic cavitation phenomenon. *Journal of Current Advances in Materials and Processes*. 2005, Vol.18, No. 4, pp. 962 – 969.
- 8 Zupanc M., Tina Kosjek T., Petkovšek M., et al. Shear-induced hydrodynamic cavitation as a tool for pharmaceutical micropollutants removal from urban wastewater. *Ultrasonics Sonochemistry*, 2014, Vol. 21, Issue 3, pp. 1213 – 1221.
- 9 Chuang Y.H., Cheng P.W., Chen S.C., et al. Effects of ultrasound-induced inertial cavitation on enzymatic thrombolysis. *Ultrason Imaging. Apr.* National Taiwan University, Taipei, Taiwan. 2010, Vol. 32(2), pp. 81-90.
- 10 Riesz P., Berdahl D., Christman C.L. 1985. Free radical generation by ultrasound in aqueous and nonaqueous solutions, *Environ Health Perspective*. 1985, Vol. 64, pp. 233 – 252.
- 11 Hernández-García D., Castro-Obregón S., Gómez-López S., Valencia C., Covarrubias L. Cell death activation during cavitation of embryoid bodies is mediated by hydrogen peroxide, *Experimental Cell Research*, 2008, Vol. 314, Issue 10, pp. 2090 – 2099.
- 12 Villanueva M.V., Luna M.C., Gil M.I., Allende A. Ultrasound treatments improve the microbiological quality of water reservoirs used for the irrigation of fresh produce. *Food research international*. 2015, Vol. 75, pp. 140 – 147.
- 13 Pan Li, Yuan Song, Shuili Yu, Hee-Deung Park. 2015. The effect of hydrodynamic cavitation on *Microcystis aeruginosa*. *Physical and chemical factors. Chemosphere*, 2015, Vol. 136, pp. 245 – 251.
- 14 Dyussenov K., Nedugov I. *Cavitation energy converter*: Patent Provisional Application, USA, Number 61745772. Publ. 25.12.12, 21 p.
- 15 Nyborg, W.L. *Physical Mechanisms for Biological effects of Ultrasound*. DHEW 78-8062. Washington, D.C., U.S. Government Printing Office, 1977, pp. 59-64.

DOI 10.31489/2021No1/70-74

UDC 536.631

INVESTIGATION OF THE THERMOPHYSICAL CHARACTERISTICS OF MINERALS AT VARIOUS HEATING PARAMETERS

Shaimerdenova K.M., Stoev M., Sekerbayeva G.K., Bulkairova G.A.,
Ospanova D.A., Tussypbayeva A.S., Rakhmankyzy A.

¹E.A. Buketov Karaganda University, Karaganda, Kazakhstan,

The study of natural minerals in the production of heat and electrical insulating materials is of particular practical interest for the study of their thermophysical characteristics. The regularities of changes in the heat capacity of minerals when heated in production and operating conditions are of particular interest. Natural minerals of wollastonite and quartz were considered as the object of research. The heat capacity of these minerals was measured in an apparatus with a three-dimensional sensor and a panel for automatic control of gas flows, when heated to the temperature of 1600°C by the calorimetric method. Based on the experimental results, graphs of the dependence of the heat capacity of mineral samples on temperature were constructed.

Keywords: wollastonite, quartz, differential scanning calorimetry, heat capacity, thermal condition.

Introduction

The problem of theoretical and experimental study of the properties of natural minerals remains relevant. To know the thermo-physical properties of substances under different variable temperature conditions is important for several reasons. Here it is important to define the thermo-physical characteristics of natural minerals, those of building, heat-insulating, facing materials and products and their recyclability. The thermo-physical characteristics of closed structures affect the thermal and air conditions of buildings for various purposes, as well as ventilation and air quality, which currently consume a significant amount of thermal energy, as well as the operation of heating systems.

One of the most promising areas of science and practice for improving the grinding process is target-specific changing the properties and state of natural minerals [1]. Stationary, non-stationary and complex methods based on the theory of thermal conductivity are used to determine the thermo-physical characteristics of minerals and materials in stationary or non-stationary thermal conditions. In addition, these methods can be absolute and relative [2]. Natural minerals are widely used as heat insulators in metal smelting, heating, various wall-mounted boilers, and electric heaters. In foundry and metallurgy, heat-resistant molding materials, especially in powder form, diatomaceous earth and other refractory materials are used. The extraction of high-melting and heat-resistant minerals in the Republic of Kazakhstan is of particular interest. Currently, the minerals of the Republic of Kazakhstan are used for the manufacture of raw bricks, houseware, souvenirs, various parts of electric stoves, ovens, etc. [3, 4].

1. Experimental part

The heat capacity of the whole body is taken into account when studying the structure of substances and their properties, studying phase transitions and critical phenomena, calculating the total amount of impurities in a substance, determining the thermal effects of chemical reactions. In addition, heat capacity as a thermo-physical parameter is an effective tool for scientific research. The determination of the heat capacity of natural minerals was carried out in the LABSYS™ EVO apparatus with synchronous thermo-gravimetric, differential thermal analysis, a 3D sensor at a temperature of up to 1600 °C and an automatic gas flow control panel (LABSYS™ EVO TG, DTA, DSC 1600 °C) in the “Methods of physical and chemical research” engineering laboratory of Karaganda E.A. Buketov University (Fig. 1) [5].



Fig.1. LABSYS™ EVO thermal analyzer (main view)

The work is carried out as follows: using a laboratory balance, the mass of the studied minerals is determined: wollastonite, quartz samples from two deposits (Aktas) and (Nadyrbai). The sample weights are, respectively, equal: wollastonite – 8 mg, quartz (Aktas) – 9.36 mg, and quartz (Nadyrbai) – 9.6 mg.

Differential Scanning Calorimetry (DSC) is a method in which the difference in heat flows applied to the crucible with the test sample and the reference crucible is measured as a function of temperature and/or time during the exposure of the test and reference samples to a controlled temperature program under a specified atmosphere and using symmetrical measuring system. The use of DSC makes it possible to significantly reduce the time for conducting experiments and to obtain experimental data on the specific heat capacity of the investigated products with an error of no more than 3%.

Two valved crucibles are placed in the DSC measuring chamber, the test sample is placed in the first one, and the second is used as a reference (free) crucible. The material of the crucible is set depending on the maximum heating temperature of the sample and the tested substance, which should not react with the crucible. In the experiment, platinum was used (up to 1000° C) as the crucible material. The experimenters run the apparatus program and set the parameters to perform the required thermal scanning. During the experiment the program of continuous heating was used. After starting the device, measurements were taken.

The temperature was determined using the thermocouples in the measuring chamber of the calorimeter. When the sample begins to heat up, heat is released. Then the system can measure and analyze the change in specific heat. The melting points of the tested natural minerals were obtained from the reference data. Accordingly, the melting points of minerals are: wollastonite – 1400-1500° C, quartz (Aktas) – 1710-1720 ° C, quartz (Nadyrbai) – 1710-1720 ° C. These values are necessary so that when minerals are heated, their temperature values exceed the specified range.

Specific heat c_p , J/g·K is calculated by the formula

$$c_p = m^{-1}C_p = m^{-1}(dQ/dT)_p, \quad (1)$$

where m is the mass of the sample, g; C_p is the heat capacity, J/K; dQ is the amount of heat, J, required to increase the temperature of the material by dT , K.

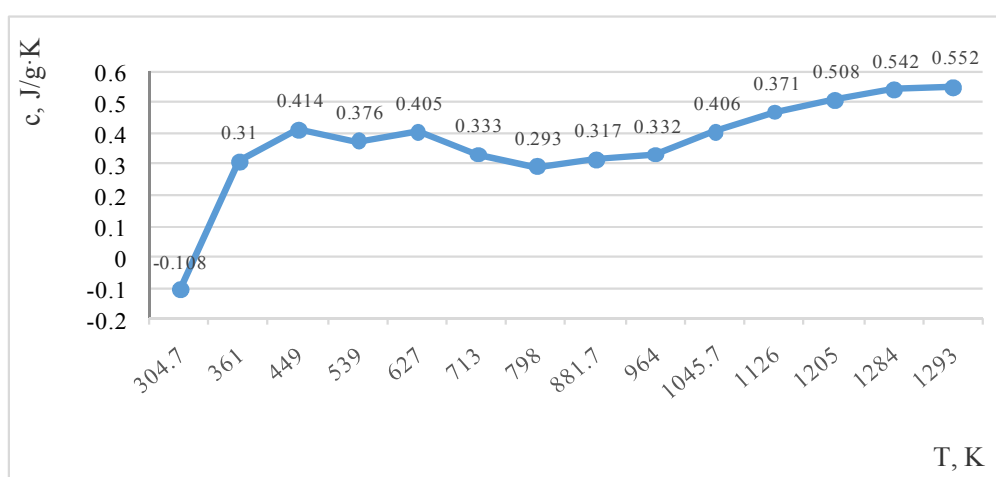
The subscript indicates an isobaric process. According to experiment, the specific heat capacities of natural minerals are determined by the proposed formula (1), which represents the amount of heat absorbed by a unit mass of material when heated by 1K at constant pressure. By calculating the dependence of the specific heat capacity of mineral samples on temperature are obtained.

2. Discussion of results

Using the results obtained, a graph of the dependence of the specific heat capacity on temperature $c=f(T)$ is plotted. The experimental values of the heat capacity of minerals are given in Table 1. The plot of the obtained heat capacity versus temperature for wollastonite under the thermal condition is shown in Fig. 2.

Table 1. Experimental values of the heat capacity of minerals

Wollastonite		Quartz (Aktas)		Quartz (Nadyrbay)	
T, K	c, J/g·K	T, K	c, J/g·K	T, K	c, J/g·K
304.7	-0.108	305	-0.083	305	-0.146
361	0.31	361	0.038	361	0.072
449	0.414	449	0.093	450	0.128
539	0.376	539	0.095	539	0.143
627	0.405	627	0.148	627	0.208
713	0.333	713	0.121	713	0.237
798	0.293	798	0.125	797	0.166
881.7	0.317	882	0.204	882	0.238
964	0.332	964	0.259	964	0.288
1045.7	0.406	1046	0.328	1045.5	0.348
1126	0.471	1126	0.427	1125.8	0.412
1205	0.508	1205	0.44	1205	0.455
1284	0.542	1284	0.445	1284	0.504
1293	0.552	1293	0.449	1293	0.508

**Fig.2.** Dependence of the heat capacity of wollastonite $c = f(T)$ under heating process.

As can be seen from this graph, the heat capacity values within the temperature range from 304 K to 1293 K vary from 0.108 to 0.552 J/g·K. The specific heat capacity for the temperature condition of wollastonite within the temperature range of 1193-1293 K is calculated by the equation (1):

$$c = \frac{(dQ/dT)_p}{m} = \left(\frac{(6.14 - 5.216)}{(1293.82 - 1193.43)} \right) / 0.008 = 1156.3 \text{ J/kg} \cdot \text{K}.$$

The graph of the temperature dependence of the heat capacity obtained for quartz (Aktas) under thermal condition is shown in Figure 3. As can be seen from the graph, the heat capacity values within the temperature range from 305 K to 1293 K were -0.083-0.449 J/g·K.

The specific heat capacity of the quartz (Aktas) under thermal condition within the temperature range 1123-1293 K is calculated:

$$c = \frac{(dQ/dT)_p}{m} = \left(\frac{(6.16 - 5.45)}{(1293.91 - 1193.11)} \right) / 0.00936 = 752.88 \text{ J/kg} \cdot \text{K}.$$

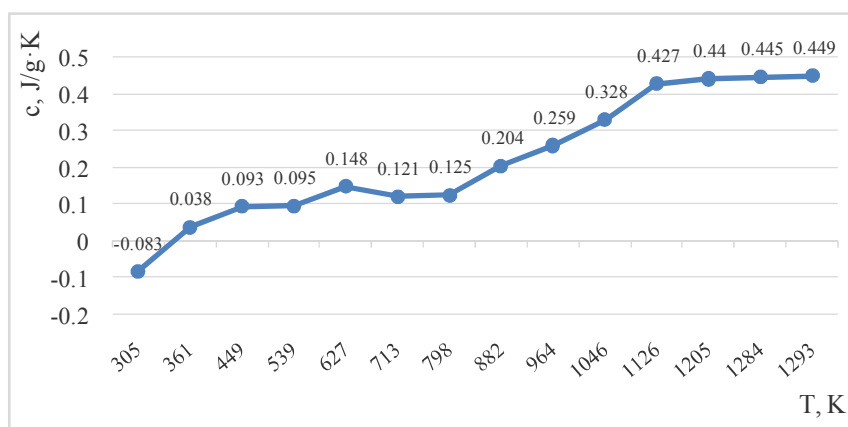


Fig.3. Graph of dependence $c = f(T)$, obtained for quartz (Aktas) under thermal condition

The graph of the temperature dependence of the heat capacity, obtained for quartz (Nadyrbay) under thermal condition, is shown in Figure 4.

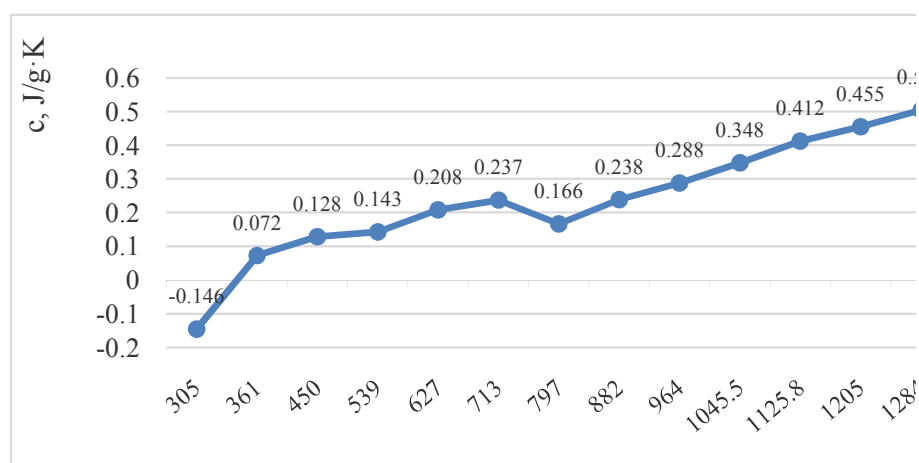


Fig.4. Graph of dependence $c = f(T)$, obtained for quartz (Nadyrbay) under thermal condition

Figure 4 shows that the heat capacity values within the temperature range from 305 K to 1293 K are 0.146 - 0.508 J/g·K, respectively. The heat capacity of quartz (Nadyrbay) under the thermal condition within the temperature range of 305 -1293 K is calculated by the equation (1):

$$c = \frac{(dQ/dT)_p}{m} = \left(\frac{(6.87 - 0.44)}{(1293.59 - 305.35)} \right) / 0.0096 = 770.7 \text{ J/kg} \cdot \text{K}.$$

After the experiments, the average values of the specific heat capacity with an error of 0.08% were determined and compared with theoretical values [7, 8], which are given in table 2.

Table 2. Comparison table

Mineral	Wollastonite, c, J/kg·K	Quartz (Aktas), c, J/kg·K	Quartz (Nadyrbay), c, J/kg·K
Experimental values	1156.3	752.88	770.7
Theoretical values	1100	692	692

It can be concluded from the table that the experimental values correspond to the theoretical ones. As can be seen from the temperature-dependent graph $c = f(T)$ of the heat capacity for wollastonite, quartz and dolomite under thermal condition, as the temperature rises, the heat capacity increases accordingly. The observation showed that the specific heat capacity of natural minerals depends on the temperature and concentration of the main components.

Conclusions

The specificity of the theory of thermal condition is that its basic conditions are generalized to the conditions for the existence of bodies of complex composition (systematic) and of any shape, while the usual theory is limited to the study of simple temperature fields or sometimes two-component bodies of a simple shape. Using DSC, the specific heat capacity of natural minerals with an error of 0.08% was determined. Specific heat capacity values are important material characteristics for their research and development as well as for quality control. The developed methods can be applied in information-measuring systems of thermophysical characteristics, in practice for thermophysical measurements, and in construction heat engineering.

REFERENCES

- 1 Sidortsova L.S. Current state and trends in the development of intellectual property in the field of physical and technical control of properties and state of rocks. *Mining Informational and Analytical Bulletin*, Moscow. 2009. No. 3, pp. 141 – 145.
- 2 Fokin V.M., Kovylin A.V., Chernyshov V.N. *Energy-efficient methods for determining the thermophysical properties of building materials and products*. Moscow, Publishing House "Spectr", 2011. 156 p.
- 3 Deveterikova M.I., Kozina L.N. *Laboratory practicum on general heat engineering*. Togliatti, 2007, 427 p.
- 4 Skryabin V.I. *A series of lectures on heat engineering*. Russian University of physics and technology. 2000, 82p.
- 5 State standard 55134-2012 (ISO 11357-1: 2009) *Plastics. Differential Scanning Calorimetry (DSC). Part 1. General principles*. Moscow, 2014, 27 p.
- 6 State standard 56754-2015 (ISO 11357-4: 2005) *Plastics. Differential Scanning Calorimetry (DSC). Part 4. Determination of specific heat capacity*. Moscow, 2017. 17 p.
- 7 Babichev A.P., Babushkina N.A., Bratkovsky A.M., et al. *Physical quantities. Reference guide*. (Ed. by Grigorieva I.S., Meilikhova E.Z.). Moscow, 1991, 1232 p.
- 8 Dobrynin V.M., Vendelstein B.Yu., Kozhevnikov D.A. *Petrophysics (Physics of rocks). Textbook for universities*. Moscow, Gubkin Russian State University of Oil and Gas, 2004, 368 p. [in Russian]

THE STUDY OF CURVES OF THE TRANSIENT CURRENT IN POLYTETRAFLUOROETHYLENE BY MEANS OF FOURIER ANALYSIS

Turdybekov K. M.¹, Turdybekov M.K.²

¹ E. A. Buketov Karaganda University, Karaganda, Kazakhstan, kalkantur@mail.ru

²Karaganda Technical University, Karaganda, Kazakhstan

Experimental transition current curves for polytetrafluoroethylene after exposure to high-energy ionizing radiation are obtained. The transient current curves in irradiated polytetrafluoroethylene are analyzed based on the discrete Fourier transform. It is shown that there is an intense maximum of dielectric absorption in the infra-low frequency region. This maximum is characterized by abnormally large values of the dielectric increment, permittivity, and the dielectric loss factor. It is concluded that the volume polarization of the irradiated polytetrafluoroethylene is uniform. The polarization observed in this frequency range is associated with the activation of migration of trapped charge carriers within microscopic regions.

Keywords: transient current curves, electrophysical properties, polytetrafluoroethylene, ionizing irradiation, Fourier analysis.

Introduction

The study of the effect of ionizing radiation on the electrical properties of solid dielectrics has become urgent due to the development of modern radiation technologies, the widespread use of insulating materials in nuclear and space research. Polymer materials used in spacecraft as part of screen-vacuum thermal insulation, electrical insulation of cables, thermal control coatings are exposed to the entire energy spectrum of ionizing radiation [1-3]. As an object of study, polytetrafluoroethylene (PTFE) is interesting on the one hand because it is a polymer of high practical significance, due to its unique complex of physics-chemical properties (chemical and biological resistance, excellent dielectric, antifriction and anti-adhesion properties, elasticity in the field of cryogenic temperatures). On the other hand, the fact that it reveals a number of electrical phenomena that have not yet found their explanation and are the subject of discussion [4-10].

The electrophysical properties of polytetrafluoroethylene (PTFE) after ionizing irradiation in the range of absorbed doses of 10^3 — 10^5 Gy degrees have a number of characteristic features. The values of the specific volume conductivity (σ_v) of PTFE at room temperature after γ - and electron irradiation increase by two or more orders of magnitude depending on the irradiation conditions and the physical state of the object under study (disks, film, thermal Modification) [1]. In the dielectric relaxation spectra of irradiated PTFE, intense maxima appear in the frequency range 10^2 - 10^4 Hz at $T = 400$ - 500 K (after irradiation in vacuum) and $T = 360$ - 400 K (after irradiation in air) [1]. Similar changes were observed for other fluorinated polymers, as well as for weak and nonpolar polymers [1] and were attributed to the type of slowly reversible changes, since they are characterized by annealing effects. For fluorinated polymers, both reversible and slowly reversible changes in the dielectric characteristics were associated with the accumulation of peroxide macroradicals. However, the estimation of the values of their effective dipole moment under the condition of the maximum possible concentration leads to unreasonable values ($\mu_{ef} \sim 10^{-28}$ C·m).

For the dipole-group and segmental mobility of most polymers at glass transition temperature $T_g < 400$ K, the specified time interval is sufficient to establish equilibrium polarization. However, after irradiation of polymers, a complete analysis of the transition current curves is necessary to determine the σ_v of the polymer matrix, since the relaxation times of the captured charges can be any, or, in any case, this time interval is not known in advance. To this end, this paper studies the transient current curves in the charging and discharging modes of irradiated PTFE in the frequency range: 10^{-4} — 10^1 Hz.

1. Samples and Research Methods

The study of the transition current of the technical film of polytetrafluoroethylene F4-IO with a thickness of 80 microns was carried out. Metal electrodes (measuring, high-voltage, and guard ring) were applied to the sample by thermal sputtering of silver in a vacuum. The transient current curves were recorded according to standard methods using measuring cells with a small parasitic capacitance, electrometric amplifiers (B7-30, U5-11, BK2-16). The time constant of the current measurements did not exceed 1 s, the RC - measured circuit did not exceed 10 s. The irradiation was carried out by gamma-rays with an energy of 1.2 MeV in air at the K-120 facility with the isotope ^{60}Co , the absorbed dose $D=5$ Mrad.

Transition current curves of a technical PTFE film with a thickness of 80 microns were studied. The analysis of transient current curves before and after gamma irradiation was performed using a block of standard Fourier analysis programs and original blocks of input-output programs and processing of Fourier analysis data implemented on a computer. Experimental points for calculations were taken after 1 s in the range 0-100 s, after 10 s in the range 100-1000 s, and after 100 s in the range 1000 - 10000 s.

The transition current curves after switching on (charging current) and off (discharging current) of the voltage source for the original PTFE are straightened in double logarithmic coordinates. The exponent of the time dependence of the discharge transient current density $j(t) \sim t^{-\eta}$ for the initial PTFE is $\eta = 1.6$ (Fig. 1). This result can be interpreted in terms of the Debye model for dipole-group mobility. If there is a Cole-Cole distribution of dipole relaxation times at $t > \tau$ (the dipole relaxation times are obviously much less than the characteristic measurement time) $(t/\tau)^{\alpha-2}$, [11], where τ is the relaxation time of the dipoles, and is the parameter of the relaxation time distribution. Based on the experimental dependences, we obtain the value $\alpha = 0.4$, which is typical for dipole-group losses.

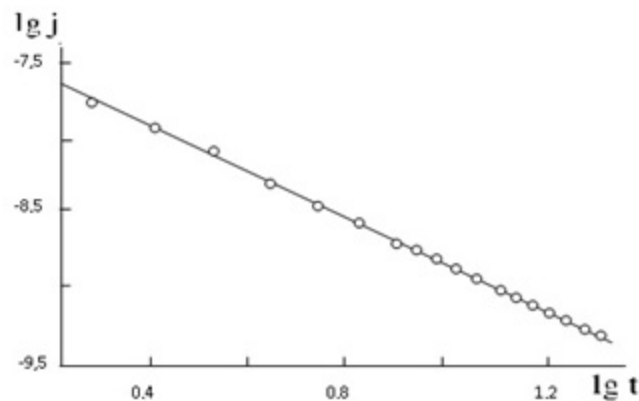


Fig.1. Kinetics of the discharge current density of an unirradiated PTFE film.

For the initial PTFE samples, the transient current density usually reached values less than 10^{-11} A / m² by the first minute, which corresponds to $\sigma_v < 10^{-17}$ Om⁻¹·m⁻¹ and is consistent with the literature data[11]. The dielectric increment can be determined from the discharge current curves:

$$\Delta\varepsilon = \int_0^{\infty} j(t)dt / \varepsilon_0 E_0 \cong 2 \cdot 10^{-2}, \quad (1)$$

where ε_0 is the dielectric constant, E_0 is the polarizing field strength, and t is the time in seconds.

The concentration of dipoles at normal values of $\mu_{ef} \sim 10^{-30}$ C · m will be

$$N = 3\varepsilon_0 kT \cdot \Delta\varepsilon / \mu^2 \cong 10^{25} \text{ m}^{-3}$$

and corresponds to the concentration of chemical and physical defects in PTFE. The occurrence of a polarizing current due to ionogenic impurities at room temperature is unlikely. These effects are usually observed at elevated temperatures. A completely different situation is observed for irradiated PTFE. The values of the transient current density in the initial section of the kinetic curve are three or more orders of magnitude higher than the corresponding values for the initial samples, and the current drop is observed up

to 10^4 s (Fig.2). Moreover, the discharge current of depolarization differs little in absolute value from the charging current.

The estimate of $\Delta\varepsilon$ by gives values for various PTFE films irradiated in air in the range of absorbed doses of 10^4 - 10^5 Gy, from 30 to 80. Obviously, such high values of $\Delta\varepsilon$ cannot be provided by dipole polarization. Even if their local concentration is high and the volume distribution is inhomogeneous, the recorded values of transient currents would need to be further increased, since the value of the integral in (1) is averaged over the volume.

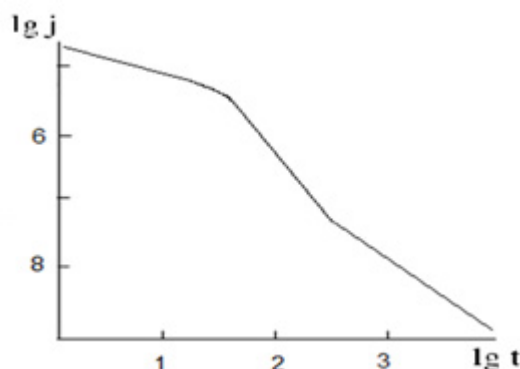


Fig.2. Kinetics of the discharge current density of a γ -irradiated PTFE film up to $D = 50$ kGy in air.

It follows from the above that the transition current curves up to 10^4 s are due to the establishment of polarization due to microscopic displacement of charges. In this regard, the increase in σ_v recorded after PTFE irradiation is mainly due to polarization currents, rather than stationary conductivity [1].

2. Discussion of results

Charge-discharge curves when recorded repeatedly on the same sample are well reproduced at room and low temperatures. Minor annealing effects begin to appear at 310 K and almost complete annealing, when the discharge curves differ slightly from the corresponding curves for the original samples, was observed after recording the charging curve for 10^4 s at 470 K. To determine the nature of polarization, we compared the discharge currents in two modes. In the first mode, the circuit during charging and discharging is shorted according to Fig.3a, in the second mode, the polarity of switching on during discharge changes to the opposite (Fig.3b). When an excess charge density is formed at one of the electrodes, the discharge currents in these switching schemes should differ markedly, just as it is observed when the excess charge injected into the surface layers of the dielectric is relaxed. The discharge curves observed by us were almost identical in both switching schemes. Thus, the polarization of irradiated PTFE can be characterized as uniform volumetric.

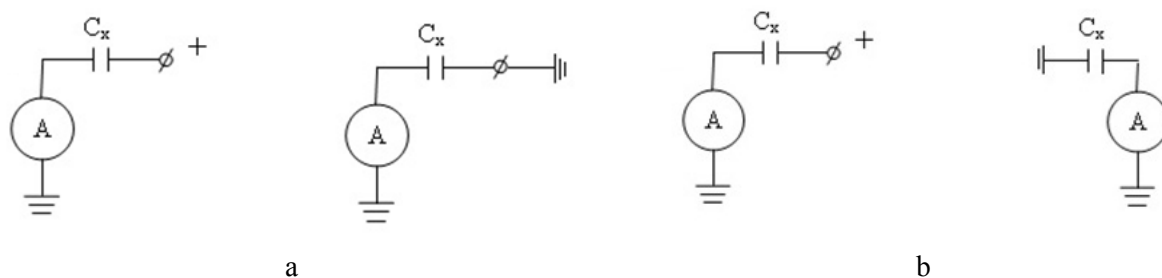


Fig.3. Scheme for measuring discharge currents without changing (a) and with a variable (b) polarity of switching on samples.

It is known that the time dependence of the transient current and the corresponding frequency dependence of the conductivity are related by the Fourier transform [11, 12]. In the presence of an exponential response $j(t) \sim \exp(-t/\tau)$, the variance of the transient current density is not observed, since the relative changes in the exponential function are the same at any time. For $j(t) \sim t^{-s}$, the relative changes in the transient current density decrease with increasing time, which corresponds to an increase in conductivity with increasing frequency. Experimental results indicate the existence of a frequency dependence of the conductivity of irradiated PTFE. Moreover, the presence of inflection points on the charge-discharge curves

clearly indicates the non-monotonic nature of this relationship. We have analyzed transient currents based on the discrete Fourier transform. It is known [11, 12] that

$$\varepsilon'(\omega) - i\varepsilon''(\omega) = \int_0^{\infty} j(t) \exp(-i\omega t) dt / \varepsilon_0 E_0,$$

then

$$\varepsilon'(\omega_i) = \int_0^{\infty} j(t) \cos \omega_i t dt / \varepsilon_0 E_0,$$

$$\varepsilon''(\omega_i) = \int_0^{\infty} j(t) \sin \omega_i t dt / \varepsilon_0 E_0,$$

where $\omega_i = 2\pi / t_i$

The dispersion curves ε' and ε'' obtained from the Fourier analysis of transient currents correspond to the infra-low frequency region 10^{-4} — 10^{-1} Hz. As can be seen in Fig. 4, the maximum of dielectric absorption is formed in the specified frequency range. The character of the curves ε' and ε'' fully corresponds to the Debye relations for the real and imaginary parts of the permittivity [12-14]. Moreover, the values of ε' , ε'' in the maximum and $\Delta\varepsilon$ are an order of magnitude or more higher than the possible values for dipole polarization processes. Lowering the temperature in full accordance with the Debye theory leads to a shift in the maximum towards lower frequencies. The activation energy found from the displacement of the peaks in Arrhenius coordinates was 84 kJ/mol. The values of the pre-exponential factor $\nu_0 = 6 \cdot 10^{13}$ Hz significantly exceed the corresponding values for the dipole group ($\nu_0 \cong 10^{13}$ Hz) and segmental ($\nu_0 \cong 10^{12}$ Hz) mobility in polymers, which in turn is consistent with the activation mechanism of migration of captured charge carriers.

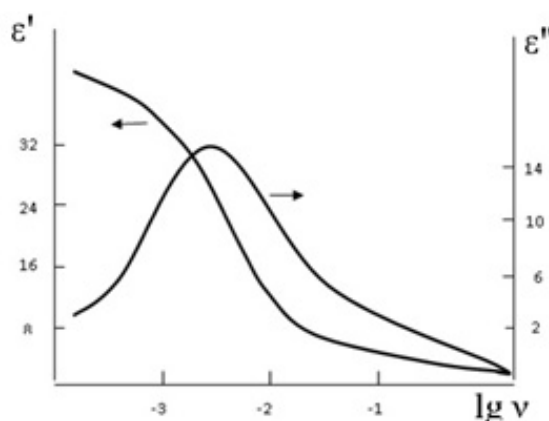


Fig.4. Frequency dependence of the permittivity ε' and the dielectric loss factor ε'' for PTFE after gamma irradiation in air; D = 50 kGy.

Thus, the analysis of transient currents in the frequency range 10^{-4} — 10^{-1} Hz shows that the polarization effects observed for irradiated PTFE can be interpreted by thermal activation of charge carriers both with the participation (near 400 K) and without the participation (at $T < 300$ K) of the polymer matrix and their displacement within microscopic regions not related to conductivity. However, it remains unclear the question about the nature of these areas. It could be assumed that the charges are mainly localized on the chemical and physical defects of the structure. However, thermal modification of the samples does not lead to qualitative changes in the spectra, and the corresponding electrophysical parameters remain anomalous. In addition, similar patterns were observed on other fluorinated polymers (and even polyolefins) with significantly different nature of structural traps.

The latter fact clearly indicates the more General nature of the observed polarization phenomena. It can be assumed that the observed effects are related to the inhomogeneous spatial distribution of the ionization regions. These regions can be spurs, blobs, and short tracks formed during the interaction of secondary electrons with matter. The lifetimes of these micro-regions may be quite large, since the dispersion transport

of charge carriers in them occurs under conditions of strong scattering to deep radiation traps, while the times of dielectric relaxation of the polymer matrix are $\tau = 10^6 - 10^8$ s.

Conclusion

In general, changes in the dielectric parameters are anomalous and are observed both directly during the exposure to radiation, and after its termination for a long time. Several different explanations for the radiation-induced effects of the electric polarization of polytetrafluoroethylene have been put forward in the literature, but a single view on this issue has not yet been developed.

In this paper, we study the volume electric polarization in polytetrafluoroethylene (-CF₂-CF₂-) n exposed to high-energy ionizing radiation. The small difference in the absolute value of the charge-discharge currents suggests that there is no significant influence of the near-electrode polarization on the observed process. Since the polarization curves in both inclusion schemes practically did not differ, the polarization of the irradiated polytetrafluoroethylene can be characterized as uniform volumetric. The curves of the polarization and depolarization currents are reproduced repeatedly with an error not exceeding 10%.

A Fourier analysis of the time dependences of the polarization current is performed. The main feature of the obtained results is the abnormally high values of ϵ' and ϵ'' in the region of the relaxation maximum, which are not typical for elementary dipoles. The analysis shows the existence of an intense maximum of dielectric absorption in the region of infra-low frequencies with abnormally large values of the dielectric increment, permittivity, and the dielectric loss factor. Polarization phenomena in the infra-low frequency region are associated with activation of migration of trapped charge carriers within microscopic regions. These areas are not connected by conductivity. Such areas can be spurs, blobs, and short tracks formed during the interaction of secondary electrons with matter.

REFERENCES

1. Milinchuk V. K. Radiation resistance of organic materials. Moscow, Energoatomizdat, 1986, 171p. [in Russian].
2. Khatipov S.A. Radiation electrical conductivity of polymers. Chapter 1.12 of the collection «*Model of space: The impact of the space environment on the materials and equipment of spacecraft*». Moscow, 2007, pp. 361 – 376. [in Russian].
3. Khatipov S.A., Tsvelev V.M., Alekseev S.V. Radiation resistance of polymers in the conditions of outer space. Chapter 1.15 of the collection «*Model of space: The impact of the space environment on the materials and equipment of spacecraft*». Moscow, 2007, pp. 414-436. [in Russian].
4. Obvintsev A.Yu. and others. The effect of gamma radiation on the surface and bulk properties of polytetrafluoroethylene. *The surface. X-ray, synchrotron, and neutron studies*. 2017, No. 9, pp. 52-60. [in Russian]
5. Zhutaeva Yu.R., Khatipov S.A. Maxwell-Wagner polarization in polytetrafluoroethylene subjected to the impact of ionizing radiation. *Proc. of the Intern. Symposium «Physics and Chemistry of processes, oriented toward development of new high technologies, materials and equipment»*. Chernogolovka, 2007, pp. 317-322.
6. Tyutnev A. P., Arkhipov V. I., Nikitenko V. R., Sadovnichy D. N. On the nature of non-Langevin recombination of charge carriers in polymers. *Chemical physics*. 1996, vol. 15, No. 3, pp. 91-99. [in Russian].
7. Malysheva I.A., Burmistrov S.E., Gavrilova N.D. Dielectric spectroscopy of sulfonated polytetrafluoroethylene in the swollen state. *High-molecular compounds*. 2005, B, Vol.47, No. 8, pp. 1563-1568. [in Russian].
8. Klein R.J., Cole S.M., Belcher M.E., et al. Radiation tolerance in polymeric dielectrics by small molecule doping. Part II: Thermodynamic and kinetic parameters. *POLYMER*, 2008, Vol. 49, p.5549-5563.
9. Khatipov S. A., Turdybekov K. M., Edrisov A. T., Milinchuk V. K. Electrification of polymer films under the influence of vacuum ultraviolet light. *High-energy chemistry*. 1995, Vol. 29, No.3, pp. 184-186. [in Russian].
10. Sergeeva A. E. Polarization and spatial charge in ferroelectric polymers. Odessa: TES, 2014, 347 p. [in Russian].
11. Lushcheikin G. A. Methods for studying the electrical properties of polymers. Moscow: Khimiya, 1988, 160 p. [in Russian].
12. Sazhin B. I. *Electrical properties of polymers*. Leningrad, Chemistry, 1986, 224 p. [in Russian].
13. Lushcheikin G. A. *Polymer electrets*. Moscow, 2008, 180 p. [in Russian].
14. Sessler G. M. *Electrets*. Springer-Verlag, Berlin. 2003, 437 p.

SUMMARIES	ТҮСІНІКТЕМЕЛЕР	АННОТАЦИИ
<p><i>Мальшев А.В., Лысенко Е.Н., Шевелева Е.А., Суржикова О.А., Арынгазин А.К.</i> Радиациялық және радиациялы-термиялық жағдайларда қақтау кезінде ферриттердің магниттік қасиеттері мен микроқұрылымының өзарабайланысы. Магниттік қасиеттері мен микроқұрылымның корреляциясын зерттеу радиациялық және радиациялы-термиялық режимдерінде қақталған литий алмастырылған феррит үлгілерінде жүргізілген. Радиациялық-термиялық қақтау дайындамаларды (1.5-2.0) МэВ энергиялы электрондардың импульсті шоғымен, импульстегі шоктың (0.5 – 0.9) А тогы, сәулелендіру импульсінің ұзақтығы – 500 мкс, импульстердің жүру жиілігі – (5-50) Гц, дайындамаларды қыздыру жылдамдығы - 1000°С/мин кезінде жүргізілген. Термопештердегі қақтау (Т-қақтау) алдын ала қыздырылған камералық электр пешінде жүргізілді. Жұмыста магниттік индукцияның ферриттің түйіршіктілігінен тәуелсіздігі көрсетілген. Бұл жағдайда коэрцитивті күш түйіршіктің өлшеміне кері пропорционал және феррит үлгілерінің ішкі түйіршікті кеуектілігіне байланысты. Термиялық қақтаумен салыстырғанда радиациялы-термиялық қақтау өсіп келе жатқан түйіршіктердің түйіршік-аралық қуыстардың қармауына әкелмейді және ішкі түйіршік кеуектердің коагуляциясына ықпал етеді.</p>	<p><i>Мальшев А.В., Лысенко Е.Н., Шевелева Е.А., Суржикова О.А., Арынгазин А.К.</i> Взаимосвязь магнитных свойств и микроструктуры ферритов при спекании в радиационных и радиационно-термических условиях. Исследования корреляции магнитных свойств и микроструктуры проводились на образцах литий-замещенного феррита, спеченных в радиационном и радиационно-термическом режимах. Радиационно-термическое спекание осуществлялось облучением заготовок импульсным пучком электронов с энергией (1.5-2.0) МэВ, токе пучка в импульсе (0.5-0.9) А, длительности импульса облучения – 500 мкс, частоте следования импульсов – (5-50) Гц, скорости разогрева заготовок – 1000°С/мин. Спекание в термопечах (Т-спекание) производилось в предварительно разогретой камерной электрической печи. В работе показана независимость магнитной индукции от зернистости феррита. При этом коэрцитивная сила обратно пропорциональна размеру зерна и зависит от внутризеренной пористости ферритовых образцов. Радиационно-термическое спекание, в отличие от термического спекания, не приводит к захвату межзеренных пустот растущими зёрнами и способствует коагуляции внутризеренных пор.</p>	<p><i>Мальшев А.В., Лысенко Е.Н., Шевелева Е.А., Суржикова О.А., Арынгазин А.К.</i> Радиациялық және радиациялы-термиялық жағдайларда қақтау кезінде ферриттердің магниттік қасиеттері мен микроқұрылымының өзарабайланысы. Магниттік қасиеттері мен микроқұрылымның корреляциясын зерттеу радиациялық және радиациялы-термиялық режимдерінде қақталған литий алмастырылған феррит үлгілерінде жүргізілген. Радиациялық-термиялық қақтау дайындамаларды (1.5-2.0) МэВ энергиялы электрондардың импульсті шоғымен, импульстегі шоктың (0.5 – 0.9) А тогы, сәулелендіру импульсінің ұзақтығы – 500 мкс, импульстердің жүру жиілігі – (5-50) Гц, дайындамаларды қыздыру жылдамдығы - 1000°С/мин кезінде жүргізілген. Термопештердегі қақтау (Т-қақтау) алдын ала қыздырылған камералық электр пешінде жүргізілді. Жұмыста магниттік индукцияның ферриттің түйіршіктілігінен тәуелсіздігі көрсетілген. Бұл жағдайда коэрцитивті күш түйіршіктің өлшеміне кері пропорционал және феррит үлгілерінің ішкі түйіршікті кеуектілігіне байланысты. Термиялық қақтаумен салыстырғанда радиациялы-термиялық қақтау өсіп келе жатқан түйіршіктердің түйіршік-аралық қуыстардың қармауына әкелмейді және ішкі түйіршік кеуектердің коагуляциясына ықпал етеді.</p>
<p><i>Юров В.М., Гончаренко В.И., Олешко В.С.</i> Кубтық көлемдік-центрленген кристалдық торлардың беткі анизотропиясы. Шебзухов және Арефьева жұмысында металдардың беттік энергиясының анизотропиясын электронды-статистикалық есептеу әдісімен металдан электрондардың шығу жұмысы үшін бағалау әдісі анықталған. Бокаревтің жұмысында монокристалдардың беттік энергиясының анизотропиясы кристалдардың координациялық балку моделінен есептелген. Біз ұсынған эмпирикалық модельде анизотропия ғана емес, сонымен қатар Li→Cs жүйесі үшін 3-тен 27 нм-ге дейінгі металдың беткі қабатының қалыңдығы есептелген. Бұл қабат анизотропты және орта есеппен 9 (Li) - ден 27-ге дейін (Cs) моноқабаттарға ие. Жалпы алғанда, өлшемді эффектілер $R(II) \approx 9R = R_{\infty}$ ара-қашықтыққа дейін байқалады, бұл кезде көлемдік фаза басталады, ал калийден бастап, Слейтер бойынша наноқұрылымдар үшін тән 100 нм шегінен асады. Жұмыста электрондардың шығу жұмысы металдың беттік энергиясының өзгеруімен пропорционалды түрде өзгеретіні көрсетілген. Бұл біз жасаған құрылғыны металл бетінің күйін және оның анизотропиясын өлшеу үшін қолдануға болатындығын білдіреді.</p>	<p><i>Юров В.М., Гончаренко В.И., Олешко В.С.</i> Анизотропия поверхности кубических объемно-центрированных кристаллических решеток. В работе Шебзуховой и Арефьевой методом электронно-статистического расчета анизотропии поверхностной энергии металлов определен метод оценки для работы выхода электронов из металла. В работе Бокарева анизотропия поверхностной энергии монокристаллов рассчитана из модели координационного плавления кристаллов. В предложенной нами эмпирической модели рассчитывается не только анизотропия, но и толщина поверхностного слоя металла, которая для системы Li→Cs составляет от 3 до 27 нм. Этот слой анизотропен и содержит в среднем от 9 (Li) до 27 монослоев (Cs). В целом же размерные эффекты наблюдаются до расстояний $R(II) \approx 9R = R_{\infty}$, где начинается объемная фаза, которая, начиная с калия, превышает предел 100 нм, характерный для наноструктур по Слейтеру. В работе показано, что работа выхода электронов пропорционально изменяется с изменением поверхностной энергии металла. Это значит, что разработанный нами прибор можно использовать для измерения состояния поверхности металла и его анизотропии.</p>	<p><i>Юров В.М., Гончаренко В.И., Олешко В.С.</i> Кубтық көлемдік-центрленген кристалдық торлардың беткі анизотропиясы. Шебзухов және Арефьева жұмысында металдардың беттік энергиясының анизотропиясын электронды-статистикалық есептеу әдісімен металдан электрондардың шығу жұмысы үшін бағалау әдісі анықталған. Бокаревтің жұмысында монокристалдардың беттік энергиясының анизотропиясы кристалдардың координациялық балку моделінен есептелген. Біз ұсынған эмпирикалық модельде анизотропия ғана емес, сонымен қатар Li→Cs жүйесі үшін 3-тен 27 нм-ге дейінгі металдың беткі қабатының қалыңдығы есептелген. Бұл қабат анизотропты және орта есеппен 9 (Li) - ден 27-ге дейін (Cs) моноқабаттарға ие. Жалпы алғанда, өлшемді эффектілер $R(II) \approx 9R = R_{\infty}$ ара-қашықтыққа дейін байқалады, бұл кезде көлемдік фаза басталады, ал калийден бастап, Слейтер бойынша наноқұрылымдар үшін тән 100 нм шегінен асады. Жұмыста электрондардың шығу жұмысы металдың беттік энергиясының өзгеруімен пропорционалды түрде өзгеретіні көрсетілген. Бұл біз жасаған құрылғыны металл бетінің күйін және оның анизотропиясын өлшеу үшін қолдануға болатындығын білдіреді.</p>

Кручинин Н.Ю., Кучеренко М.Г.

Көлденең аса жоғары жиілікті электр өрісінде металл наносым бетіндегі полиамфолиттердің конформациялық құрылымының қайта құрылуы.

Молекулалық динамика әдісін қолдуымен алтын наносымның бетіне адсорбцияланған полиамфолиттердің конформациялық құрылымын оның полярлығының уақыт өтуімен аса жоғары жиілікпен көлденең бағытта периодты түрде өзгеруімен қайта құрылуы зерттелген. Полипептид атомдары тығыздығының радиалды таралуы, сондай-ақ оның наносым бетіндегі бұрыштық таралуы есептелген. Жоғары температураларда адсорбцияланған полиамфолит полипептидінің конформациялық құрылымының уақытша ауытқулары байқалды. Бұл жағдайда наносым полярлығының өзгеру периодының жартысында макротізбектің конформациясы наносымның тығыз қаптаудан конформациялық құрылымға өзгерді, онда макромолекулалық жиек наносымның диполь моменті бойымен көлденең бағытта созылды. Наносымның дипольдік моментінің төмен температурасы мен мәні кезінде адсорбцияланған полиамфолиттің жиектерінің бөртуі байқалды, оның буындарының көп бөлігі наносымның диполь моментінің бағытына перпендикуляр және оның осі арқылы өтетін жазықтыққа қатысты бір жағына жылжыды. Төмен температурада және наносымның диполь моментінің жоғары мәндерінде наносым бетінен полиамфолит полипептидінің десорбциясы орын алды. Сыртқы өрістегі ұйытқу теориясы түрінде полиамфолиттік гаусс тізбегінің конформациялық қайта құрылуының аналитикалық моделі ұсынылған.

Кручинин Н.Ю., Кучеренко М.Г.

Перестройка конформационной структуры полиамфолитов на поверхности металлического нанопровода в поперечном сверхвысокочастотном электрическом поле.

С использованием метода молекулярной динамики исследована перестройка конформационной структуры адсорбированных на поверхности золотого нанопровода полиамфолитов с периодическим изменением во времени его полярности в поперечном направлении со сверхвысокой частотой. Рассчитаны радиальные распределения плотности атомов полипептида, а также его угловые распределения на поверхности нанопровода. При высокой температуре наблюдались временные колебания конформационной структуры адсорбированного полиамфолитного полипептида. В этом случае за половину периода изменения полярности нанопровода конформация макроцепи изменялась от плотного обволакивания нанопровода к конформационной структуре, при которой макромолекулярная опушка вытянута в поперечном направлении вдоль дипольного момента нанопровода. При низких температуре и значении дипольного момента нанопровода наблюдалось набухание опушки адсорбированного полиамфолита со смещением большей части его звеньев на одну сторону по отношению к плоскости, перпендикулярной направлению дипольного момента нанопровода и проходящей через его ось. При низкой температуре и высоких значениях дипольного момента нанопровода происходила десорбция полиамфолитного полипептида с поверхности нанопровода. Представлена аналитическая модель конформационных перестроек полиамфолитной гауссовой цепи в виде теории возмущений по внешнему полю.

Қасенов Б.Қ., Қасенова Ш.Б., Сағынтаева Ж.И., Нұхұлы А., Тұртұбаева М.О., Бектұрғанов Ж.С., Зейниденов А.К., Қуанышбеков Е.Е., Исабаева М.А.

Құрамында сілті металдары бар жаңа нанокұрылымды мыс-мырыш манганиттерін синтезі мен рентгенографиялық тұрғыдан зерттеу.

Берілген жұмыстың мақсаты - лантан мен сілтілі металдардың жаңа нанокұрылымды мыс-мырыш манганиттерін синтездеу. 800-1200 °С аралығында лантан (III), мыс (II), мырыш (II), марганец (III) оксидтерінен және литий, натрий және калий карбонаттарынан керамикалық технология әдісімен $LaMe^I_2CuZnMnO_6$ құрамды поликристалды мыс-мырышты манганиттері синтезделінді, мұндағы $Me^I - Li, Na, K$. «ММ301» маркалы «Retsch» (Германия) компаниясының тербелмелі диірменінде синтезделген поликристалды қосылыстарды ұсақтау арқылы олардың нанокұрылымды бөлшектері алынды. Нанокұрылымды лантан және сілтілі металдардың мыс-мырышты манганиттерінің рентгенограммаларын индицирлеу арқылы олардың кубтық сингонияда кристалданатыны анықталды. Олардың тор көрсеткіштері анықталды. Сілтілік металдардың иондық радиустарынан тор көрсеткіштерінің өзгеруінде заңдылық байқалады.

Қасенов Б.К., Қасенова Ш.Б., Сағынтаева Ж.И., Нухұлы А., Тұртұбаева М.О., Бектұрғанов Ж.С., Зейниденов А.К., Қуанышбеков Е.Е., Исабаева М.А.

Синтез и рентгенографическое исследование новых наноструктурированных медно-цинковых манганитов содержащих щелочные металлы.

Цель данной работы – синтез новых наноструктурированных медно-цинковых манганитов лантана и щелочных металлов. Методом керамической технологии из оксидов лантана (III), меди (II), цинка (II), марганца (III) и карбонатов лития, натрия и калия в интервале 800-1200 °С синтезированы

поликристаллические медно-цинковые манганиты состава $\text{LaMe}^1_2\text{CuZnMnO}_6$, где Me^1 – Li, Na, K. Измельчением синтезированных поликристаллических соединений на вибрационной мельнице компании «Retsch» (Германия) марки «ММ301» получены их наноструктурированные частицы. Индексированием рентгенограмм наноструктурированных медно-цинковых манганитов лантана и щелочных металлов установлено, что, они кристаллизуются в кубической сингонии. Определены их параметры решеток. Наблюдается закономерность в изменении параметров решетки от ионных радиусов щелочных металлов.

Леонов А.П., Усачева Т.В., Ляпунов Д.Ю., Воронина Н.А., Гальцева О.В., Розачев А.А.

Асинхронды қозғалтқыштарды модернизациялау үшін полимерлі электр окшаулау жүйелерінің жылу төзімділігін арттыру.

Шағын массалық өлшемдерді қамтамасыз етуімен бірге асинхронды қозғалтқыштардың жоғары қуатын, үнемділігін және сенімділігін қамтамасыз ету мәселесі қазіргі таңда маңызды рөл атқарады. Асинхронды қозғалтқыштардың қуатын арттыру кезінде массагабариттік көрсеткіштерінің төмендеуін шектейтін факторлардың бірі - окшаулау жүйесінің істен шығуы болып табылады. Сондықтан электр окшаулау жүйелерінің қыздыруға төзімділік класының жоғарылауын ескере отырып, асинхронды қозғалтқышты жобалау кезінде ойықты толтыру мәселелерін зерттеу қажет. Жұмыстың мақсаты – массагабариттік көрсеткіштерді төмендету және орауыш материалының мүмкін болатын үнемдеуін бағалау үшін орташа қуатты асинхронды қозғалтқышты модернизациялау үшін жоғары температураға төзімді полимерлі электр окшаулау жүйесін жасау болып табылады. Жұмыс барысында статор ойығының толтырылуына талдау жүргізілген, заманауи өткізгіш және окшаулағыш материалдар таңдалды, әр түрлі қыздыруға төзімділік кластарына арналған орташа қуатты асинхронды қозғалтқыштарына есептеулері жүргізілген, ұсынылған электр окшаулау жүйесі негізделген. Алынған нәтижелерді талдау сапаның белгілі бір деңгейін төмендетпестен асинхронды қозғалтқыштардың орауыш материалын үнемдеу үшін полимерлі электр окшаулау жүйелерінің қыздыруға төзімділігін арттыру мүмкіндіктерінің болуын көрсеткен.

Леонов А.П., Усачева Т.В., Ляпунов Д.Ю., Воронина Н.А., Гальцева О.В., Розачев А.А.

Повышение нагревостойкости полимерных электроизоляционных систем для модернизации асинхронных двигателей.

Проблема обеспечения высокой мощности, экономичности и надежности эксплуатации асинхронных двигателей при обеспечении малых массогабаритных показателей играет все более важную роль. Одним из факторов, ограничивающих снижение массогабаритных показателей при наращивании мощностей асинхронных двигателей является выход изоляционной системы из строя. Исходя из этого возникает необходимость проработать вопросы заполнения паза при проектировании асинхронного двигателя, с учетом повышения класса нагревостойкости электроизоляционных систем. Цель работы – разработать полимерную электроизоляционную систему повышенной нагревостойкости для модернизации асинхронного двигателя средней мощности с целью снижения массогабаритных показателей и оценить возможную экономию обмоточного материала. В ходе работы проведен анализ заполнения паза статора, выбраны современные проводниковые и изоляционные материалы, выполнены расчеты асинхронного двигателя средней мощности на разные классы нагревостойкости, обоснована предложенная электроизоляционная система. Анализ полученных результатов показывает наличие возможностей повышения нагревостойкости полимерных электроизоляционных систем с целью экономии обмоточного материала асинхронных двигателей без снижения заданного уровня качества.

Трубицын А.А., Грачев Е.Ю., Козлов Е.А., Шугаева Т.Ж.

Жоғары қуатты микротөғысты рентген түтігін жасау.

Берілген жұмыста атыс типті микротөғысты рентген түтігінің қуатын арттырудың жаңа әдісі ұсынылған және зерттелген. Ұсынылған әдіс жылу құбырын түтіктің аноды ретінде пайдалану идеясына негізделген. Электронды сәуленің диаметріне және вольфрам нысанасының қалыңдығына байланысты осындай анодта шашыраған максималды қуат үшін теориялық өрнек алынған. Ұсынылған түтіктің қуаты стандартты құрамдас анодтарға ие түтіктердің қуатынан бірнеше есе асып түсетіні көрсетілген. Электрстатикалық төғысталуға ие түтіктің электронды-оптикалық сұлбасы ұсынылып, талданған.

Трубицын А.А., Грачев Е.Ю., Козлов Е.А., Шугаева Т.Ж.

Разработка микрофокусной рентгеновской трубки высокой мощности.

В настоящей работе предлагается и исследуется новый способ повышения мощности микрофокусной рентгеновской трубки прострельного типа. В основе предлагаемого способа лежит идея использования тепловой трубы в качестве анода трубки. Получено теоретическое выражение максимальной мощности, рассеиваемой на таком аноде, в зависимости от диаметра электронного луча и толщины вольфрамовой мишени. Показано, что мощность предлагаемой трубки может многократно превосходить мощность трубок со стандартными составными анодами. Предложена и проанализирована электронно-оптическая схема трубки с электростатической фокусировкой.

Танашева Н.К., Бахтыбекова А.Р., Сакипова С.Е., Миньков Л.Л., Шуюшбаева Н.Н., Касимов А.Р.

Айналмалы цилиндрлік қалақшалармен жел дөңгелегі айналасындағы ағынды сандық модельдеу.

Мақалада ANSYS бағдарламалық кешенінің негізінде айналмалы цилиндр түріндегі қалақшаларға ие жел дөңгелегі айналасындағы ағынның сандық модельдеудің нәтижелері талқыланады. Айналмалы цилиндрлік қалақшаларына ие жел энергетикалық қондырғының дәстүрлі қалақшалы қондырғылармен салыстырғанда артықшылығы (2-3) м/с желдің жылдамдығы кезінде іске қосылу және электр энергияны өндіруді бастау мүмкіндігі болып табылады. Айналмалы жүйеде үш өлшемді Навье-Стокс тендеулеріне негізделген математикалық модель жасалды. Сәйкесті шекаралық шарттар тұжырымдалған. Рейнольдстың жоғары сандары кезінде пайда болатын турбулентті құйындылары бар жылдамдық өрісінің аймақтары көрсетілген. Кіретін ауа ағынының әр түрлі жылдамдықтары кезінде күштер моментінің шамасына жел дөңгелегінің айналуының бұрыштық жылдамдығының әсер ету дәрежесі анықталды.

Танашева Н.К., Бахтыбекова А.Р., Сакипова С.Е., Миньков Л.Л., Шуюшбаева Н.Н., Касимов А.Р.

Численное моделирование обтекания ветроколеса с вращающимися цилиндрическими лопастями.

В статье обсуждаются результаты численного моделирования обтекания ветроколеса с лопастями в виде вращающихся цилиндров на основе программного комплекса ANSYS. Преимуществом ветроэнергетической установки с вращающимися цилиндрическими лопастями по сравнению с традиционными лопастными установками является возможность запуска и начала выработки электроэнергии при скорости ветра (2-3) м/с. Разработана математическая модель на основе трехмерных уравнений Навье-Стокса во вращающейся системе. Сформулированы соответствующие граничные условия. Показаны области поля скорости с турбулентными вихрями, которые образуются при больших числах Рейнольдса. Определена степень влияния угловой скорости вращения ветроколеса на величину момента сил при различных скоростях набегающего воздушного потока.

Безродный М.К., Ословский С.А.

Ғимаратты жылыту және желдету үшін ауа және жердегі жылу сорғыларының комбинациясын пайдалану тиімділігін талдау.

Мақалада жылу сорғылары үшін ең көп таралған екі жылу көздерінің – жер пен атмосфералық ауаның комбинациясын қолдану тиімділігі зерттелген. Мұндай жүйенің ерекшелігі - жер және ауа жылу сорғыларының су арқылы тізбектей қосылуы болып табылады. Жүйенің жылу және материалдық баланстарының теңдеулер жүйесіне негізделген ұсынылған жүйенің математикалық моделі жасалды. Талдау нәтижесі теңдеулер жүйесі болып табылады, оның шешімі энергия тиімділігінің екі негізгі сипаттамасын, атап айтқанда, жердің жылу алмастырғышының салыстырмалы жылу жүктемесін және желдету шығарындыларының жылу пайдалану тереңдігіне байланысты жүйенің жетегіне арналған сыртқы жұмыстың жалпы шығындарын зерттеуге мүмкіндік берді. Энергия мен инвестициялар үшін екі жылу сорғысына ие жылу және желдету жүйесін пайдаланудан оң нәтижеге ауа және жер үсті жылу сорғылары үшін түрлендіру коэффициенттерінің теңдігі шартына сәйкес келетін желдету шығарындыларын пайдалану тереңдігінде қол жеткізуге болатындығы көрсетілген.

Безродный М.К., Ословский С.А.

Анализ эффективности использования комбинации воздушного и грунтового тепловых насосов для отопления и вентиляции здания.

В статье исследуется эффективность использования комбинации двух наиболее распространенных источников тепла для тепловых насосов - грунта и атмосферного воздуха. Особенностью такой системы является последовательное подключение по воде грунтового и воздушного тепловых насосов. Разработана математическая модель предложенной системы, основанная на системе уравнений теплового и материального балансов системы. Результатом анализа является система уравнений, решение которой позволило изучить две основные характеристики энергоэффективности, а именно относительную тепловую нагрузку грунтового теплообменника и удельные общие затраты внешней работы для привода системы в зависимости от глубины использования тепла вентиляционных выбросов. Показано, что положительный эффект от использования системы отопления и вентиляции с двумя тепловыми насосами, как по энергии, так и по инвестициям, может быть достигнут при глубине использования вентиляционных выбросов, соответствующей условию равенства коэффициентов преобразования для воздушных и наземных тепловых насосов.

Дүйсенов Қ.М., Сақыпов Қ.Е., Шаяхметова Р.Т., Недугов И.А., Айтмағамбетова М.Б., Есімсейіт А.Қ.

Акустикалық кавитацияның судың физикалық және химиялық қасиеттеріне әсері.

Мақалада ультрадыбыстық кавитацияның әсерінен судың иондық құрамының өзгеруін эксперименттік зерттеу нәтижелері келтірілген. Акустикалық сәулеленудің судың физика-химиялық қасиеттеріне әсері 20 Гц - 50 кГц жиілік диапазонында зерттелді. Ультрадыбыстық диапазон металл іздері аймағында

концентрацияның жоғарылауына әкелетіні және судың рН өзгеруіне әсер ететіні көрсетілген. Кавитацияның әсер ету механизмі судың құрылымдық сипаттамаларының өзгеруіне әкеледі. Ультрадыбыстық кавитацияның дәлелденген әсерінің бірі әртүрлі қосымшалар үшін пайдаланылуы мүмкіндігі көрсетілген.

Дюсенов К.М., Сакипов К.Е., Шаяхметова Р.Т., Недугов И.А., Айтмагамбетова М.Б., Есимсеит А.К.

Влияние акустической кавитации на физико-химические свойства воды.

В статье представлены результаты экспериментального исследования изменения ионного состава воды под действием ультразвуковой кавитации. Влияние акустического излучения на физико-химические свойства воды исследовалось в диапазоне частот 20 Гц - 50 кГц. Показано, что ультразвуковой диапазон приводит к увеличению концентрации в области следов металла и влияет на изменение рН воды. Механизм воздействия кавитации приводит к изменению структурных характеристик воды. Показано, что один из проявленных эффектов ультразвуковой кавитации может быть использован для различных приложений.

Шаймерденова К.М., Стоев М., Секербаева Г.К., Булкаирова Г.А., Оспанова Д.А., Тусыпбаева А., Рахманқызы А.

Әр түрлі қыздыру параметрлеріндегі минералдардың жылуфизикалық сипаттамаларын зерттеу.

Жылу және электр оқшаулағыш материалдар өндірісінде табиғи минералдарды зерттеу олардың жылуфизикалық сипаттамаларын анықтау барысында тәжірибелік қызығушылық тудырады. Минералдардың жылу сыйымдылығының өзгеру заңдылықтары өндіріс және пайдалану жағдайында қыздырылған кезде ерекше назар аударылады. Зерттеу нысандары ретінде волластонит және кварц табиғи минералдары қарастырылды. Бұл минералдардың жылу сыйымдылығы калориметриялық әдіспен 1600°C температураға дейін қыздырылған үш өлшемді сенсорлы және газ ағынын автоматты түрде басқаруға арналған панельді аппараттарында өлшенді. Тәжірибе нәтижелері бойынша минералдар үлгілерінің жылу сыйымдылығының температураға тәуелділік графиктері құрылды.

Шаймерденова К.М., Стоев М., Секербаева Г.К., Булкаирова Г.А., Оспанова Д.А., Тусыпбаева А., Рахманқызы А.

Исследование теплофизических характеристик минералов при различных параметрах нагревания.

Изучение природных минералов при производстве тепло- и электроизоляционных материалов представляет особый практический интерес для изучения их теплофизических характеристик. Особый интерес представляет закономерности изменения теплоемкость минералов при нагревании в производственных и эксплуатационных условиях. В качестве объекта исследований рассматривались природные минералы волластонита и кварца. Теплоемкость данных минералов измерялась в аппарате с трехмерном сенсором и панелью автоматического управления потоками газов, при нагреве до температуры 1600 °С калориметрическим методом. По экспериментальным результатам построены графики зависимости теплоемкости образцов минералов от температуры.

Тұрдыбеков Қ.М., Тұрдыбеков М.Қ

Фурье-талдау бағдарламаларын пайдалануымен политетрафторэтилендегі өтпелі ток қисықтарын зерттеу.

Жоғары энергиялы иондаушы сәулелену әсерінен кейін политетрафторэтилен үшін өтпелі токтың эксперименттік қисықтары алынды. Фурьенің дискретті түрлендіруіне негізделген сәулелендірілген политетрафторэтилендегі өтпелі ток қисықтарына талдау жасалды. Инфратөмен жиіліктер аймағында диэлектрлік жұтылуының қарқынды максимумының бар болуы көрсетілген, ол диэлектрлік өсудің, диэлектрлік тұрақтылықтың және диэлектрлік жоғалу факторының шамадан тыс үлкен мәндерімен сипатталады. Сәулеленген политетрафторэтиленнің біркелкі көлемдік поляризациясы туралы қорытынды жасалды. Көрсетілген жиілік аймағында байқалатын поляризация микроскопиялық аймақтар шегінде қақпанға түскен заряд тасымалдаушылардың миграциясының белсендірумен байланысты.

Тұрдыбеков К.М., Тұрдыбеков М.К.

Исследование кривых переходного тока в политетрафторэтилене с использованием программ Фурье-анализа.

Получены экспериментальные кривые переходного тока для политетрафторэтилена после воздействия высокоэнергетичного ионизирующего излучения. Проведен анализ кривых переходного тока в облученном политетрафторэтилене на основе дискретного преобразования Фурье. Показано существование интенсивного максимума диэлектрического поглощения в области инфранизких частот, который характеризуется аномально большими значениями диэлектрического инкремента, диэлектрической проницаемости и фактора диэлектрических потерь. Сделан вывод о равномерной объемной поляризации облученного политетрафторэтилена. Наблюдаемая в указанной области частот поляризация связывается с активацией миграции захваченных на ловушки носителей заряда в пределах микроскопических областей.

**INFORMATION
ABOUT AUTHORS**
**АВТОРЛАР ТУРАЛЫ
МӘЛІМЕТТЕР****СВЕДЕНИЯ
ОБ АВТОРАХ**

- Aitmagambetova M.B.** – Master (tech. science), Senior Lecture, L.N. Gumilyov Eurasian National University, Nur-Sultan, Kazakhstan
- Aringazin, A.K.** - Doctor of phys.-math.science, Professor, L.N. Gumilyov Eurasian National University, Nur-Sultan, Kazakhstan
- Bakhtybekova, A.R.** - PhD student, E.A. Buketov Karaganda University, Karaganda, Kazakhstan
- Bekturganov, Zh. S.** - Doctor of Chem.science, Professor, E.A. Buketov Karaganda University, Karaganda
- Bezrodny, M.K.** - Doctor of tech. sciences, Professor, National Technical University of Ukraine “Igor Sikorsky Kyiv Polytechnic Institute”, Kyiv, Ukraine
- Bulkairova, G.A.** - Master, Senior Lecturer, Karaganda E.A. Buketov University, Karaganda, Kazakhstan
- Dyussenov K.M.** – Candidate of techn.science, Associate Professor, L.N. Gumilyov Eurasian National University, Nur-Sultan, Kazakhstan
- Galtseva, O.V.** - Candidate of tech science, Assistant Professor, Tomsk State University of Control Systems and Radioelectronics, Tomsk, Russia
- Goncharenko, V.I.** - Doctor of techn.science, Professor, Director of the Military Institute, Moscow Aviation Institute (National Research University), Moscow, Russia
- Grachev, E.Yu.** – Candidate of tech science, Docent, Ryazan State Radio Engineering University, Ryazan, Russia
- Issabaeva, M.A.** - Candidate of Chem.science, Associate Professor, Senior Teacher, Chemistry Department, Toraighyrov Pavlodar University, Pavlodar, Kazakhstan
- Kasenov, B.K.** - Doctor of Chem.science, Professor, Head of the laboratory of thermochemical processes, Zh.Abishev Chemical-Metallurgical Institute, Karaganda, Kazakhstan
- Kasenova, Sh.B.** - Doctor of Chem.science, Professor, Chief researcher, Laboratory of thermochemical processes, Zh.Abishev Chemical-Metallurgical Institute, Karaganda, Kazakhstan
- Kasimov, A.R.** – Postgraduate student, Sh.Ualikhanov Kokshetau State University, Kokshetau, Kazakhstan
- Kozlov, E.A.** - Grachev, E.Yu. – postgraduate student, Ryazan State Radio Engineering University, Ryazan, Russia
- Kruchinin, N.Yu.** - Candidate of phys.-math. sciences, Docent, Associate professor, Department of radiophysics and electronics, Orenburg State University, Orenburg, Russia
- Kuanyshbekov, E.E.** – Master (Eng.) Leading engineer, Laboratory of thermochemical processes, Zh.Abishev Chemical-Metallurgical Institute, Karaganda, Kazakhstan
- Kucherenko, M.G.** - Doctor of phys.-math. sciences, Professor, Department of radiophysics and electronics, Orenburg State University, Orenburg, Russia
- Leonov, A.P.** - Candidate of tech. sciences, Assistant Professor, Division of Power and Electrical Engineering School of Energy and Power Engineering, Tomsk Polytechnic University, Tomsk, Russia
- Lyapunov, D.Y.** - Candidate of tech. science, Assistant Professor, Division of Power and Electrical Engineering School of Energy and Power Engineering, Tomsk Polytechnic University, Tomsk, Russia
- Lysenko, E.N.** - Doctor of techn.science, Head of the Research Laboratory, National Research Tomsk Polytechnic University, Tomsk, Russia
- Malyshev, A.V.** – Candidate of phys.-math.science, Senior Researcher, National Research Tomsk Polytechnic University, Tomsk, Russia
- Minkov, L.L.** – Doctor of phys.-math.science, Professor, National Research Tomsk State University, Tomsk, Russia
- Nedugov I.A.** - Engineer, L.N. Gumilyov Eurasian National University, Nur-Sultan, Kazakhstan
- Nukhuly, A.** - Doctor of Chem.science, Professor, Senator of the Parliament of the Republic of Kazakhstan
- Oleshko, V.S.** - Candidate of techn.science, Professor of the Department, Moscow Aviation Institute (National Research University), Moscow, Russia
- Oslovskiy, S.A.** – PhD student, National Technical University of Ukraine “Igor Sikorsky Kyiv Polytechnic Institute”, Kyiv, Ukraine
- Ospanova, D.A.** - Master, Senior Lecturer, Karaganda E.A. Buketov University, Karaganda, Kazakhstan
- Rakhmankyzy, A.** - Master, Lecturer, Karaganda E.A. Buketov University, Karaganda, Kazakhstan
- Rogachev, A.A.** - Doctor of tech. sciences, Professor of the Department of Transport and Technological Machines and Equipment of the Belarusian State University of Transport

Sagintaeva, Zh.I. - Candidate of Chem.sciences, Associate Professor, Leading researcher, Laboratory of thermochemical processes, Zh.Abishev Chemical-Metallurgical Institute, Karaganda, Kazakhstan

Sakipov, K.E. - Candidate of techn.sciences, Associate Professor, L.N. Gumilyov Eurasian National University, Nur-Sultan, Kazakhstan

Sakipova, S.E. – Candidate of phys.-math.sciences, Professor, E.A.Buketov Karaganda University, Karaganda, Kazakhstan

Sekerbayeva, G.K. – Postgraduate student, Karaganda E.A. Buketov University, Karaganda, Kazakhstan

Shaimerdenova, K.M. - Candidate of techn.science, Associate Professor, E.A. Buketov Karaganda University, Karaganda, Kazakhstan

Shayakhetova R.T. – Engineer. L.N. Gumilyov Eurasian National University, Nur-Sultan, Kazakhstan

Sheveleva E.A., PhD, Assistant Professor, Department of Control and Diagnostics, National Research Tomsk Polytechnic University, Tomsk, Russia

Shugayeva, T.Zh. – K.Zhubanov Aktobe Regional University, Aktobe, Kazakhstan

Shuiushbaeva, N.N. – PhD, Associate Professor, Sh.Ualikhanov Kokshetau State University, Kokshetau, Kazakhstan

Stoev, M. - PhD, Doctor of engineering, South-West University «NeofitRilski», Blagoevgrad, Bulgaria

Surzhikova S.A., PhD, Teacher, Czech Technical University in Prague, Prague, Czech Republic

Tanasheva, N.K. – PhD, Associate Professor, E.A. Buketov Karaganda University, Karaganda, Kazakhstan

Trubitsyn, A.A. – Doctor of phys.-math.sciences, Professor, Ryazan State Radio Engineering University, Ryazan, Russia

Turdybekov, K.M. - Senior Lecturer, E.A. Buketov Karaganda University, Karaganda, Kazakhstan

Turdybekov, M.K. - Master, Senior Lecturer, Karaganda Technical University, Karaganda, Kazakhstan

Turtubaeva, M.O. - PhD, Docent, Chemistry Department, Toraighyrov Pavlodar University, Pavlodar, Kazakhstan

Tussypbayeva, A.S. - Master, Senior Lecturer, Karaganda E.A. Buketov University, Karaganda, Kazakhstan

Usacheva, T.V. - Candidate of tech. sciences, Assistant Professor, Division of Power and Electrical Engineering School of Energy and Power Engineering, Tomsk Polytechnic University, Tomsk, Russia

Voronina, N.A. - Candidate of tech. science, Assistant Professor, Division of Power and Electrical Engineering School of Energy and Power Engineering, Tomsk Polytechnic University, Tomsk, Russia

Yessimseit A.K. – Postgraduate student, L.N. Gumilyov Eurasian National University, Nur-Sultan, Kazakhstan

Yurov, V.M. - Candidate of phys.-math.sciences, Associate Professor, Director of the Scientific Research Center, E.A. Buketov Karaganda University, Karaganda, Kazakhstan

Zeinidenov, A.K. – PhD, Associate Professor, Dean of the Physical-Technical Faculty, E.A. Buketov Karaganda University, Karaganda, Kazakhstan

About «Eurasian Physical Technical Journal»

ISSN 1811-1165 Key title: Eurasian physical technical journal (Print)
Abbreviated key title: Eurasian phys. tech. j.

ISSN 2413-2179 Key title: Eurasian physical technical journal (Online)
Abbreviated key title: Eurasian phys. tech. j.

Eurasian Physical Technical Journal (Eurasian phys. tech. j.) is a peer-reviewed open access international scientific journal publishing original research results on actual problems of Technical Physics and other related fields. Since 2004 «Eurasian phys. tech. j.» is published in English. E.A. Buketov Karaganda University is the main organizer and financial sponsor of Eurasian phys. tech. j. The international editorial board consists of leading physicists from 8 countries.

Since 2008, "Eurasian Physics and Technology Journal" has been included in the list of publications recommended by the Ministry of Education and Science of the Republic of Kazakhstan for publishing the main results of candidate and doctoral dissertations in physical and mathematical sciences. This status is confirmed in accordance with Science Committee Order No. 52 dated January 28, 2021.

Since May 2019 «Eurasian phys. tech.j.» has been indexed in the Scopus database on four scientific areas: Energy, Engineering, Materials Science, Physics and Astronomy. As of March 2, 2021 (data is updated monthly) Journal's CiteScoreTracker is 0.5 with a maximum percentile of 16% in Energy, <https://www2.scopus.com/sourceid/21100920795#tabs=0>

Re-registration Certificate No.KZ50VPY00027647 of the «Eurasian phys. tech. j.» issued October 6, 2020 by Information Committee of the Ministry of Information and Public Development of the Republic of Kazakhstan. According this since 2021 Eurasian phys. tech. j. will be published quarterly.

Publication Ethics and Malpractice Statement

Submission of an article to the Eurasian phys. tech. j. implies that the paper described has not been published previously, that it is not under consideration for publication elsewhere, that its publication is approved by all authors and tacitly or explicitly by the responsible authorities where the paper was carried out, and that, if accepted, it will not be published elsewhere in the same form, in English or in any other language, including electronically without the written consent of the copyright holder. In particular, translations into English of papers already published in another language are not accepted.

For information on Ethics in publishing and Ethical guidelines for journal publication see <http://www.elsevier.com/publishingethics> and <http://www.elsevier.com/journal-authors/ethics>.

The Eurasian phys. tech. j. follows the Code of Conduct of the Committee on Publication Ethics (COPE), and follows the COPE Flowcharts for Resolving Cases of Suspected Misconduct (http://publicationethics.org/files/u2/New_Code.pdf).

To verify originality, your article may be checked by the originality detection service Cross Check <http://www.elsevier.com/editors/plagdetect>.

Authors are responsible for the content of their publications. No other forms of scientific misconduct are allowed, such as plagiarism, falsification, fraudulent data, incorrect interpretation of other works, incorrect citations, etc. Authors are obliged to participate in peer review process and be ready to provide corrections, clarifications, retractions and apologies when needed. All authors of a paper should have significantly contributed to the research.

Reviewers should provide objective judgments and should point out relevant published works which are not yet cited. Reviewed articles should be treated confidentially. The reviewers will be chosen in such a way that there is no conflict of interests with respect to the research, the authors and/or the research funders.

Editors have complete responsibility and authority to reject or accept a paper, and they will only accept a paper when reasonably certain. They will preserve anonymity of reviewers and promote publication of corrections, clarifications, retractions and apologies when needed.

The acceptance of a paper automatically implies the copyright transfer to the Eurasian phys. tech. j.

All submitted papers will be sent for reviewing to leading experts in the given area.

The Editorial Board of the Eurasian phys. tech. j. will monitor and safeguard publishing ethics.

The editors reserve the right to accept or reject manuscripts.

GUIDELINES FOR AUTHORS

Research articles, survey papers and short notes are accepted for exclusive publication in the **Eurasian phys. tech. j.** in English. The manuscripts and short notes must contain original results of investigation in the following scientific areas of Physics:

ENERGY.

ENGINEERING.

MATERIALS SCIENCE.

PHYSICS AND ASTRONOMY

All publishing manuscripts and short notes must have been recommended by a member of the editor board or by the organization (University), where the work was performed. The author who submitted an article for publication will be considered as a corresponding author.

The paper, short note or review paper shall include an abstract of the contents, not exceeding 200 words and keywords (no more than 10). The abstract must not coincide with the introduction or conclusive part of the work and must not contain references, abbreviations and other unknown words.

All articles should have list of keywords or terms (3 to 10) for indexing purposes.

The text of a paper must not exceed 6-10 pages including tables, figures (no more than 6) and references (no more than 30). A short note must not exceed 4-5 pages including no more than 2 figures. A review paper must not be more than 15-20 pages (including no more than 10 figures).

The text should be divided on structural parts: **Introduction, Theoretical part, Experimental technique, Results and Discussion, Conclusion**, etc.

Printed copies shall be on good quality paper of International size A4. All texts must be printed in Microsoft Word. It is preferable to use the Times fonts. **The text must be printed in 11 point letters, with 1 interval.** There shall be a margin of 30 mm at the left-hand edge, of 15 mm at the fore edge, of 30 mm at the head of the page and of 30 mm at the tail.

Acknowledgments may be shown at the end of the article text, before **REFERENCES**.

All references must be numbered in the text (for example, [1], [2-4]) and listed in numerical order.

Equations in your paper have to be written using the **Microsoft Equation Editor or the MathType** (<http://www.mathtype.com>) for (Insert | Object | Create New | Microsoft Equation or MathType Equation).

Tables must be inserted into the text.

Figures should be prepared in a digital form suitable for direct reproduction. Figures shall be submitted on the separate sheets and not included into the text.

The following files must be submitted via e-mail:

- Article text (*.doc);
- Figures (fig1.jpg, fig2.pcx);
- Figure captions (*.txt, *.doc).

The text file containing all Authors' names, organizations, postal code, postal address, telephone, fax, E-mail, scientific topic of the paper.

It is possible to use **rar** or **zip** compressors and to transmit the files as an attachment.

Title page (specimen)

UDC

TITLE

Smith J.H., Cooper H.J.

E.A. Buketov Karaganda State University, Karaganda, Kazakhstan, email@for_correspondence.kz

Abstract: 5-6 sentences

Keywords: no less 3, but no more 10 words

